Flow-Directed Assembly of Cellulose Nanocrystal Dispersions with Ordered Film Applications

by

Alexander Douglas Haywood

A dissertation submitted to the Graduate Faculty of
Auburn University
in partial fulfillment of the
requirements for the Degree of
Doctor of Philosophy

Auburn, Alabama
August 6, 2016

Keywords: Cellulose nanocrystal, liquid crystal, self-assembly
rheo-optics, rheo-SANS, aligned films

Approved by

Virginia A. Davis, Co-chair, Alumni Professor of Chemical Engineering
W. Robert Ashurst, Co-chair, Uthlaut Family Endowed Associate Professor of Chemical Engineering
Zhihua Jiang, APPF Assistant Professor of Chemical Engineering
Michael C. Hamilton, Associate Professor of Electrical Engineering

Abstract

This dissertation presents the results of highly collaborative research on the fluid-phase assembly of cellulose nanocrystals (CNC) into ordered films. Due to their extraordinary properties, CNC are increasingly being considered as nanoscale building blocks for advanced materials. However, controlled and predictable assembly into ordered structures is necessary for CNC's outstanding properties to manifest in macroscale objects. This work focused on CNC films with two different structures: 1) nematically aligned films for application as the structural layer in microelectromechanical systems (MEMS), and 2) chiral films for application as optical devices such as reflectors, security papers, or filters. The key contribution of this research has been to obtain insight into the relationship between dispersion microstructure, shear response, and the final structure and properties of the film. These results can be used to guide the development of specific applications based on CNC films.

In the first portion of the work, rheo-optical microscopy and microspectrophotometry were used to gain new insights into the interrelated effects of liquid crystalline phase behavior, flow, and microstructural relaxation on CNC films. Aqueous liquid crystalline CNC dispersions showed greater alignment after shear than isotropic or biphasic dispersions. However, CNC gels exhibited lower alignment at equivalent shear rates. Optical contrast measurements were found to be an effective and facile way of quantifying microstructural relaxation after the cessation of shear and the anisotropy of CNC films. The combination of greater initial alignment and slower relaxation of sheared liquid crystalline dispersions resulted in nematically aligned films. Depending on their thickness, these films can be optically transparent in the visible regime or exhibit tunable interference colors.

Using a novel microfabrication scheme, the nematically aligned films were processed into MEMS test devices including doubly clamped beams (DCB), cantilever beam arrays (CBA), residual stress testers (RST), and mechanical strength testers (MST). Using these devices it was determined that the CNC film has an elastic modulus of 72 GPa, a compressive residual stress of 66 kPa, and a fracture strength of 2 GPa. While not quantified, it was clear from curvature in different cantilever beams that the films had anisotropic mechanical properties.

In the latter portion of the work rheo-small-angle neutron scattering (rheo-SANS) was used to investigate the shear behavior and relaxation of CNC dispersions, mostly in the biphasic regime. Order parameter increased with both shear rate and concentration. Interestingly, three region like behavior was observed in both the rheology versus shear rate and order parameter versus shear rate curves for the biphasic dispersions. Based on the rheo-SANS and rheo-optical microscopy data, a mechanism has been proposed to explain this behavior. Preliminary results of the modeling of this system are also presented. In future work, the model will be used to further explain the flow behavior of CNC and to help guide the fabrication of chiral films through controlled relaxation of flow-aligned CNC dispersions.

These studies on the flow behavior of CNC liquid crystal highlight the interplay between dispersion microstructure, shear response, and microstructural relaxation. The

processing methods studied provided a foundation for establishing the processing route on large-scale assembly of CNC films with controlled morphology.

Acknowledgements

I would like thank my committee members for providing both their time and knowledge in the preparation and review of this manuscript. I would like to thank my advisors Dr. Virginia Davis and Dr. Bob Ashurst for providing a solid foundation and allowing me to follow my interests in this research. Thank you to Dr. Majid Beidaghi for helping to review this document and for serving as university reader.

This work could not have been completed without the collaborators that have contributed to many portions of this research. Thank you to Dr. Christopher Kitchens, Dr. Jose Orellena, and Ming Jiang for their help with CNC preparation. Thank you to Dr. Micah Green and Martin Pospisil for your incredible work on modeling cholesteric CNC. Thank you to Dr. Katie Weigandt for your support with SANS data collection and interpretation. Thank you to Partha Saha for taking my work on CNC MEMS to the next level. Finally, thank you to undergraduate researchers, Joshua Passantino, Cara Sake, Tom Gillis, Vitoria Scarpini, Mathew Rasmussem, and Kishan Patel, who helped me explore many cool areas of CNC assembly that I would not have been able to on my own.

To my many group mates over the years, Dr. Daniel Horn, Dr. Ao Geyou, Dr. Daisy Xu, Dr. Matthew Kayatin, Joyanta Goswami, Alex Kelly, Partha Saha, Mahesh Parit, Matt Noor, and Andre Hansford, thank you for the knowledge that you have passed on to me and for making every day in the lab fun. To the many great friends that I have made here in Auburn, thank you for making every day outside the lab fun.

Most importantly, I would like to thank my parents, Alan and Missy Haywood, for their constant support before, during, and after graduate school. I could not have done it without you. To Josh, Kelsey, and Camille, thank you for being the best siblings and giving me reason to look forward to going home during school holidays. Finally, thank you to my friends for every beach trip, football game, festival, and all the good times that kept me going through this process.

Table of Contents

Abstract ii

Acknowledgements v

List of Figures xi

List of Tables xvi

List of Equations xvii

Chapter 1 Introduction 1

Chapter 2 Background 4

  2.1 Cellulose Nanocrystals 4

    2.1.1 Cellulose Structure 4

    2.1.2 Cellulose Nanocrystal Isolation 5

  2.2 Liquid Crystals 10

    2.2.1 Liquid Crystalline Structure 10

    2.2.2 Lyotropic Liquid Crystalline Phase Behavior 12

    2.2.3 Onsager Theory 14

    2.2.4 Stroobants-Lekkerkerker-Odijik Theory 15

    2.2.5 Rheological Signatures of Liquid Crystalline Polymers 15

  2.3 Cellulose Nanocrystal Aqueous Dispersions 22

    2.3.1 Colloidal Stability of CNC 22

    2.3.2 Liquid Crystalline Phase Behavior of CNC 25

- 2.3.3 CNC Rheology....28
- 2.3.4 Small-Angle Scattering from CNC....29

2.4 Cellulose Nanocrystal Films....31

- 2.4.1 Aligned CNC Films....32
- 2.4.2 Cholesteric CNC Films....34

Chapter 3 Experimental Section....37

3.1 Cellulose Nanocrystal Dispersion Preparation....37

- 3.1.1 CNC-SA Isolation from Cotton Cellulose....38
- 3.1.2 CNC-HCl and CNC-AA Isolation from Cotton....39
- 3.1.3 Commercial CNC-SA....39
- 3.1.4 Commercial CNC-SA/Polymer Dispersions....40

3.2 Cellulose Nanocrystal Characterization....41

- 3.2.1 Determination of Size Distribution....41
- 3.2.2 Determination of Sulfate Content....41

3.3 Film Casting....42

3.4 Characterization Methods....43

- 3.4.1 Optical Microscopy....43
- 3.4.2 Rheology....45
- 3.4.3 Small-Angle Neutron Scattering....46
- 3.4.4 Microspectrophotometry....47
- 3.4.5 Confocal Microscopy....47
- 3.4.6 TGA-FTIR....48
- 3.4.7 Atomic Force Microscopy....49

3.4.8 Contact Angle Measurement....50

3.4.9 Mechanical Testing....50

3.5 Microelectromechanical System Fabrication....51

3.5.1 1st Generation MEMS....51

3.5.2 2nd Generation MEMS....52

Chapter 4 Nematic Films for MEMS Applications....54

4.1 CNC-HCl....55

4.2 CNC-AA....58

4.3 CNC-SA....63

4.3.1 CNC Characterization....63

4.3.2 Rheology....64

4.3.3 Optical Microscopy....66

4.3.4 Film Properties....74

4.4 CNC/Polymer Films....78

4.5 CNC MEMS (1st Generation)....84

4.5.1 CNC MEMS Films....84

4.5.2 CNC Film Stabilization....87

4.5.3 MEMS Test Platform Design....89

4.5.4 MEMS Fabrication Process....93

4.6 CNC MEMS (2nd Generation)....96

4.6.1 MEMS Fabrication Process....97

4.6.2 Anisotropic Properties....98

4.6.3 Mechanical Properties....99

Chapter 5 Chiral Films for Optical Applications 103

5.1 Rheo-SANS of CNC 103

5.1.1 CNC Characterization..103

5.1.2 Phase Behavior and Microstructure..104

5.1.3 Viscoelastic Properties..106

5.1.4 Steady Shear Rheology..106

5.1.5 Neutron Scattering..109

5.2 Modeling..118

Chapter 6 Conclusion..122

References..125

List of Figures

Figure 2.1 Chemical structure of cellulose. 4

Figure 2.2 The hydrogen bonding network in crystalline cellulose. 5

Figure 2.3 Electron microscope image of sulfuric acid hydrolyzed CNC. 7

Figure 2.4 Conductometric titration curves of CNC. 9

Figure 2.5 Reaction scheme illustrating the simultaneous hydrolysis and esterification of cellulose. 10

Figure 2.6 Diagram envisaging the arrangement of liquid crystalline domains to illustrate the distinction between local directors, n, and the global director, N. 11

Figure 2.7 Friedelian classes of liquid crystals 12

Figure 2.8 Lyotropic liquid crystalline phase transitions. 13

Figure 2.9 Viscosity versus concentration curve of PBG in m-cresol at several shear rates.16

Figure 2.10 Three regions flow curve by Onogi and Asada. 17

Figure 2.11 Flow curves illustrating the difficulty of determining three region behavior for LCPs. 18

Figure 2.12 N_1 versus shear rate of 17 wt % PBLG (M_w = 350000) and m-cresol for two cone angles 19

Figure 2.13 Reduced shear stress versus shear unit curve of 37 wt % PBLG in m-cresol solution. 20

Figure 2.14 Comparison between steady shear and complex viscosities for 50 % wt. HPC in water. η (square); η^* (triangle). 21

Figure 2.15 TEM images of (a) CNC-HCl, (b) CNC esterified at 40°C, (c) CNC esterified at 60°C, and (d) CNC-SA. 24

Figure 2.16 Relative viscosities of cellulose suspensions versus volume fraction. 24

Figure 2.17 Dried down film of birefringent dispersion between crossed polarizers. 26

Figure 2.18 Optical micrograph between crossed polars of the anisotropic phase formed by dispersions of sulfuric acid hydrolyzed cellulose nanocrystals. 27

Figure 2.19 Sketch illustrating the hydrophobic interaction in cellulose nanocrystal dispersions in the presence of organic counterions. 28

Figure 2.20 Helical pitch as a function of CNC volume fraction determined by laser diffraction...30

Figure 2.21 Average center-to-center separation distance for CNC as measured by SAXS.31

Figure 2.22 Experimental setup for convective-shear assembly......................................33

Figure 2.23 AFM of film prepared on a silica substrate from a 4.5% CNC dispersion at intermediate withdrawal rate. 33

Figure 2.24 Correlation of optical and electron microscopy and the reflectance spectra of different domains. 36

Figure 3.1 Schematic of CNC production using different types of acid ahydrolysis. 38

Figure 3.2 Schematic of flow plane visible in the Linkam Shear Cell. 44

Figure 3.3 Schematic of flow planes that are accessible by rheo-SANS. 47

Figure 3.4 Schematic of contact angle measurement where θ is the contact angle. 50

Figure 4.1 Large birefringent aggregate found in a 3.06 vol % CNC-HCl dispersion viewed by optical microscopy...56

Figure 4.2 Cross-polarized optical microscope images of CNC-HCl dispersions............57

Figure 4.3 Optical microscopy images of CNC-HCl films..57

Figure 4.4 Cross-polarized optical microscopy images of CNC-HAA dispersions...........59

Figure 4.5 AFM images of a) CNC-AA, and b) CNC-SA adsorbed onto a mica surface. 60

Figure 4.6 3D representation of confocal microscope z-stacked images of a 0.06 vol % CNC-AA dispersion..61

Figure 4.7 3D representation of confocal microscope z-stacked images of a 0.93 vol % CNC-AA dispersion..61

Figure 4.8 Cryo-SEM images of 1.84 vol % CNC-AA dispersion showing the ribbon like morphology resulting from ISISA 62

Figure 4.9 Cryo-SEM image of a) 0.77 vol % CNC-AA dispersion with a layered structure, and b) 1.54 vol % CNC-AA dispersion with a network like structure. 63

Figure 4.10 Steady shear viscosity of aqueous CNC dispersions verseus shear rate. 64

Figure 4.11 The storage modulus G' and loss modulus G" of CNC dispersions at 11.6 and 15.8 vol %. 65

Figure 4.12 Cross-polarized optical microscopy images of CNC dispersions after shear.67

Figure 4.13 Enlarged region of Figure 4.12f showing the cholesteric fingerprint texture.67

Figure 4.14 Cross-polarized images showing phase behavior of CNC suspensions in cuvettes 68

Figure 4.15 Michel-Levy birefringence chart. 70

Figure 4.16 Sheared 11.6 vol % dispersions at additional shear rates 71

Figure 4.17 Cross-polarized optical microscopy images of CNC suspensions over time during relaxation from 100 s^{-1} shear. 73

Figure 4.18 Cross-polarized optical microscope images of drop cast films. 75

Figure 4.19 Doctor blade coated CNC films made from a) isotropic, b) biphasic, c) liquid crystalline and d) gel dispersions. 77

Figure 4.20 CRAIC spectra and images of CNC films prepared from liquid crystalline dispersion 78

Figure 4.21 Comparison of the mechanical properties of flocculated films with different thicknesses 80

Figure 4.22 Representative cross-polarized microscopy images of all films in the CNC/PEO film study. 81

Figure 4.23 Mechanical properties of CNC/PEO Films 83

Figure 4.24 AFM images showing the surface topography of (a) CNC-SA, (b) CNC-HCl, and (c) CNC-AA films on silicon substrates. 85

Figure 4.25 TGA weight percent versus temperature curve for (blue) original and (red) heat treated CNC-SA films and (green) CNC-HCl film..88

Figure 4.26 FTIR Spectra of CNC-SA film decomposition products at 180°C. 89

Figure 4.27 LASI layout of CNC MEMS module. 90

Figure 4.28 LASI layout of a) residual stress tester, b) mechanical strength tester, c) resonator, and d) cantilever beam array. 93

Figure 4.29 Developed patterns in photoresist film..94

Figure 4.30 Adhesion problem between CNC film and second photoresist layer. 95

Figure 4.31 Failed fabrication of CBAs...96

Figure 4.32 Representative reflected light microscopy images of CNC-MEMS devices. 96

Figure 4.33 Reflected optical microscopy images showing the steps involved in photolithographic fabrication scheme for 2nd Generation CNC MEMS. 98

Figure 4.34 Reflected microscopy images showing the effect of the stress gradient developed in CNC cantilevers 99

Figure 4.35 Micromechanical property analysis graphs of CNC-MEMS devices. 101

Figure 4.36 Reflectance micrograph showing thickness dependent compressive stress developed in CNC-RSTs...102

Figure 5.1 Polarized optical microscopy images of CNC dispersions............................105

Figure 5.2 Linear viscoelastic properties of CNC dispersions 107

Figure 5.3 Viscosity versus concentration curves for CNC dispersions..........................108

Figure 5.4 a) Scattering curves for each CNC dispersion. For clarity the intensities have been offset on the y axis. b) CNC spacing as a function of concentration ...110

Figure 5.5 Reduced two-dimensional scattering data for the 2.49, 5.16, and 7.16 vol % dispersions 112

Figure 5.6 Annular averages of 2D scattering patterns for 8.48 vol % CNC at shear rates ranging from 0.01 to 100 s^{-1}. 113

Figure 5.7 Order parameter versus shear rate for CNC dispersions 113

Figure 5.8 Shear cell cross-polarized optical microscope images of the 4.50 vol % dispersion...116

Figure 5.9 Order parameter (red squares) and viscosity (blue diamonds) versus concentration for CNC dispersions at $\dot{\gamma} = 1.0\ s^{-1}$. 117

Figure 5.10 Order parameter vs. time after cessation of shear for CNC dispersions 118

Figure 5.11 Model results and cross-polarized optical microscope images for liquid crystalline dispersion relaxation after high shear...120

Figure 5.12 Polarized optical microscope image showing transition from zig-zag pattern to cholesteric fingerprint texture within a domain. 121

List of Tables

Table 2.1 Length and width of cellulose nanocrystals from various sources. 6

Table 2.2 Sulfur content and the amounts of acidic groups in cellulose nanocrystals.......23

Table 2.3 Order parameter and mechanical properties of CNC films................................34

Table 2.4 Cholesteric pitch of different domains in CNC films as determined from the cross-sectional SEM images. 36

Table 4.1 Water contact angle and RMS roughness of photoresist films after various air plasma treatment protocols. 87

Table 4.2 Summary of CNC MEMS mechanical properties. (Data by Partha Saha) 102

Table 5.1 Shear rate at region transitions and rate index during each region for CNC dispersions from rheology data. 109

Table 5.2 Shear rate at region transitions for CNC dispersions from SANS data. 115

List of Equations

Equation 2.1 Definition of Order Parameter..11

Equation 2.2 Relationship Between Pitch and Concentration 12

Equation 2.3 Isotropic to Biphasic Transition Concentration from Onsager Theory 14

Equation 2.4 Biphasic to Liquid Crystalline Transition Concentration from Onsager Theory 14

Equation 2.5 Conversion from Weight Fraction to Volume Fraction 14

Equation 2.6 Isotropic to Biphasic Transition Concentration from SLO Theory 15

Equation 2.7 Biphasic to Liquid Crystalline Transition Concentration from SLO Theory15

Equation 2.8 Selective Reflection from Cholesteric Liquid Crystals and Films 35

Equation 3.1 Resolution of an Optical Microscope 43

Equation 4.1 Light Intensity Transmitted by a Birefringent Sample Through Cross-Polarizers 72

Equation 4.2 MEMS Residual Stress Tester Equation..90

Equation 4.3 MEMS Mechanical Strength Tester Equation 91

Equation 4.4 MEMS Resonator Equation..92

Equation 5.1 Legendre Series Expansion to Fit Orientational Distribution Function from SANS Data...112

Equation 5.2 Order Parameter from First Legender Coeffiecient...................................113

Equation 5.3 Modified Landau-de Gennes Model for Cholesteric Liquid Crystals 119

Equation 5.4 Order Parameter Calculation from Model Data 121

Chapter 1 Introduction

Since its discovery in 1838, cellulose has been used extensively in many industries; particularly in pulp and paper, and textiles. Industrial applications of cellulose and cellulose derivatives include rayon and acetate fibers, regenerated cellulose films such as cellophane, excipients in tablets, and food additives.[1] Research into the nanoscale properties of cellulose began as early at the 1950's. There has been a significant increase in interest starting in the early 1990's.[2] The increase in research is partially due to the discovery of chiral nematic structure in cellulose nanocrystal dispersions. Due to their excellent strength and stiffness the most widely studied application of cellulose nanocrystals (CNC) has been as a reinforcing agent in polymer nanocomposites. However, cellulose nanocrystals are increasingly being considered as nanoscale building blocks for advanced materials.[3] Some potential applications include iridescent films for security papers, polarizing rotators for lasers, optical storage devices, stimuli-responsive fluids, and applications in nanomedicine and nanosensing.[1]

Similar to other nanomaterials,[4-6] controlled and predictable assembly into ordered structures is necessary for CNC's outstanding properties to manifest in macroscale objects. Historically, controlled assembly was an issue in polymer manufacturing, where the mechanical properties attained by polymer fibers were a fraction of the theoretical maximums.[7] Such discrepancies have largely been attributed to non-ideal morphologies, particularly, chains aligning non-parallel to the stress direction. For dispersions of rod-like polymers and anisotropic nanomaterials, the balance between rotational and translational entropy results in the formation of lyotropic liquid crystalline phases above a critical concentration that is a function of solute aspect ratio, size polydispersity, and solvent-solute thermodynamic compatibility.[8-10] The combination of lyotropic liquid crystalline phase behavior and processing shear has been shown to facilitate the production of highly aligned fibers and films. One of the best known commercial products enabled by this approach is DuPont Kevlar® which is solution spun from a dispersion of the rod-like polymer poly(p-phenylene terephthalamide) in concentrated sulfuric acid.[11]

CNC also possess the anisotropic shape and rigidity needed to form lyotropic liquid crystalline phases. Moreover, CNC extracted using sulfuric acid hydrolysis can be readily dispersed in water at sufficient concentrations for cholesteric liquid crystalline phase formation.[12] Producing CNC films is an area of ongoing research that requires understanding the combined effects of dispersion microstructure and processing on film properties. Previous studies have separately investigated the effects of initial microstructure, flow behavior, and microstructural relaxation during drying on CNC dispersions and films, but there has been little work focused on understanding the interrelationships between these parameters.

This dissertation presents the results of highly collaborative research on the fluid-phase assembly of cellulose nanocrystals (CNC) into ordered films. While the final applications were considered throughout this work, the key contribution of this research has been to obtain insight into the relationship between dispersion microstructure, shear response, and the final structure and properties of the film. Along with the major results in these sections, preliminary results from a number of secondary projects will be presented.

Chapter 2 provides background information on CNC, liquid crystals, rheology and phase behavior of rods dispersed in liquids, and CNC films. Chapter 3 provides information on instrumentation and experimental techniques. The results and discussion are organized into two sections: 1) nematically aligned films for application as the structural layer in microelectromechanical systems, and 2) chiral films for application as optical devices such as reflectors, security papers, or filters. Chapter 4 primarily provides information on rheo-optics of CNC for and their application in nematic films for MEMS, and Chapter 5 primarily provides information on rheo-SANS of CNC for their application in chiral films for optical applications. Finally, Chapter 6 summarizes the conclusions of this research.

Chapter 2 Background

2.1 Cellulose Nanocrystals

2.1.1 Cellulose Structure

Cellulose, the world's most abundant macromolecule,[13] was first isolated by Anselme Payen in the early 1800's. It is the main constituent of plant cell walls and is produced naturally by a variety of organisms including some bacteria, fungi, algae, and even some animals.[14] Cellulose has been characterized as a high molecular weight polymer of β-1,4-linked anhydro-D-glucose units, where the repeat unit is a dimer of glucose, referred to as cellobiose (Figure 2.1).[15] In 1920, X-ray investigations showed that natural cellulose fibers contain both amorphous and crystalline regions.[16] The crystalline regions are formed due to cellulose's tendency towards both intra- and intermolecular hydrogen bonds (Figure 2.2). The proportions and size of the ordered and disordered regions are highly dependent on the cellulose source.[17] Despite the abundance of hydroxyl groups in its structure and its hydrophilic nature, cellulose is insoluble in water due to its highly crystalline structure.

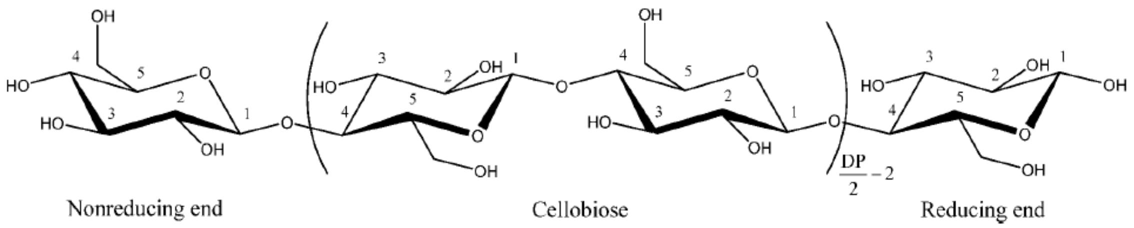

Figure 2.1 Chemical structure of cellulose.[15]

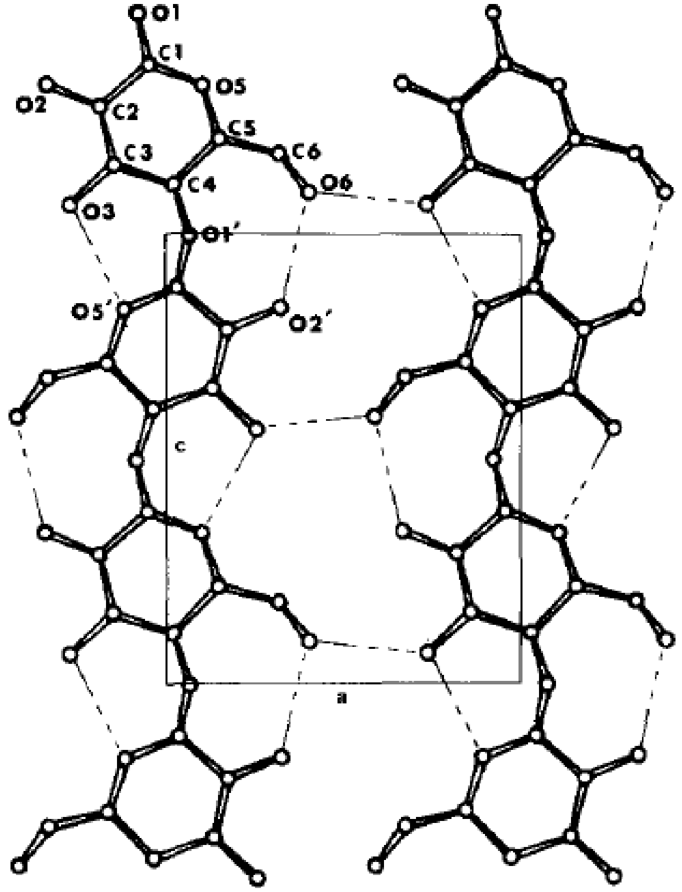

Figure 2.2 The hydrogen bonding network in crystalline cellulose.[18]

2.1.2 Cellulose Nanocrystal Isolation

The predominant method for the isolation of cellulose nanocrystals (CNC) is by acid hydrolysis of cellulose fibers where the CNC size (Table 2.1) and surface chemistry depend on the cellulose source and reaction conditions.[19] Since the acid cannot penetrate the crystalline regions, the amorphous regions of the cellulose fiber are preferentially hydrolyzed.[20] While long reaction times will completely digest the cellulose, terminating the reaction will result in the production of CNC.[21]

Table 2.1 Length and width of cellulose nanocrystals from various sources.[15]

Source	Length (nm)	Width (nm)
Bacterial	100-1000	5-50
Cotton	70-300	5-15
Cotton Linter	25-500	6-70
Microcrystalline Cellulose	35-500	3-48
Ramie	50-250	5-10
Sisal	100-500	3-5
Tunicate	100-3000	9-30
Valonia	>1000	10-20
Soft Wood	100-200	3-5
Hard Wood	140-150	4-5

The production of a colloidal solution of CNC by acid hydrolysis was first reported by Rånby in 1949.[16] Acid hydrolysis of either wood or cotton cellulose fibers was performed in boiling 2.5 N sulfuric acid (H_2SO_4) for 1-8 hours. The resulting CNC was repeatedly washed by centrifugation with distilled water. At a pH of 4, the maximum cellulose concentration of 0.5% in the sol was achieved. Rånby and Ribi further characterized these CNC morphologically by electron microscopy and structurally by X-ray and electron diffraction.[22] They concluded that the hydrolysis resulted in rod-like particles having the same dimensions as the crystalline regions of the cellulose fibers (Figure 2.3). The particles had high crystallinity and the same structure and lattice dimensions as cellulose fiber. Marchessault et. al. hypothesized that the colloidal solutions of CNC arose from repulsive forces of sulfate half esters introduced to the surface during sulfuric acid hydrolysis.[23] Analysis of freeze dried CNC showed about 1% to 2% sulfur, and electrophoresis showed that the particles were negatively charged. Today, typical hydrolysis procedures use strong acids with controlled temperature, acid-to-cellulose ratio, and time. Specific protocols have been established for the optimal production of CNC from a variety of cellulose sources. Dong et. al. studied the effect of preparation conditions on the properties of CNC from cotton fiber.[24] The hydrolysis conditions were optimized by varying temperature and time while the sulfuric acid concentration was constant at 64% (w/v) with cellulose to acid ratio of 1:8.75 (g/ml). Low hydrolysis temperature required reaction times of up to 18 hours while at high temperatures the reaction was hard to control and resulted in sample discoloration. The optimal reaction temperature was determined to be 45 °C, producing a 44% yield after 1 hour.[24]

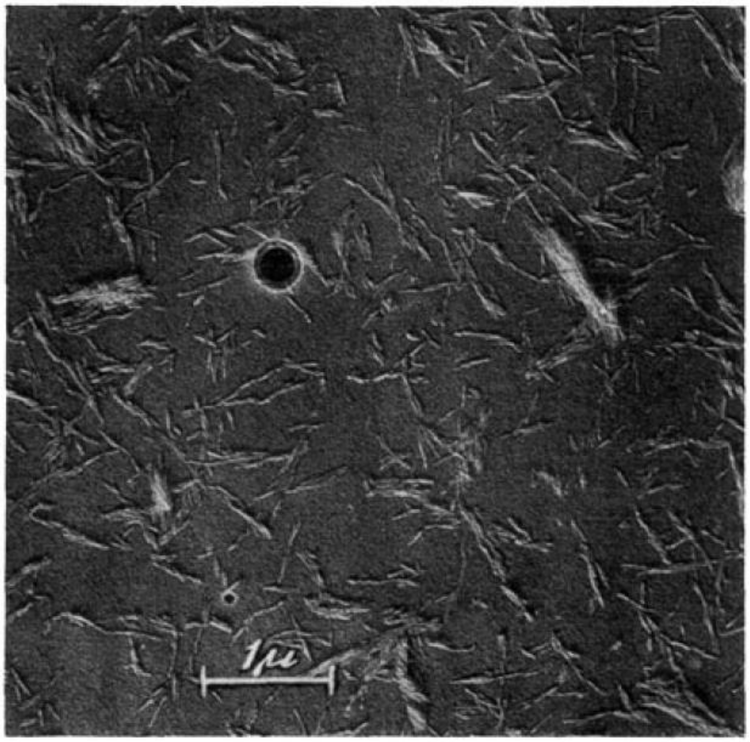

Figure 2.3 Electron microscope image of sulfuric acid hydrolyzed CNC.[22]

Simultaneous to Rånby, Battista explored the hydrochloric acid (HCl) degradation of cellulose fibers.[25] His work investigated the effects of time, temperature, and acid concentration on the hydrolysis of both native and regenerated cellulose. A wide variety of cellulose sources were investigated, and data was collected on weight loss and degree of polymerization of the hydrolysis product. When mild hydrolysis conditions (low acid concentration and low temperature) were used for longer periods of time, the average degree of polymerization of the resultant material was the same as when harsh hydrolysis conditions are used for a short period of time. The average degree of polymerization levels off to a constant value after a certain degree of hydrolysis, dependent primarily on the cellulose source. Degree of polymerization was determined through a correlation with solution viscosity and relates to the length of the CNC (the longer the rod, the higher degree of polymerization). In a later patent Battista et. al. claimed that this method produces cellulose crystallites with a high degree of perfection and an unusually high level of chemical purity.[26] Hydrochloric acid hydrolysis had been used recently in a study by Araki et. al. to produce CNC with no surface functionalization beyond the native hydroxyl groups.[27] In this study softwood kraft pulp was hydrolyzed with 4 N HCl with a cellulose to acid ratio of 1:35 (g/ml) at 80°C for 225 min. The resultant material was washed repeatedly by centrifugation until the pH ≤ 4. These CNC were compared with those prepared from the same cellulose source by the more common H_2SO_4 hydrolysis. Transmission electron microscopy (TEM) observations gave almost identical appearances for the samples and X-ray diffraction patterns indicated that the crystalline form was nearly identical. Conductometric titration showed that the HCl hydrolyzed CNC was completely devoid of strong acid groups on the surface (Figure 2.4).

Braun and Dorgan reported on a single-step method for the isolation and surface functionalization of CNC using acid-catalyzed esterification.[28] This reaction scheme (Figure 2.5) uses a mixture of hydrochloric and acetic acids to simultaneously hydrolyze cellulose and introduce a methyl ester group onto the surface. Cotton linter was hydrolyzed in a mixture of 17.5 M acetic acid and 0.027 M HCl with a cellulose to acid ratio of 1:25 (g/ml) at 105°C with reaction times between 4 to 20 hours. The resultant material was

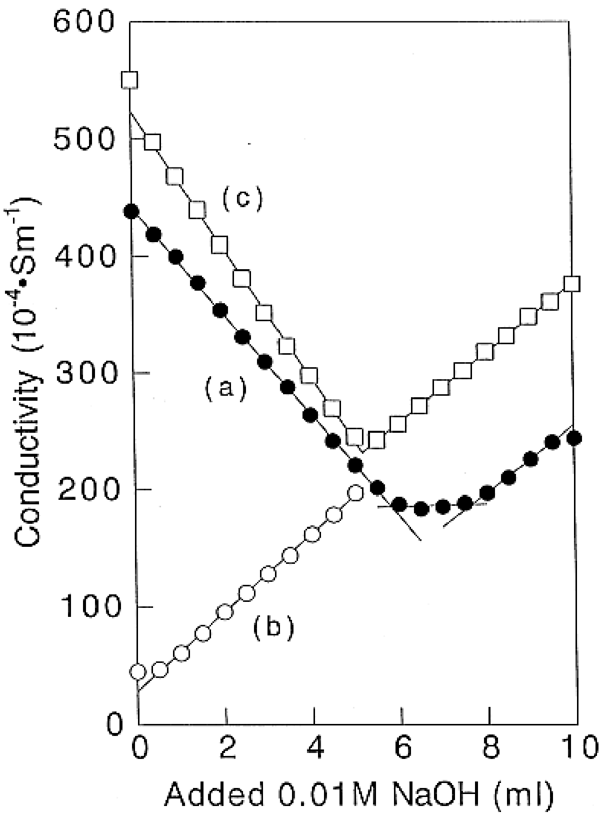

Figure 2.4 Conductometric titration curves of CNC. (a) H_2SO_4 hydrolyzed, (b) HCl hydrolyzed, and c) HCl hydrolyzed with initial addition of 5 ml of 0.01 M HCl.[27]

washed by centrifugation repeatedly until the pH reached 5 and the turbid supernatant was collected. TEM images indicated that the size of CNC obtained using the mixed acid system are similar to those from HCl hydrolysis of the same cellulose source. Fourier transform infrared (FTIR) spectra of the sample after dialysis exhibited a C=O stretch at 1736 cm^{-1} that is not present in the HCl hydrolyzed CNC indicating that methyl ester groups are covalently attached to the surface of the CNC.

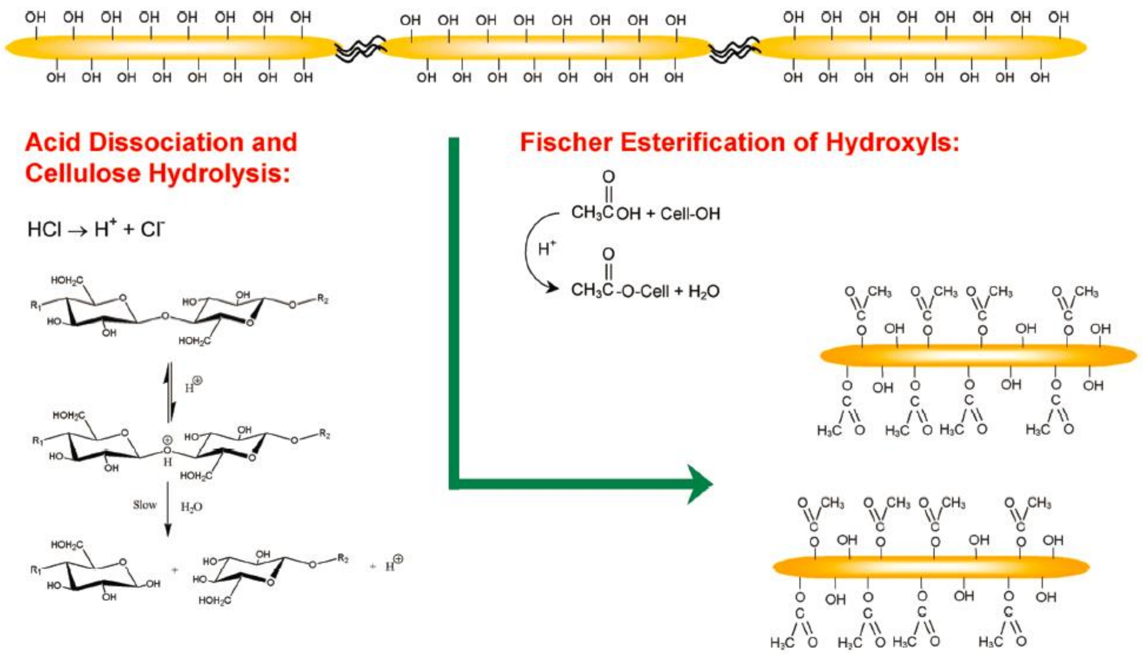

Figure 2.5 Reaction scheme illustrating the simultaneous hydrolysis and esterification of cellulose.[28]

2.2 Liquid Crystals

Liquid crystals are a mesophase that possesses both the order of a crystal and the fluidity of a liquid. Entities that form liquid crystals are termed mesogens and can be of two types, thermotropic or lyotropic. Thermotropic mesogens are small molecules with rigid cores, and their phase transitions depend on temperature. Lyotropic mesogens can be a variety of anisotropic macromolecules such as rigid polymers and rodlike nanomaterials. When dispersed in a solvent their phase transitions depend on their concentration. Since CNC liquid crystals are lyotropic section focuses on lyotropic liquid crystals.

2.2.1 Liquid Crystalline Structure

Friedel first reported on the existence of different types of liquid crystalline phases in 1922.[29] He characterized liquid crystals as nematic, cholesteric, or smectic. Nematic liquid crystals possess long range orientational order along a vector known as the director n, but do not possess positional order. Orientation along the director is not perfect, but is quantified by the order parameter S which is the same as the orientation function $\bar{P}_2$.[29] The order parameter is described by Equation 2.1, where θ is the angle between the rod long axis and the director and the angled brackets indicate an average over all rods in the system. Due to long relaxation times, lyotropic liquid crystals often have a polydomain structure with varying local directors, giving them a globally isotropic structure. This is illustrated in Figure 2.6. The order parameter has a value of 1 for perfect alignment and 0 for random orientation.

$$S = \frac{1}{2} < 3cos^2(\theta) - 1 > \qquad (2.1)$$

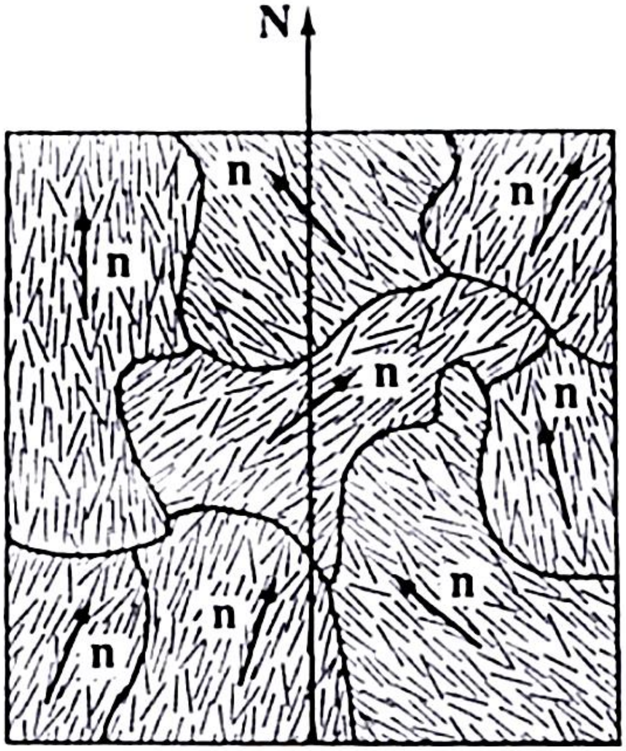

Figure 2.6 Diagram envisaging the arrangement of liquid crystalline domains to illustrate the distinction between local directors, n, and the global director, N.[29]

Cholesteric, or chiral nematic, liquid crystals possess local nematic order, however layers are rotated periodically about an axis perpendicular to the director. The distance in which the rods make a full rotation is known as the pitch. The cholesteric pitch shortens as the concentration increases and can be described by Equation 2.2, where P is pitch, c is concentration and A and n are scaling factors related to the system. The pitch is also effected by temperature, hydrostatic pressure, and salt content.

$$P = \frac{1}{Ac^{n}} \tag{2.2}$$

Finally, smectic liquid crystals exhibit both long range orientational and positional order. Representations of each Friedelian class are shown in Figure 2.7.

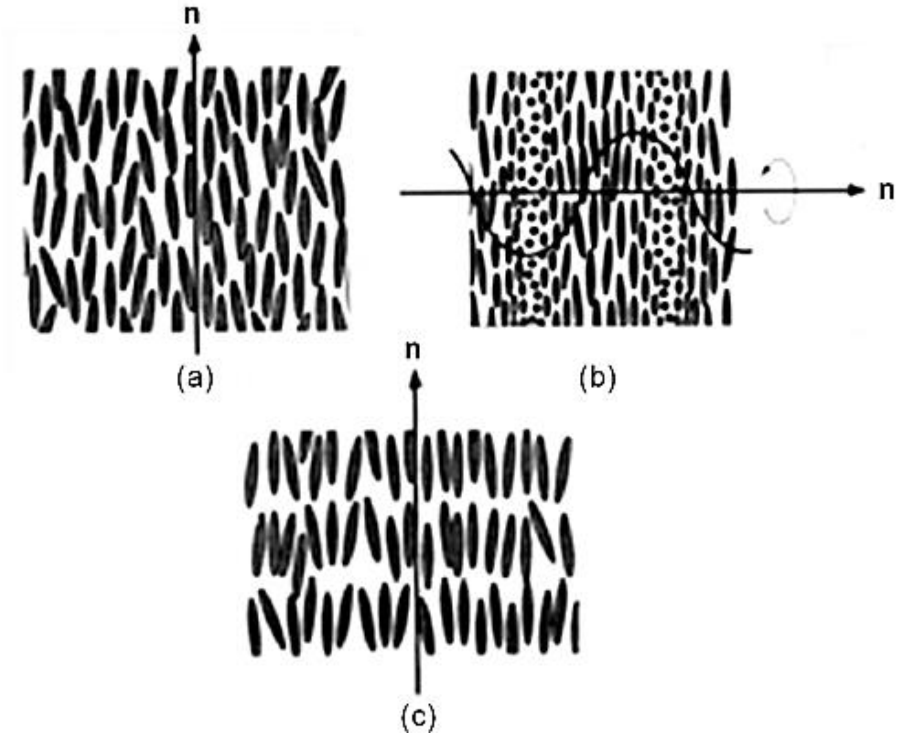

Figure 2.7 Friedelian classes of liquid crystals: a) nematic, b) cholesteric, c) smectic.[29]

2.2.2 Lyotropic Liquid Crystalline Phase Behavior

Doi and Edwards described the dynamics of rigid rodlike polymers through a series of regimes as the concentration is increased: dilute, semidulute, isotropic concentrated, biphasic, and liquid crystalline.[30] In dilute solutions, defined as when the average distance between rods is much larger than the rod length, the rods can rotate and translate freely. In the semidilute regime, the rotation of the rods is severely restricted by other rods. A further increase in concentration causes both the rotation and translation to be hindered, this is called the isotropic concentrated regime, where the motion is confined to straw like volumes as shown in Figure 2.8. When the concentration exceeds ϕ_I, the isotropic to biphasic transition concentration, the system enters the biphasic regime. Here a liquid crystalline phase coexists with an isotropic phase. As the concentration is increased in this regime the fraction of liquid crystalline phase increases until the solution reaches ϕ_{LC}, the biphasic to liquid crystalline transition concentration and the solution becomes a single liquid crystalline phase. For uncharged monodisperse rods the concentration of rods in each phase remains constant, and only the fraction of each phase changes with increasing concentration. Lyotropic liquid crystalline phase transitions are illustrated in Figure 2.8.

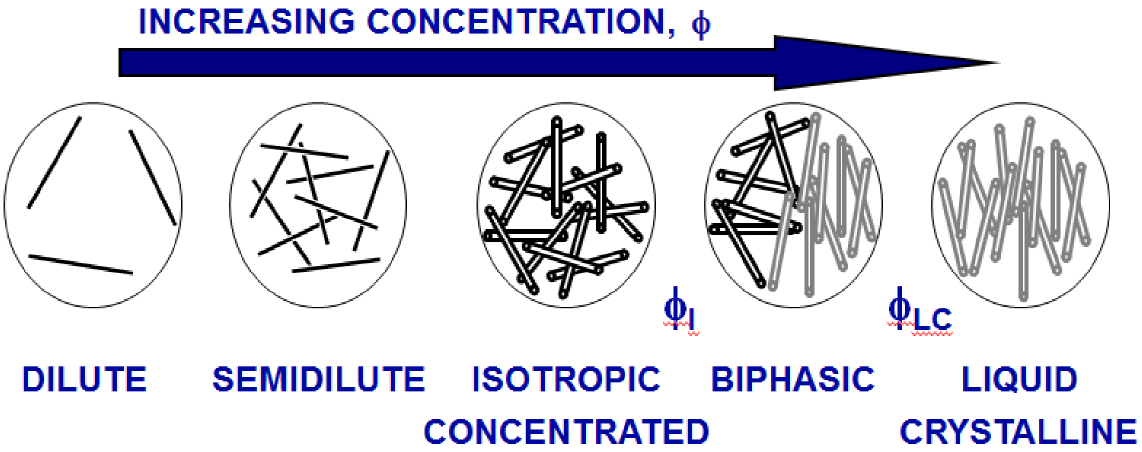

Figure 2.8 Lyotropic liquid crystalline phase transitions. Adapted from Doi and Edwards.[30-31]

2.2.3 Onsager Theory

Onsager (1949)[32] and Flory (1955)[33] theories are among the first developed to predict the phase transitions in lyotropic liquid crystals. Flory theory is still commonly used for rodlike polymer liquid crystals, however many rodlike nanomaterial systems adhere more closely to Onsager's original assumption of rigidity and "infinite length" (L>>d).[4] Onsager's theory considers ideal solutions of long, monodisperse, hard rods, in an athermal solvent, which interact only through excluded volume interactions. Based on Onsager theory, ϕ_I and ϕ_{LC}, and the coexistence concentrations in volume fraction are given by Equations 2.3 and 2.4. Volume fraction ϕ and weight fraction w are related through the densities ρ of the rod and the solvent as shown in Equation2.5.

$$\phi_I = 3.35\frac{d}{L} \qquad (2.3)$$

$$\phi_{LC} = 4.49\frac{d}{L} \qquad (2.4)$$

$$\phi = \frac{\rho_{rel} w}{1 + (\rho_{rel} - 1)w}, \qquad (2.5)$$

$$\rho_{rel} = \rho_{solvent}/\rho_{rod}$$

According to Onsager theory, aspect ratio (L/d) of rigid rods predicts the phase transition and coexistence concentrations. However, real systems rarely consist of completely monodisperse rods. Lekkerkerker et. al. considered this problem and noted a number of findings:[34] 1) Fractionation occurs, where the longer rods enter the liquid crystalline phase at lower overall concentration. 2) The biphasic region covers a larger range of concentrations. 3) The order parameter of the longer rods tends to be greater than that of the shorter rods. A number of more recent theories have further expanded Onsager theory to account for other interactions and polydispersity.[35-39]

2.2.4 Stroobants-Lekkerkerker-Odijik Theory

The Onsager modification most relevant to this work, Stroobants, Lekkerkerker, and Odijik (SLO) theory, describes phase separation in rodlike polyelectrolytes.[40] The effects of the charged rods are two-fold. First, there is an increase in the effective diameter of the rods D_{eff}. Second, a twisting factor h accounts for the preferred perpendicular orientation of charged rods. Odijik showed that the coexisting concentrations of rods in the biphasic region were given by Equations 2.6 and 2.7.[41] In these equations the concentration is expressed as the number density of rods, and h and b the twisting factor and the second virial coefficient of the system, respectively.

$$C_I = 3.290[(1 - 0.675h)b]^{-1} \tag{2.6}$$

$$C_{LC} = 4.191[(1 - 0.730h)b]^{-1} \tag{2.7}$$

2.2.5 Rheological Signatures of Liquid Crystalline Polymers

Nematic liquid crystalline polymers (LCP) often exhibit extraordinary rheological properties, however, in spite of extensive research their flow behavior is not fully understood. Although the properties can vary considerably from one LCP to another, there are a number of typical features: 1) a maximum in the viscosity versus concentration curve, 2) three region viscosity versus shear rate behavior, 3) sign change of the first normal stress difference, 4) long oscillatory transients, and 5) the Cox-Merz rule is not obeyed. It should be noted, however, that not all of these features are observed in every LCP. While the majority of research on liquid crystalline assembly has focused on polymers, the same framework can be used to understand the rheology of rodlike nanomaterial liquid crystals.[4]

The flow behavior of cholesteric liquid crystals has been studied far less than nematics, but many of the same principals apply.[42]

2.2.5.1 Maximum in Viscosity Versus Concentration

For typical polymer solutions, the viscosity increases monotonically with concentration. For lyotropic liquid crystalline polymers, generally, the viscosity increases with concentration in the isotropic region and reaches a maximum in the biphasic region. The transition from biphasic to liquid crystalline is typically on the right shoulder of the peak[43], before the viscosity again increases in the liquid crystalline region. This is not surprising, since molecules can slide past each other more readily in the nematic state than in the isotropic state. Figure 2.9 shows this typical behavior for PBG in m-cresol.[44] Also as the shear rate is increased, the maximum shifts to lower concentrations and the value of the maximum is depressed. This is because at high shear rates ordering is caused by both flow and liquid crystalline phase behavior.

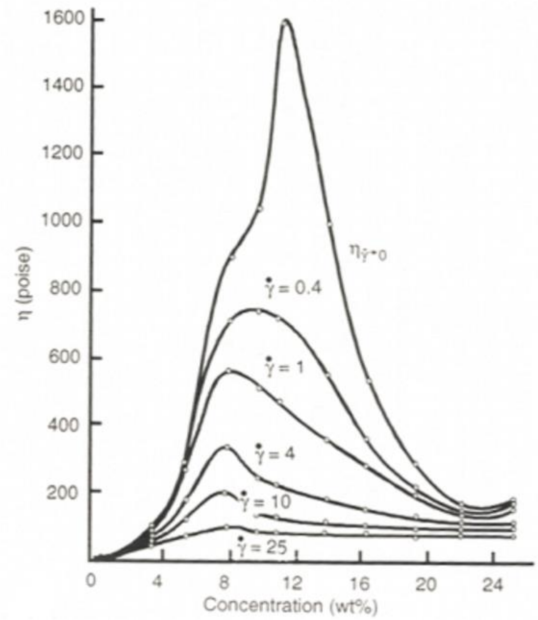

Figure 2.9 Viscosity versus concentration curve of PBG in m-cresol at several shear rates.[44]

2.2.5.2 Three Region Viscosity Versus Shear Rate Curve

For many LCPs, three distinct regions occur in the viscosity versus shear rate curve as shown in Figure 2.10.[45] Regions I and III are a low-shear-rate and high-shear-rate shear-thinning regime, respectively, and region II is a Newtonian plateau at intermediate shear rates. It is not clear for some LCPs if three region behavior is present, and it is not known whether the absence of three region behavior is due to differences in the systems or to experimental limitations in the shear rate ranges explored. Figure 2.11 shows seven flow curves for various LCPs.[43] While it is not difficult to discern three region behavior in three of these curves, others only exhibit one or two regions.

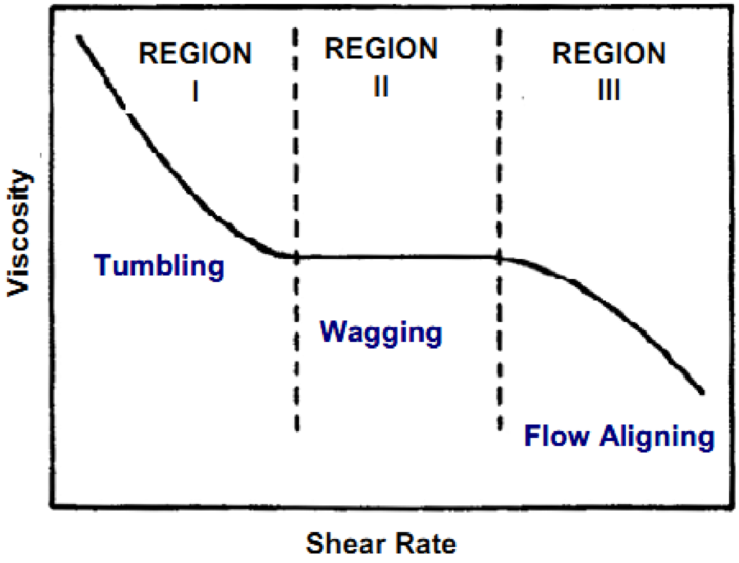

Figure 2.10 Three regions flow curve by Onogi and Asada.[46]

In isotropic polymer solutions, the viscosity versus shear rate curve typically consists of two regions, a Newtonian plateau at low shear rates and a shear thinning region when the flow becomes strong enough to orient the molecules. Region II and III in LCPs can be thought of as analogous to the behavior of isotropic polymer solutions. Therefore, it is region I that distinguishes the behavior of a LCP. While the origin of region I shear

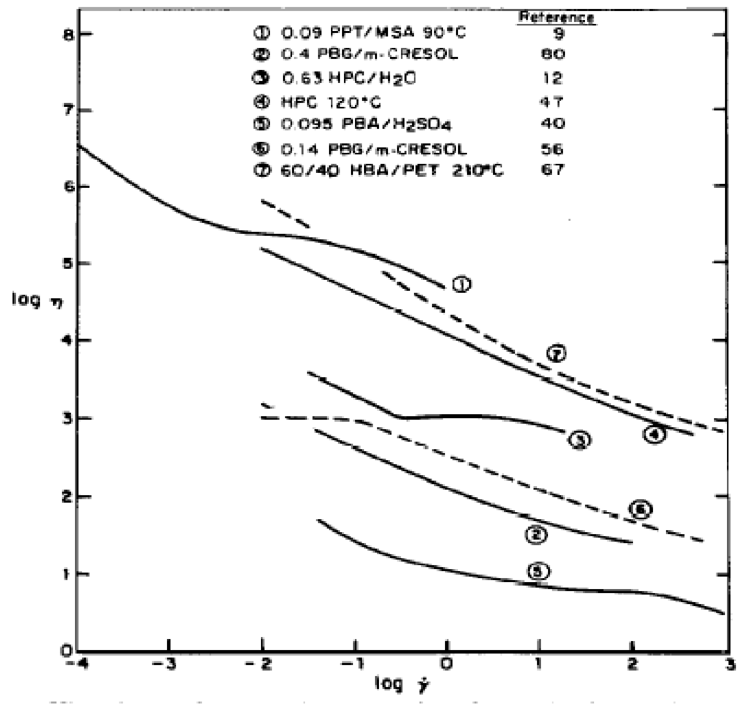

Figure 2.11 Flow curves illustrating the difficulty of determining three region behavior for LCPs.[43]

thinning is still debated, three mechanisms have been proposed.[43] In the first mechanism, shear thinning results from competition between orientation of the molecules at the boundary and in the shear field. The second mechanism attributes shear thinning to the texture of the liquid crystal. The third mechanism suggests that the LCP may undergo shear induced phase separation, which causes shear thinning.

Region II behavior is better understood than region I, however there are still two mechanisms that are seen for the Newtonian plateau. The first relates to "wagging" of the directors in the polydomain texture,[42] while the second is due to vorticity alignment of the rods over a limited shear rate range.[47] In region III, the flow is strong enough to increase the order parameter through flow alignment, which results in shear thinning. Typically, region III has a lower slope than region I.

2.2.5.3 Sign Change of First Normal Stress Difference

Along with the three region behavior of the viscosity versus shear rate curve, another striking behavior of LCPs is the behavior of the normal stresses under shear flow.[48] In ordinary polymer solutions the first normal stress difference (N1) is a positive quantity that steadily increases with shear rates. Figure 2.12 shows N1 versus shear rate for a 17 wt % PBLG and m-cresol solution.[49] It shows the typical behavior of N1 for a LCP, where at low shear rates N1 is a positive increasing function of shear rate. At intermediate shear rates, N1 suddenly decreases and changes to a negative value. As shear rate is further increased, N1 becomes positive once again. The fall in N1 to negative values occurs at approximately the beginning of region III behavior. The origin of negative N1 is still not completely understood, however, it is largely believed to be a consequence of the transition from “tumbling” to “wagging” of the director in the polydomain structure. Similar to three region behavior, negative N1 has not been observed for all LCP systems.

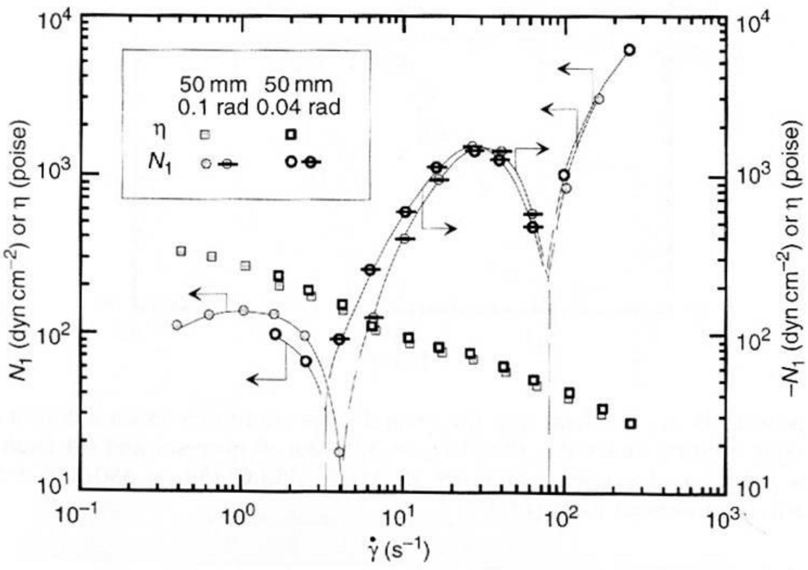

Figure 2.12 N_1 versus shear rate of 17 wt % PBLG ($M_w = 350000$) and m-cresol for two cone angles[49]

2.2.5.4 Long Oscillatory Transients

For LCPs, different transitions are often observed when shear flow is started, the flow direction is reversed, or the shear rate is suddenly changed.[42] For ordinary polymer solutions at low shear rates, the shear stress grows monotonically until it reaches its steady state value, while at higher shear rates there may be some overshoot and then a steady decrease to the steady state value. In either case the transient response lasts for only a few shear units (shear units are given by the nondimensional product $\dot{\gamma}t$). Figure 2.13 shows different behavior for a 37 wt % PBLG in m-cresol solution, which is typical of other LCPs. An oscillation of shear stress is seen with time after the startup of flow. This oscillation can last for as long as 100 shear units or more. The oscillatory behavior shows an important regularity, with stress versus shear unit curves lining up. Scaling behavior has also been seen after the cessation of shear, where the time for the strain to be recovered grows with the previously applies shear rate. This suggests that the elastic energy stored in the shear – induced distortions of the texture is proportional to shear rate.[42]

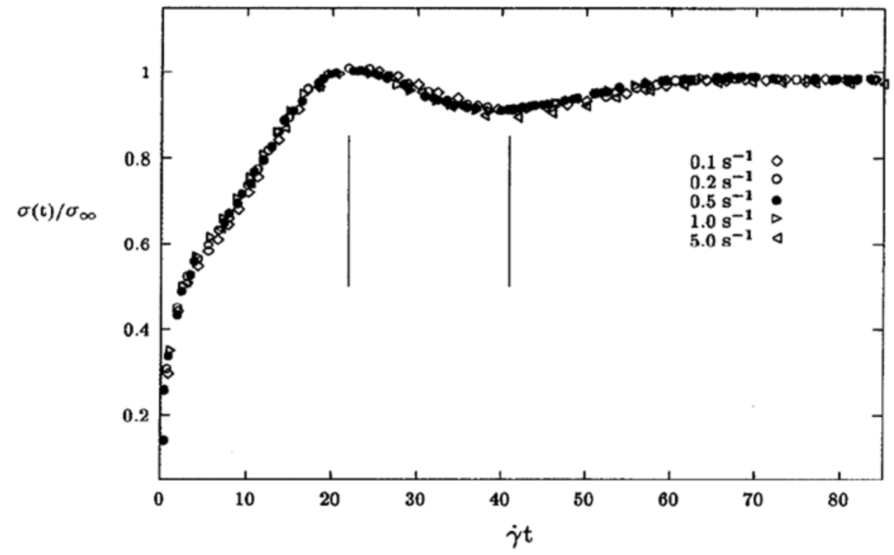

Figure 2.13 Reduced shear stress versus shear unit curve of 37 wt % PBLG in m-cresol solution.[50]

2.2.5.5 Cox-Merz Rule Not Obeyed

The Cox-Merz rule is an empirical rule which states that for values of $\dot{\gamma}$ and ω the steady shear viscosity $\eta(\dot{\gamma})$ equals the complex viscosity $\eta^*(\omega)$. Although not fully explained theoretically, this empirical rule applies well to ordinary polymer solutions. This is not the case for LCPs, as shown in Figure 2.14 for 50 wt % HPC in water. This is not surprising, since in LCPs, the microstructures, and therefore the rheology evolved by continuous shear and oscillatory shear are usually different. In addition to not following the Cox-Merz rule, measurements of $\eta^*(\omega)$ suffer reproducibility problems. This is due to the response of the material being significantly based on its shear history. In small molecule, thermotropic, nematics it takes only minutes for a LCP to heal itself from its shear history. However, in lyotropic nematics it can take anywhere from days to nearly a year.[42] Since it is impractical to wait this long for testing after sample loading, it is often necessary to employ a pre-shear protocol to erase the shear history and obtain reproducible results.

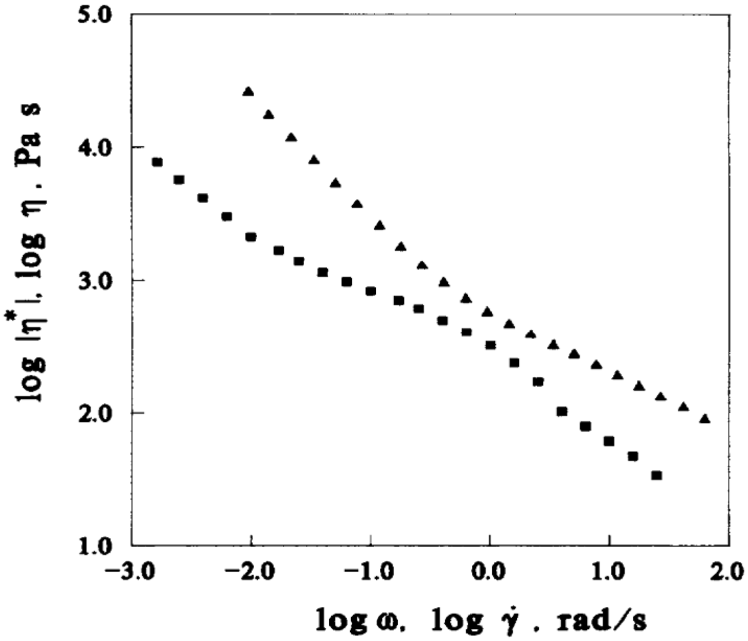

Figure 2.14 Comparison between steady shear and complex viscosities for 50 % wt. HPC in water. η (square); η^* (triangle).[51]

2.3 Cellulose Nanocrystal Aqueous Dispersions

2.3.1 Colloidal Stability of CNC

Cellulose nanocrystal suspensions were first observed by Rånby upon washing out of acid by centrifugation of sulfuric acid hydrolyzed cellulose nanocrystals (CNC-SA).[16] It was later shown that the dispersion arises from the ionization of surface sulfate half-esters as the pH increases resulting in repulsive forces between the nanocrystals.[23] Further investigation by electron microscopy showed that these suspensions were in fact dispersions of individual unit particles and small aggregates.[52]

The difficulty of obtaining good dispersions of hydrochloric acid hydrolyzed cellulose nanocrystals (CNC-HCl) has been noted in the literature.[27] Van den Berg et. al. prepared both CNC-SA and CNC-HCl suspensions from tunicate cellulose.[53] The CNC were sonicated for 6 hours at a concentration of 0.1 wt % and dispersion was assessed by inspection between crossed polarizing films. They used the presence of birefringence when viewed between the films was used as the criteria for good dispersability. The CNC-SA formed permanently birefringent dispersions at 0.1 wt % and above, however, homogeneous dispersions were not formed with the CNC-HCl. The suspension of CNC-HCl had been obtained from cotton and wood pulp after significant mechanical agitation. When the CNC-HCl was placed in water at 5 wt % solids, it settled out rapidly, but when this mixture was blended at high speed for 15 minutes a stable suspension of aggregates was achieved.[54]

Araki et. al. reported on the influence of the surface charge on the flow properties and viscosity behavior of CNC suspensions.[27, 55] CNC-SA and CNC-HCl suspensions were prepared using the established methods. Stable suspensions were obtained for each type of

CNC and both suspensions showed flow birefringence. TEM images showed that individual particles had the same dimensions for both H_2SO_4 and HCl hydrolyzed samples, but the CNC-HCl was significantly more aggregated (Figure 2.15). In order to vary surface charge post-hydrolysis addition of surface sulfate esters was carried out by reacting CNC-HCl with 55% (w/w) H_2SO_4 for 2 hours at 40°C or 60°C. The additional treatment had no effect on the size and shape of the particles, the effect on the aggregation behavior of the suspensions is shown in Figure 2.15. The resultant sulfur content and amount of acid groups for each nanocrystal type is shown in Table 2.2.

Although the post-hydrolysis esterified samples only had a small difference in surface charge their viscosity behavior was drastically different (Figure 2.16), indicating that the viscosity behavior is strongly affected by surface charge in the range of 50-60 mmol/kg. In shear flow, the viscosity of the CNC-HCl sample decreased over time, reaching equilibrium after 30 minutes. This behavior was explained as an effect of severe inter-particle aggregation that was destroyed by shear flow.

Table 2.2 Sulfur content and the amounts of acidic groups in cellulose nanocrystals.[55]

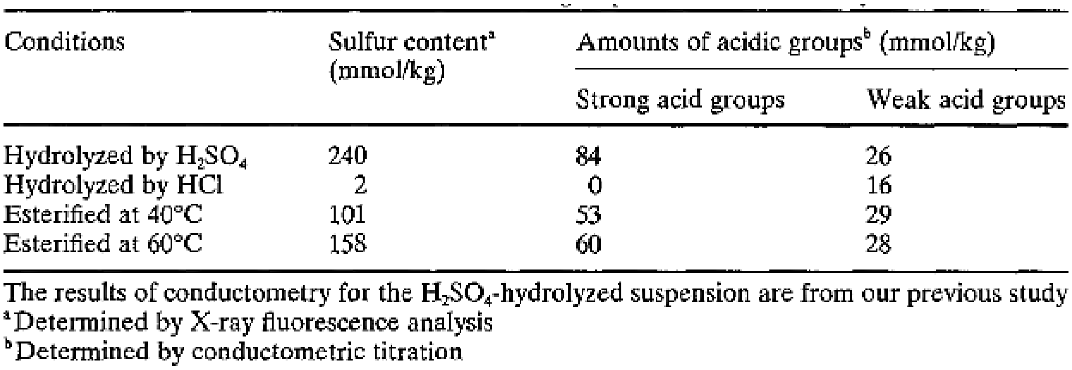

Conditions	Sulfur content[a] (mmol/kg)	Amounts of acidic groups[b] (mmol/kg)	
		Strong acid groups	Weak acid groups
Hydrolyzed by H_2SO_4	240	84	26
Hydrolyzed by HCl	2	0	16
Esterified at 40°C	101	53	29
Esterified at 60°C	158	60	28

The results of conductometry for the H_2SO_4-hydrolyzed suspension are from our previous study
[a] Determined by X-ray fluorescence analysis
[b] Determined by conductometric titration

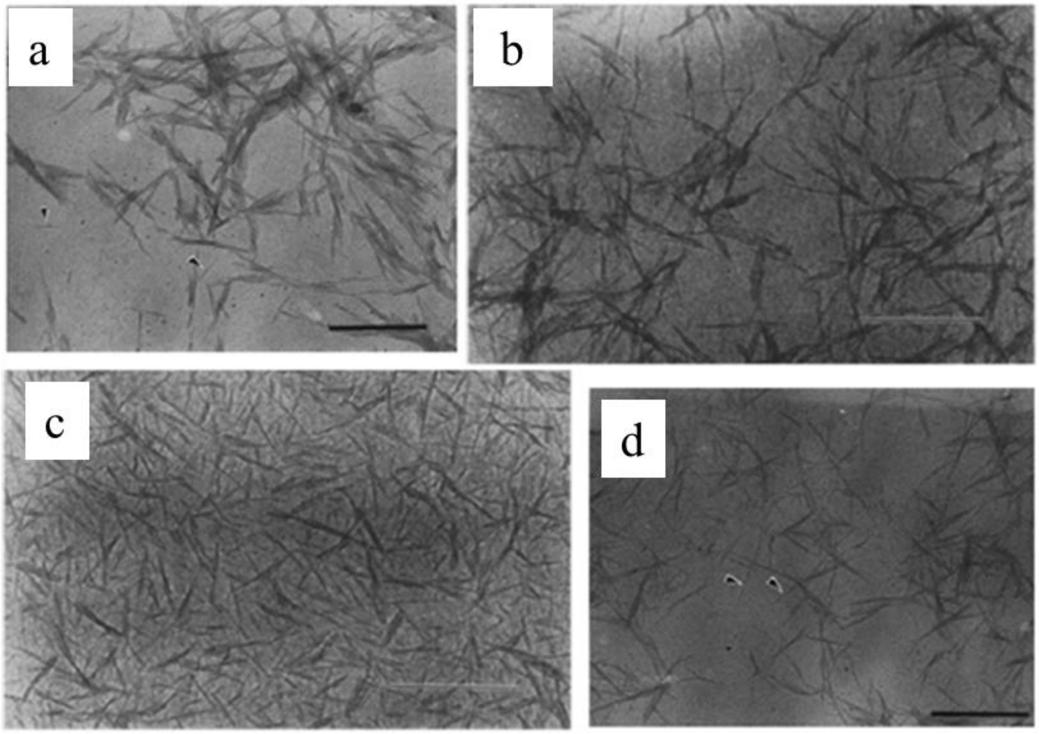

Figure 2.15 TEM images of (a) CNC-HCl, (b) CNC esterified at 40°C, (c) CNC esterified at 60°C, and (d) CNC-SA.[27, 55]

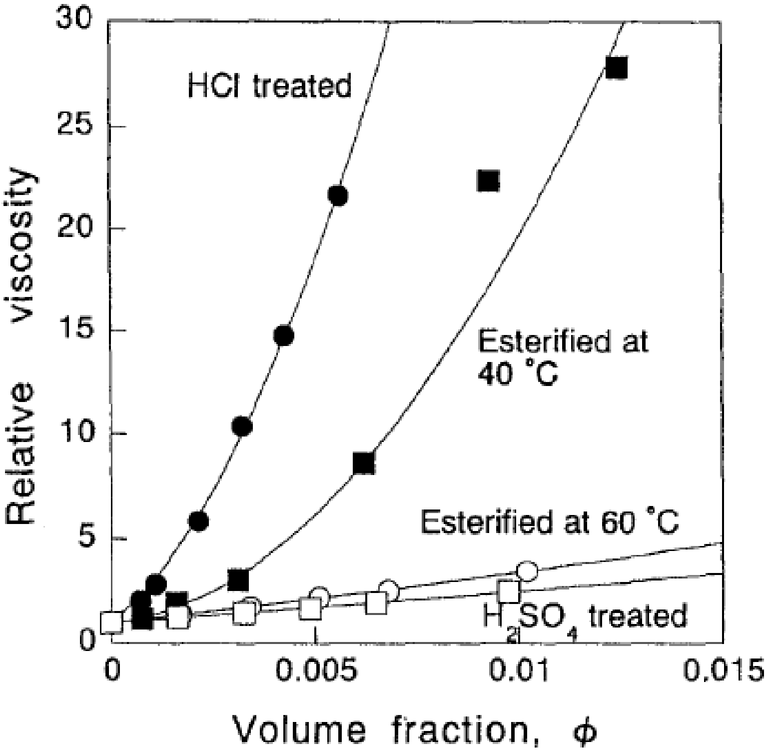

Figure 2.16 Relative viscosities of cellulose suspensions versus volume fraction.[55]

Cellulose nanocrystals prepared by mixed hydrochloric and acetic acids (CNC-AA) form initially stable suspensions during centrifugation.[28] However, Braun et. al. showed that increased hydrophobicity of these particles causes decreased colloidal stability in water and the CNC-AA precipitate over a period of weeks.[28] In comparison, CNC-HCl suspensions remain stable over this time period. The increase in hydrophobicity was verified by an increase in static contact angle when compared to CNC-HCl ($\theta_s = 18.2 \pm 1.6^o$ for CNC-HCl and 24.9 ± 0.9^o for CNC-AA). While significant mechanical agitation was necessary to suspend CNC-HCl, this was not observed for CNC-AA. This observation was reported to be consistent with multiangle laser-light scattering data, which indicates that the addition of methyl ester groups to the surface reduces hydrogen bonding and facilitates individualization of the particles.

2.3.2 Liquid Crystalline Phase Behavior of CNC

Due to the rod-like morphology of cellulose nanocrystals, dispersions of individual particles and small aggregates formed by sulfuric acid hydrolysis exhibit lyotropic liquid crystalline phase behavior. This was first observed by Marchessault et. al. in 1952 when a gel formed on the surface of a heated suspension of ramie CNC.[56] When viewed on a polarizing microscope, the gel was found to be birefringent, indicating liquid crystalline order. Further samples were obtained by centrifugation of the suspensions at 20,000 xg, resulting in dispersions with concentrations ranging from 13 to 15 wt % (8.3 to 9.7 vol %). These dispersions also exhibited birefringence when viewed between crossed polarizers. When the dispersion was dried down into a film rather large birefringent areas were observed and the structure is said to be reminiscent of the spherulitic behavior of high polymers (Figure 2.17). The liquid crystalline character of the dispersion was attributed to parallel alignment of the CNC (nematic order).

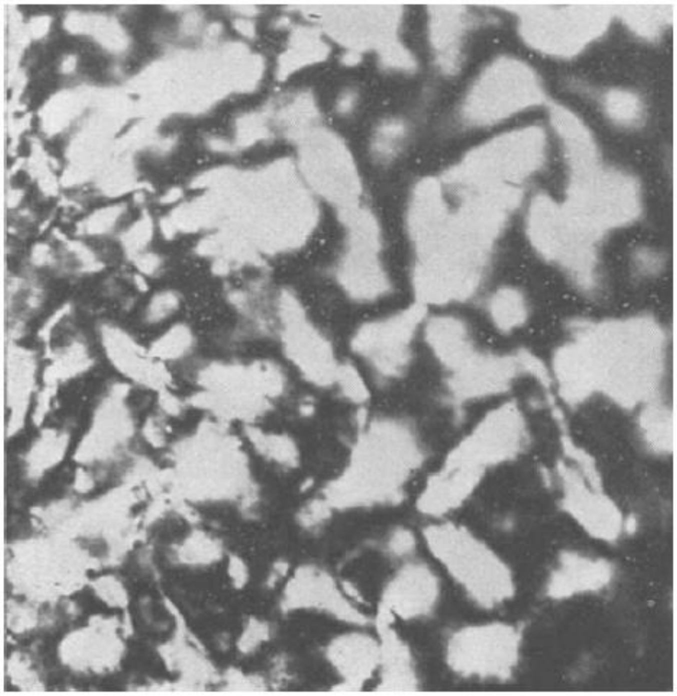

Figure 2.17 Dried down film of birefringent dispersion between crossed polarizers.[56]

Revol et. al. first reported the self-ordering of cellulose nanocrystals into stable chiral nematic phases.[12] CNC dispersions were prepared by the sulfuric acid hydrolysis of kraft wood pulp from black spruce. Upon standing at room temperature, a 3 wt % (1.8 vol %) dispersion spontaneously separated into an upper isotropic and a lower anisotropic phase. When viewed on a polarizing microscope a freshly sonicated dispersion began to form small tactoids with birefringent bands after a few minutes. With time, the tactoids settled and merged yielding fingerprint textures indicative of a chiral nematic liquid crystalline phase (Figure 2.18). The source of the chiral nematic order in CNC suspensions is still not known, but it has been hypothesized that the chirality of the cellulose fibers must somehow be transferred to the nanocrystals, possibly by a helical geometry or helical charge distribution.[57] It has been noted by Revol et. al. that the chiral nematic order was retained when these dispersions were dried into films.[58]

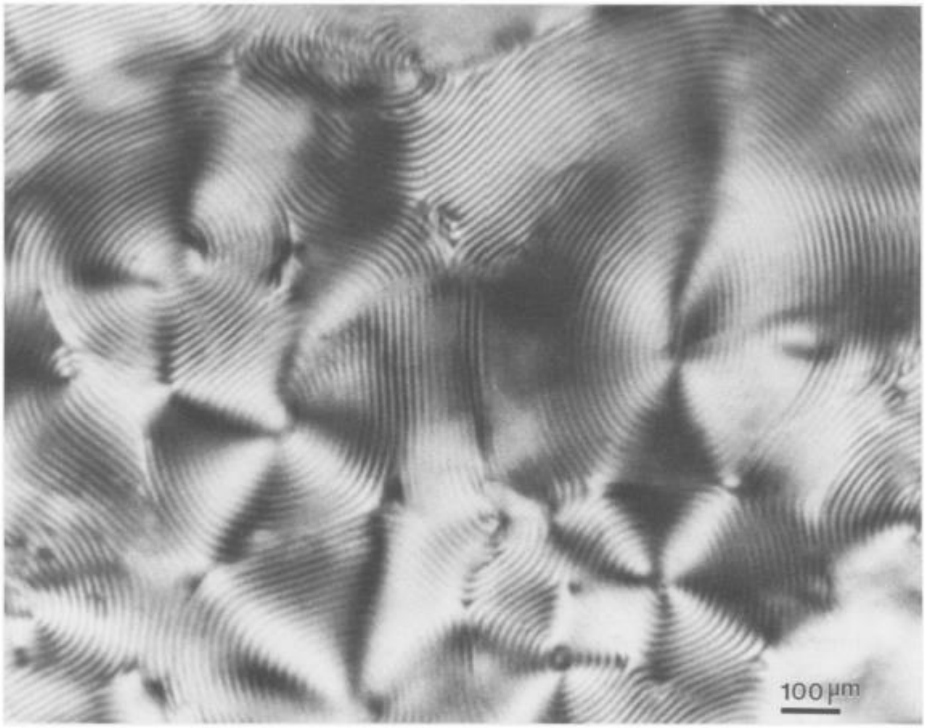

Figure 2.18 Optical micrograph between crossed polars of the anisotropic phase formed by dispersions of sulfuric acid hydrolyzed cellulose nanocrystals.[12]

The critical concentration required for the formation of a chiral nematic phase of cellulose nanocrystals in electrolyte-free aqueous dispersion depends strongly on CNC size and charge density; it can range from about 1 to 10 wt % (0.61 to 6.3 vol %).[15] Ureña-Benavides et. al. investigated the phase behavior of cotton CNC-SA dispersions (without added electrolytes) using both cross-polarized optical microscopy and rheology. At 20 ^{o}C, it was determined that the isotropic to biphasic phase transition was at 3.0 vol % (4.8 wt %) and the biphasic to liquid crystalline phase transition fell between 10.4 vol % (16.0 wt %) and 12.1 vol % (18.4 wt %). These phase transitions are sensitive to the presence of electrolytes or other molecules in the dispersion. Dong and Gray investigated the effect of eleven different counterions on ordered phase formation of cellulose nanocrystal dispersions.[59] They saw that as counterion concentration increased so did the concentration of CNC required to form an ordered phase. This behavior was also dependent on the type of counterion present. For inorganic counterions (H^+, Na^+, K^+, and Cs^+) the critical concentration increased with increasing van der Waals' radius of the counterion. The effect of organic counterions was more complicated with critical concentration dependent on both the hydrophobic interaction and steric repulsion of the counterion (Figure 2.19).

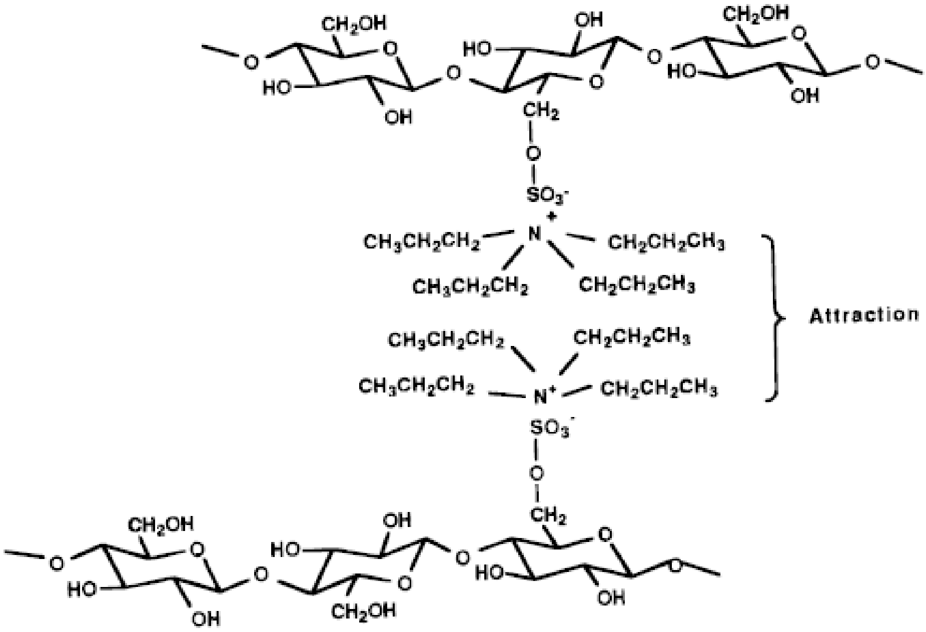

Figure 2.19 Sketch illustrating the hydrophobic interaction in cellulose nanocrystal dispersions in the presence of organic counterions.[59]

2.3.3 CNC Rheology

There is a growing body of work on the rheology of CNC dispersions.[19, 27, 60-62] The detailed rheological properties and liquid crystalline phase transitions have varied between studies due to differences in CNC size and surface chemistry, as well as differences in the exact methods used to detect the liquid crystalline phase transitions. Ureña-Benavides et. al.

and Wu et. al. both studied CNC prepared from cotton cellulose with similar average aspect ratios of 12 and 13, respectively.[19, 62] However, they reported significantly different phase transition concentrations. Ureña-Benavides observed the transition from isotropic to biphasic at 2.7 vol % and from liquid crystalline to gel at 14.5 vol %, while Wu observed these same transitions at 1.0 vol % and 3.0 vol %, respectively. Both Wu et. al. and Ureña-Benavides et. al. showed that in contrast to the rheological behavior typically associated with lyotropic liquid crystalline dispersions,[31, 63-65] there is no maximum is observed in the biphasic region of a viscosity versus concentration curve.[19, 60-62] Since similar results have been reported for hallyosite[66], a charged tubular nanoclay, and therefore may be due to changes in ionic strength with the increasing concentration. In addition, three region viscosity versus shear rate behavior is typically considered a signature of fully liquid crystalline dispersions,[42] but for CNC this behavior has been more frequently reported in the biphasic regime.[19, 60-61]

2.3.4 Small-Angle Scattering from CNC

To the authors' knowledge, only two studies have combined rheology and small-angle scattering to investigate the effects of flow on the microstructure of CNC dispersions. Orts et. al. used rheology and small-angle neutron scattering (rheo-SANS) to effect of aspect ratio on the flow induced alignment of fully liquid crystalline dispersions. They observed a transition from cholesteric to nematic alignment during flow.[67] Ebeling et. al. conducted a small-angle x-ray scattering (SAXS) experiment on liquid crystalline CNC dispersions and also saw enhanced ordering during flow.[68] Contrary to Orts et. al., at low shear rates Ebeling et. al. observed alignment in the vorticity plane at certain shear rates. Two possible explanations were presented for this behavior. The first related to the alignment of planes within the polydomain structure of the liquid crystal, while the second proposed end-over-end tumbling of the nanocrystals.

Schutz et. al. used SAXS and laser diffraction to study the packing of CNC and the pitch in the cholesteric phase of CNC dispersions over the entire isotropic to liquidic crystalline concentration range.[69] The average CNC spacing decreases from 51 nm at 1.3 vol % to 25 nm at 6.5 vol %. The pitch decreases from 15 μm to 2 μm when the concentration increases from 2.5 vol % to 6.5 vol %. The pitch as a function of concentration is shown in Figure 2.20 and CNC spacing versus concentration is shown in Figure 2.21.

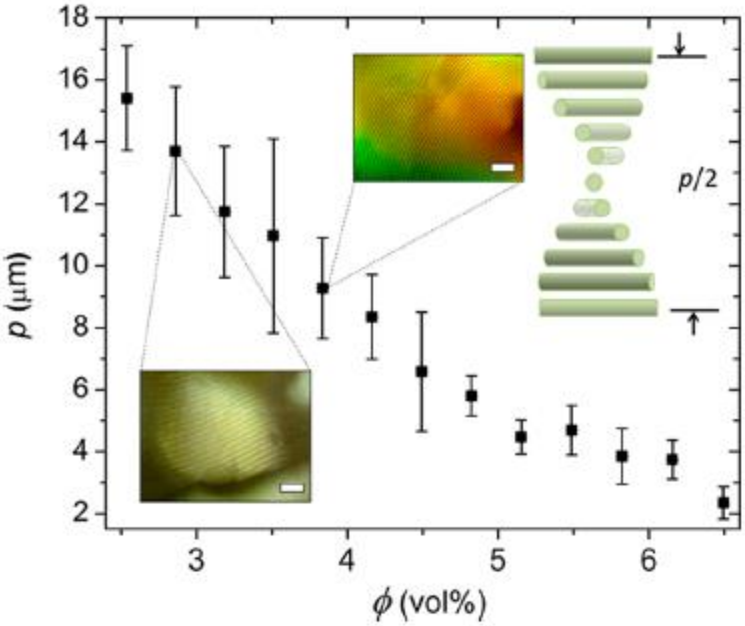

Figure 2.20 Helical pitch as a function of CNC volume fraction determined by laser diffraction.[69]

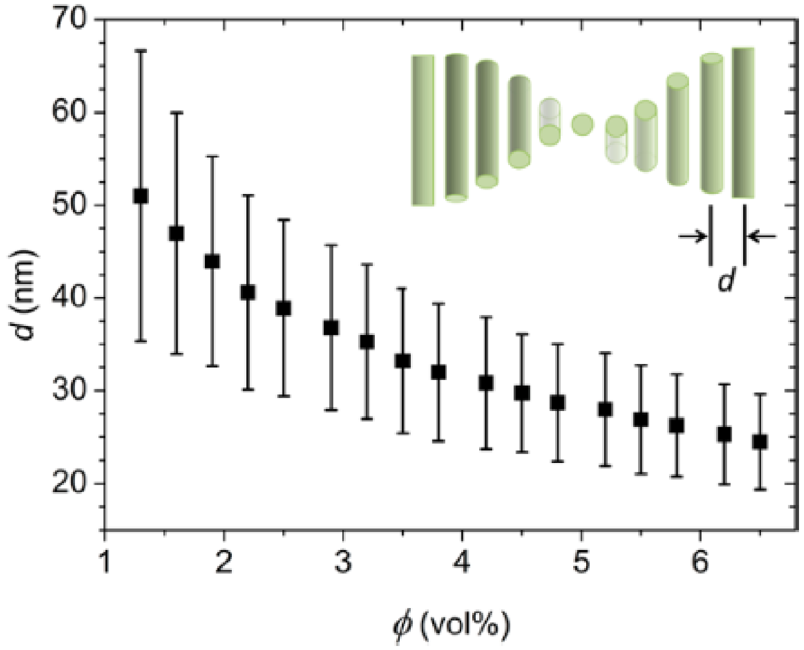

Figure 2.21 Average center-to-center separation distance for CNC as measured by SAXS.[69]

2.4 Cellulose Nanocrystal Films

Revol et. al. noted in 1992 that the chiral nematic order of a cellulose nanocrystal dispersion was retained in a dried film.[12] Pan et. al. reported an in depth study of the effect of ionic strength, temperature, suspension concentration, and magnetic field on the chiral nematic phase of cellulose nanocrystal films.[70] The addition of counterions to the CNC dispersion reduced the chiral nematic pitch and this reduction is preserved in the films. At significantly high counterion concentration, the chiral nematic phase is lost and an isotropic film results. Increased temperature also resulted in reduced chiral nematic pitch while an increase in dispersion concentration correlates to an increase in pitch. Drying the films in the presence of a magnetic field resulted in an increased chiral nematic pitch for dispersion concentrations that exhibit liquid crystallinity. It did not, however, promote the formation of a chiral nematic phase in low concentration dispersions. The increase in chiral nematic pitch is attributed to the magnetic alignment of cellulose nanocrystals given their nonzero magnetic susceptibility.

2.4.1 Aligned CNC Films

While much of the literature has focused on magnetic and electrical alignment of CNC, ordered cellulose nanocrystal films can also be prepared by shear alignment of liquid crystalline dispersions.[71] This dissertation focuses on the effects of shear on alignment. Unlike magnetic and electrical processing, shear is inherent in almost all fluid phase manufacturing processes. In one literature example, Hoeger et. al. used a convective shear assembly (Figure 2.22) to prepare aligned CNC films and looked at the effect of substrate material, withdrawal speed, and cellulose concentration on alignment.[72] It was determined that the induced orientation of the CNC was a balance of many forces including hydrodynamic (shear and drag), Brownian, surface tension (capillary forces), and electrostatic interactions (between the CNCs and the substrate). Specifically, substrates such as gold, with opposite charge as the CNC resulted in better alignment in the films. Higher concentration dispersions, where the CNC were partially aligned by liquid crystalline self-assembly, resulted in better macroscopic alignment in the film. Intermediate withdrawal rates resulted in the best alignment; this is explained by the interaction of hydronamic and capillary forces. Figure 2.23 shows an AFM image of a highly aligned form prepared using this method.

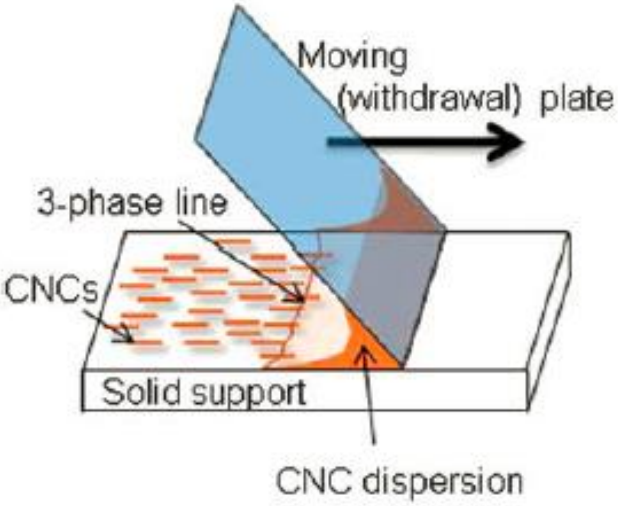

Figure 2.22 Experimental setup for convective-shear assembly.[72]

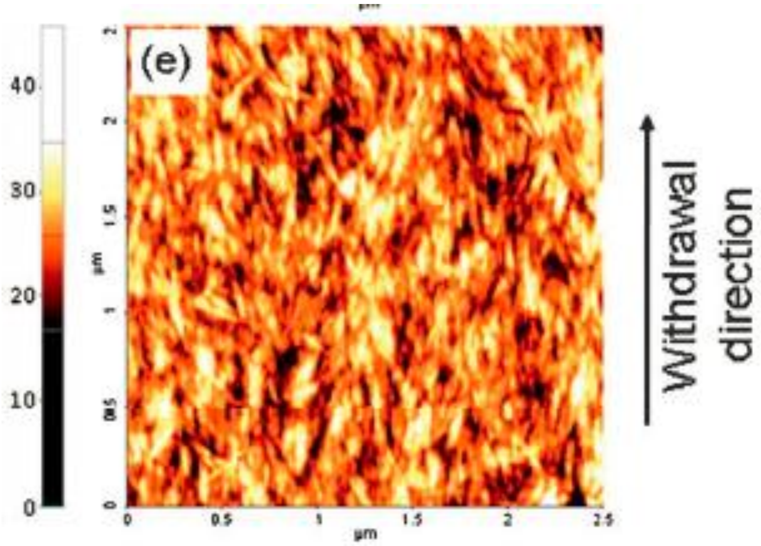

Figure 2.23 AFM of film prepared on a silica substrate from a 4.5% CNC dispersion at intermediate withdrawal rate.[72]

Reising et. al. prepared films of both randomly aligned and flow-aligned CNC.[73] They studied the effects of dispersion pH and shear rate on the order parameter and mechanical properties of the films. All sheared films were cast from dispersions with concentrations just below the gel point. Mechanical properties were investigated both parallel and perpendicular to the flow direction in flow-aligned films. They found that the degree of alignment in the films increased with higher casting shear rates and higher suspension pH. The maximum orientation of S = 0.53 was achieved for CNC suspensions having a neuteral pH and produced using a shear rate of 100 s^{-1}. The elastic modulus of the films scaled with degree of alignment, and was highly anisotropic. The maximum modulus measured was 31.5 GPa in the parallel direction, corresponding to 7.0 GPa in the perpendicular direction. The order parameter and mechanical properties of their films, made at low pH (CNC-l) and neutral pH (CNC-n), are shown in Table 2.3.

Table 2.3 Order parameter and mechanical properties of CNC films. CNC-l is CNC with low pH, CNC-n is CNC with neutral pH, A (axial) refers to the direction parallel to flow, T (transverse) refers to the direction perpendicular to flow, and the numbers in brackets are standard deviation.[73]

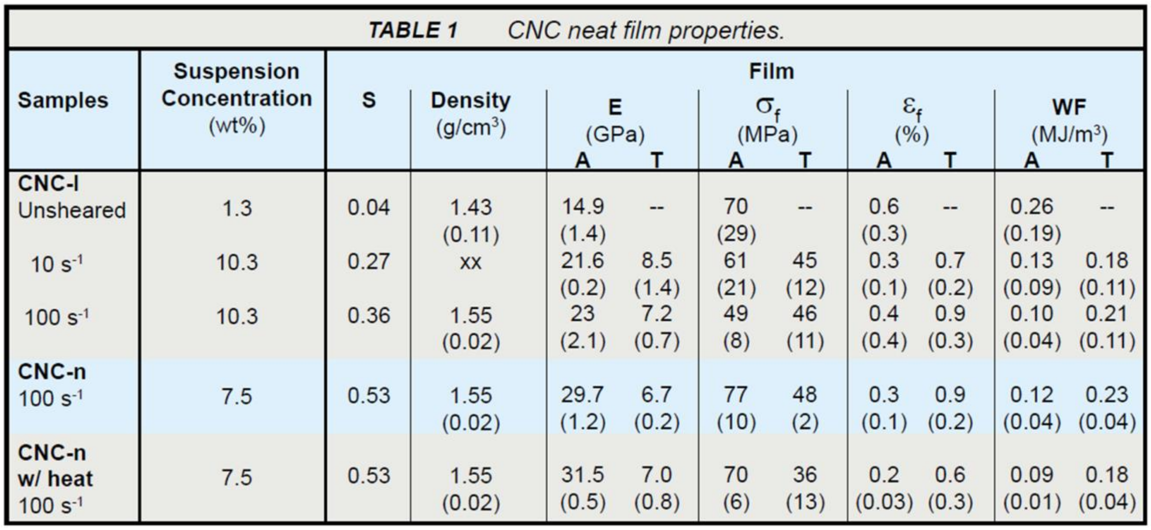

TABLE 1 *CNC neat film properties.*

Samples	**Suspension Concentration** (wt%)	**Film**									
		S	**Density** (g/cm^3)	**E** (GPa)		σ_f (MPa)		ε_f (%)		**WF** (MJ/m^3)	
				A	**T**	**A**	**T**	**A**	**T**	**A**	**T**
CNC-l Unsheared	1.3	0.04	1.43 (0.11)	14.9 (1.4)	--	70 (29)	--	0.6 (0.3)	--	0.26 (0.19)	--
10 s^{-1}	10.3	0.27	xx	21.6 (0.2)	8.5 (1.4)	61 (21)	45 (12)	0.3 (0.1)	0.7 (0.2)	0.13 (0.09)	0.18 (0.11)
100 s^{-1}	10.3	0.36	1.55 (0.02)	23 (2.1)	7.2 (0.7)	49 (8)	46 (11)	0.4 (0.4)	0.9 (0.3)	0.10 (0.04)	0.21 (0.11)
CNC-n 100 s^{-1}	7.5	0.53	1.55 (0.02)	29.7 (1.2)	6.7 (0.2)	77 (10)	48 (2)	0.3 (0.1)	0.9 (0.2)	0.12 (0.04)	0.23 (0.04)
CNC-n **w/ heat** 100 s^{-1}	7.5	0.53	1.55 (0.02)	31.5 (0.5)	7.0 (0.8)	70 (6)	36 (13)	0.2 (0.03)	0.6 (0.3)	0.09 (0.01)	0.18 (0.04)

2.4.2 Cholesteric CNC Films

After their discovery of cholesteric structure in CNC films, Revol et. al. revealed in a patent that the chiral nematic director of these films is oriented perpendicular to the substrate on which the film is dried allowing for optically active films.[58] When the chiral nematic pitch of the film is on the order of the wavelength of visible light iridescent colors are reflected. The relationship of the pitch to the wavelength of the reflected light λ is given by Equation 2.8, where n is the average refractive index of the material, P is pitch, and θ is the angle of the incident light to the helical axis.

$$\lambda = 2nPcos(\theta) \tag{2.8}$$

For example, cholesteric ordering of chitin causes the iridescent beetle *plusiotis boucardi* to reflect orange colors in regions where P = 370 nm and green colors in regions where P = 310 nm.[74] The reflection band of CNC films can be tailored by modifying the ionic strength of the dispersion, desulfating the cellulose nanocrystals, or varying cellulose nanocrystal size. Since, a number of studies have been conducted to further refine helix alignment and control pitch in CNC films.

In a recent study, Dumanli et. al produced multicolored cholesteric CNC films by the slow evaporation of CNC dispersions on polystyrene substrates.[75] These films exhibited a polydomain texture where different domains had different reflectance colors (Figure 2.24). Scanning electron microscopy (SEM) was used to measure the pitch in each domain and these values were compared to calculated values from the reflectance wavelength (Table 2.4). The pitch values measured by SEM were very consistent with those measured by reflectance.

Park et. al. reported a rotational shear method that guides the helix formation and yields dramatically improved uniformity in CNC films.[76] By varying the rate of rotation, they were able to control the reflectance color exhibited by the films. This method resulted in films with highly uniform pitch, and little variation between domains.

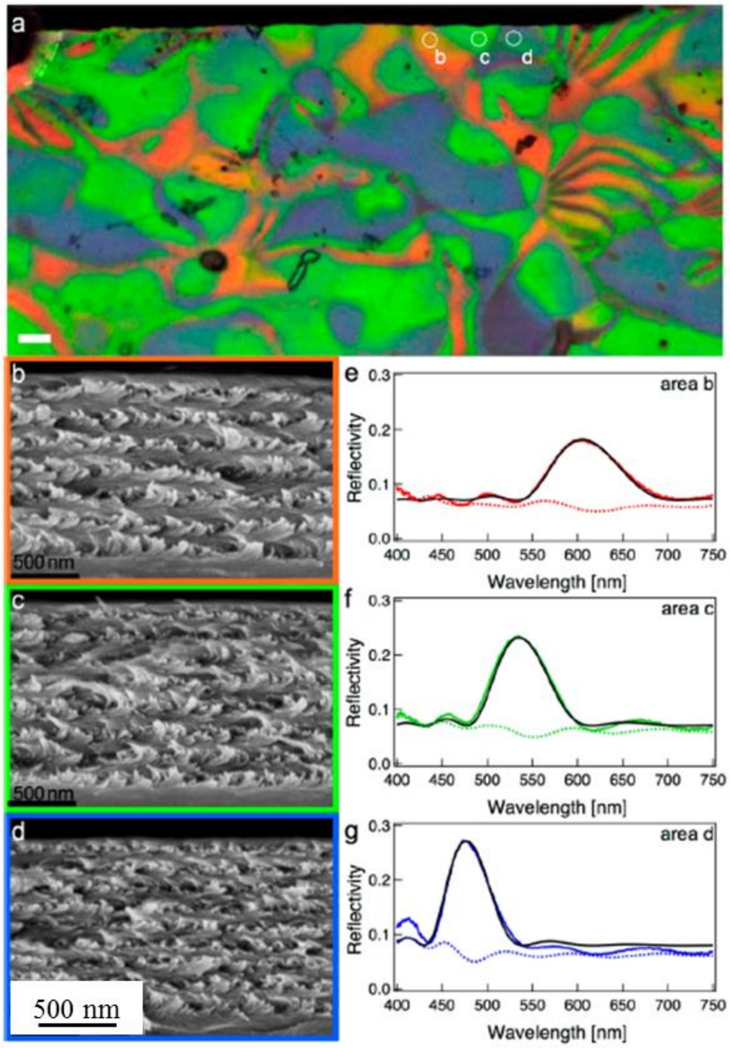

Figure 2.24 Correlation of optical and electron microscopy and the reflectance spectra of different domains.[75] a) Reflected cross-polarized image of CNC film with white circles showing areas b, c, and d from cross-sectional SEM images (b-d) and corresponding reflectance spectra (e-f) were acquired.

Table 2.4 Cholesteric pitch of different domains in CNC films as determined from the cross-sectional SEM images.[75] Domains correspons to domains referenced in Figure 2.24.

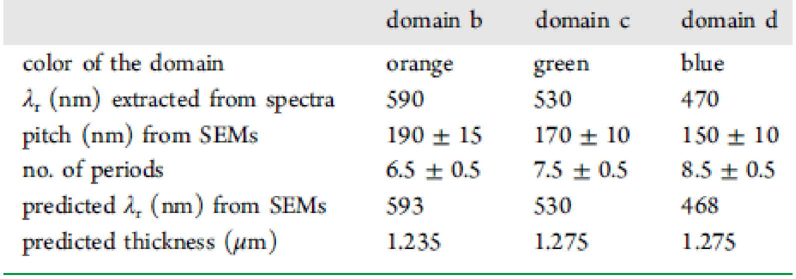

	domain b	domain c	domain d
color of the domain	orange	green	blue
λ_r (nm) extracted from spectra	590	530	470
pitch (nm) from SEMs	190 ± 15	170 ± 10	150 ± 10
no. of periods	6.5 ± 0.5	7.5 ± 0.5	8.5 ± 0.5
predicted λ_r (nm) from SEMs	593	530	468
predicted thickness (μm)	1.235	1.275	1.275

Chapter 3 Experimental Section

3.1 Cellulose Nanocrystal Dispersion Preparation

In the course of this work, CNC from a number of batches with varying cellulose sources and reaction conditions were used. In the work on nematic films for MEMS applications, CNC of were produced from Whatman ashless filter aid (cotton cellulose). Sulfuric acid hydrolyzed (CNC-SA) was prepared in our lab at Auburn, while our collaborators from the Kitchens Group at Clemson University, prepared acetic acid hydrolyzed (CNC-AA) and hydrochloric acid hydrolyzed (CNC-HCl). In the later part of the work, on chiral films for optical applications, CNC-SA became commercially available in large batches, and were purchased from the US Forest Service's Cellulose Nanomaterials Pilot Plant ant the Forest Products Laboratory in Madison, WI. In order to minimize the impacts of batch to batch variation, each portion of this work was done using CNC from a single batch. A schematic showing the resulting surface chemistry from each type of hydrolysis is shown in Figure 3.1. Since the majority of the work was done with CNC-SA and CNC-SA is not a standard term in the literature, all CNC were sulfuric acid hydrolyzed unless specifically noted.

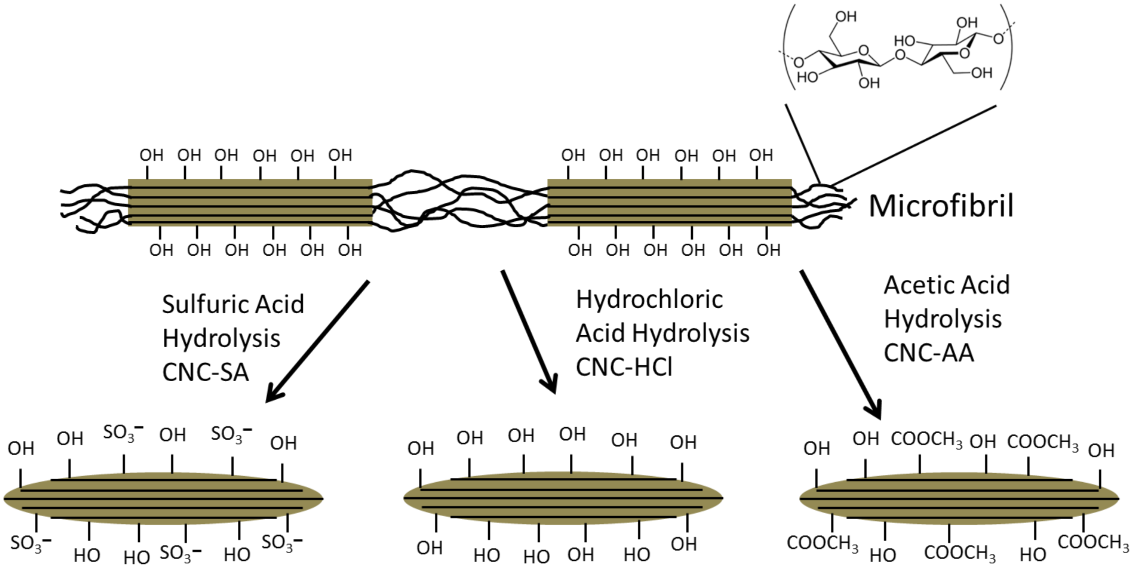

Figure 3.1 Schematic of CNC production using different types of acid ahydrolysis.

3.1.1 CNC-SA Isolation from Cotton Cellulose

CNC were isolated from Whatman ashless filter aid (cotton cellulose) using established methods.[24,21] The cellulose was hydrolyzed by continuous stirring in 64 wt % sulfuric acid at 45^{o}C for 50 minutes. For each gram of cellulose, 17 ml of sulfuric acid was used. After 50 minutes the reaction mixture was quenched with an equal volume of cold deionized water (DIW). The reaction mixture was then centrifuged at 10,800 xg for 5 minutes and the supernatant was discarded. The precipitate was re-dispersed in deionized water (DIW). The washing step was repeated 3 times. The resultant CNC slurry was dialyzed against DIW until the pH remained constant. To disperse the nanocrystals the mixture was sonicated using a Sonics VC750 ultrasonic processor at 60% amplitude for a total of 35 minutes in 5 cycles of 7 minutes on and 2 minutes off. The dispersion was allowed to evaporate at ambient conditions, with samples taken at the desired concentrations.

3.1.2 CNC-HCl and CNC-AA Isolation from Cotton

Whatman ashless filter paper (cotton cellulose) was soaked overnight in 13.3 ml DIW per g cellulose for CNC-HCl or in 22.5 ml of 100% acetic acid per g cellulose for CNC-AA. For CNC-HCl 3.5 ml of 36% HCl per g cellulose was added and the mixture was heated to 103 ^{o}C and allowed to react for 60 minutes with a reflux condenser. For CNC-AA 2.5 ml of DIW and 80 µL HCl per g cellulose were added and the mixture was heated to 105 ^{o}C and allowed to react for 10 hours. For both CNC-AA and CNC-HCl, the reaction mixture was then cooled to room temperature in an ice bath. The reaction mixture was then centrifuged at 8,000 xg for 3 minutes and the supernatant was discarded. The precipitate was re-dispersed in deionized water (DIW). The washing step was repeated 3 times. The resultant slurry was sonicated for a total of 35 minutes in 5 cycles of 7 minutes on and 2 minutes off. Water was then added to double the volume and the mixture was centrifuged and washed until a turbid supernatant was observed. The supernatant was collected and the process was repeated until no CNC could be recovered in the supernatant. The supernatant dispersion was allowed to evaporate at ambient conditions, with samples taken at the desired concentrations.

3.1.3 Commercial CNC-SA

For the work in Chapter 5, spray dried cellulose nanocrystals, produced by sulfuric acid hydrolysis (CNC-SA) were obtained from the US Forest Service's Cellulose Nanomaterials Pilot Plant at the Forest Products Laboratory. A vortex mixer was used to mix approximately 12 g of CNC and 88 g of deuterium oxide (D_2O). The mixture was then placed in an ice bath and sonicated using a Sonics VC750 ultrasonic processor at 60%

amplitude for a total of 35 minutes in 5 cycles of 7 minutes on and 2 minutes off. The mixture was stirred by hand during the off cycles. The sample concentration was measured by thermogravimetric analysis (TGA) and the dispersion was diluted to obtain samples of the desired concentrations.

3.1.4 Commercial CNC-SA/Polymer Dispersions

The CNC-SA/polymer dispersions used in Section 4.4 were made by first adding the polymer additive to 13 wt % (8.35 vol %) CNC dispersion in a 20 mL glass vial with a lid. The CNC was obtained in slurry form from the US Forest Service's Cellulose Nanomaterials Pilot Plant at the Forest Products Laboratory. To see how a polymer additive affected the film properties, polyethylene oxide (PEO) with molecular weights of 100,000, 1,000,000 and 8,000,000 were mixed into the dispersion. The PEO was added so that the dispersion resulted in 2% or 5% weight of the additive. After addition, the dispersion was first mixed in a vortex mixer for 5 minutes and then left undisturbed overnight to allow the additive to fully dissolve into the dispersion. After 24 hours, the dispersion was again mixed for 5 minutes with a vortex mixer. Flocculated dispersions were prepared by dropwise addition of 10 vol % HCl until the cellulosic material in the dispersions flocculated. Flocculation was determined by the physical transition of the dispersion from translucent to opaque. The dispersion was mixed with the vortex mixer after every drop of HCl was added. Before the casting of each film, the dispersion was again mixed using the vortex mixer.

3.2 Cellulose Nanocrystal Characterization

3.2.1 Determination of Size Distribution

A Pacific Nantechnology Nano-R SPM was used to perform atomic force microscopy (AFM) to determine the size distribution of the CNC-SA used in this work. Approximately 10 μL of 0.05 vol % CNC-SA was pipetted onto a freshly cleaved mica surface. The dispersion was allowed to sit for 5 minutes on the mica surface, which was then blown dry with dry air, leaving behind adsorbed CNC on the surface. The AFM was operated in static, noncontact mode. Each scan was of a 5 μm^2 area of a resolution of 1024 and a scan speed of 0.25 Hz. An image of the tip was obtained using a porous aluminum standard surface and Gwyddion's blind tip estimation algorithm; this image was used to deconvolute the shape of the particles from the geometry of the tip. The length, width, and height were measured for a minimum of 100 CNC.

3.2.2 Determination of Sulfate Content

The extent of sulfate functionalization of the CNC-SA was determined by conductiometric titration using a Suntex SC-170 conductivity meter with a Cole-Parmer 19050-66 conductivity cell. An aqueous solution of 10 mM sodium hydroxide (NaOH) was added in 100 µl increments to 200 ml of 0.75 mg/ml CNC-SA. The mixture was stirred and allowed to equilibrate after each NaOH addition. The conductivity measurements were corrected for dilution effects and plotted against added volume of NaOH solution. The equivalence point was determined to be the minimum in the conductivity curve.

3.3 Film Casting

Aligned CNC films in Section 4.3.4.2 were prepared by doctor blade coating on glass microscope slides using a Gardco Microm II film applicator. Doctor blade coating applies unidirectional shear to the dispersion at a constant shear rate. A droplet of the CNC dispersion was transferred to the top of the glass slide using a spatula. The dispersion was then drawn down the substrate with the blade of the film applicator. The gap height was controlled using the adjustable micrometers on the film applicator. Wet thicknesses ranging from 50 to 200 μm were used with drawdown speed adjusted to keep the shear rate approximately 100 s^{-1} for all films. After casting, the films were allowed to dry overnight at ambient conditions. Drop cast films were prepared by pipetting 200 μL of dispersion onto a polystyrene petri dish and allowing it to dry.

For CNC/Polymer films in section 4.4 a droplet of the dispersion was placed on packing tape and sheared with Gardco Microm II film applicator at a shear rate of 5 s^{-1} and a gap height of 0.5 mm. To ensure consistency for all of the sheared films, a metal rod attached to a syringe pump was used to provide a constantly velocity of the blade for each film. Packing tape was used as the substrate for easy removal of the films. After five hours of drying at ambient conditions, the films were cut to an approximate width of 5 mm and approximate length of 4 cm. The films were cut so that the long axis of the film was either parallel or perpendicular to the flow in order to test for anisotropic mechanical properties.

3.4 Characterization Methods

3.4.1 Optical Microscopy

Optical microscopy is an important method for exploring both dispersion state and liquid crystallinity of rod like nanomaterials. Due to their small size, individual CNC cannot be observed with an optical microscope, even at high magnification. This is because the particle size is smaller than the resolution of the scope. Resolution is the smallest resolvable distance between two objects and is determined by Equation 3.1.

$$r = \frac{\lambda}{2NA} \tag{3.1}$$

Here, λ is the wavelength of the light, usually assumed to be 550 nm, and NA numerical aperture of the microscope. The real world maximum value of r is approximately 250 nm. Aggregates and liquid crystalline domains within the dispersion can be much larger than this and can be directly viewed under a light microscope. This method was used to qualitatively assess the dispersion state of each CNC sample.

Liquid crystals are known to exhibit birefringence, meaning they have two indices of refraction. Therefore, incident light on a liquid crystalline sample will be split and take two different paths through the sample. After exiting the sample this light becomes out of phase and recombines into a different polarization state. This phenomenon is taken advantage of in cross-polarized optical microscopy for the characterization of liquid crystals. When an isotropic material is viewed between crossed polarizers no light can pass through the polarizers and the sample appears completely black; this is known as extinction. However, for a liquid crystalline sample the change in polarization state allows some light to pass through the second polarizer. By rotating the sample between the polarizers the angle of polarization changes and the sample will appear to change from bright to dark. A variety of patterns have been noted for different liquid crystalline phases. Of particular importance for this research is the fingerprint texture that is characteristic of cholesteric liquid crystals.

In this work images were taken using a Nikon Eclipse 80i optical microscope with a LU Plan Fluor 20x/0.45NA Nikon objective lens. Samples were prepared by sandwiching the dispersion between a microscope slide and coverslip either with or without a 120 μm SecureSeal Imaging Spacer. When an imaging spacer was not used, the cover slip was tightly sealed using fingernail polish or hot glue. For shearing CNC dispersions, the microscope was equipped with a Linkam CSS450 Optical Rheology Stage. The Linkam Optical Rheology Stage allows for images to be take of the flow-vorticity plane as shown in Figure 3.2. Shear cell images were taken at room temperature with an L Plan SLWD 20x/0.35NA Nikon objective lens. Crossed polarizers were used for all images, unless otherwise noted, with the shearing direction oriented at 0^o or 45^o with respect to the polarization axis, as indicated.

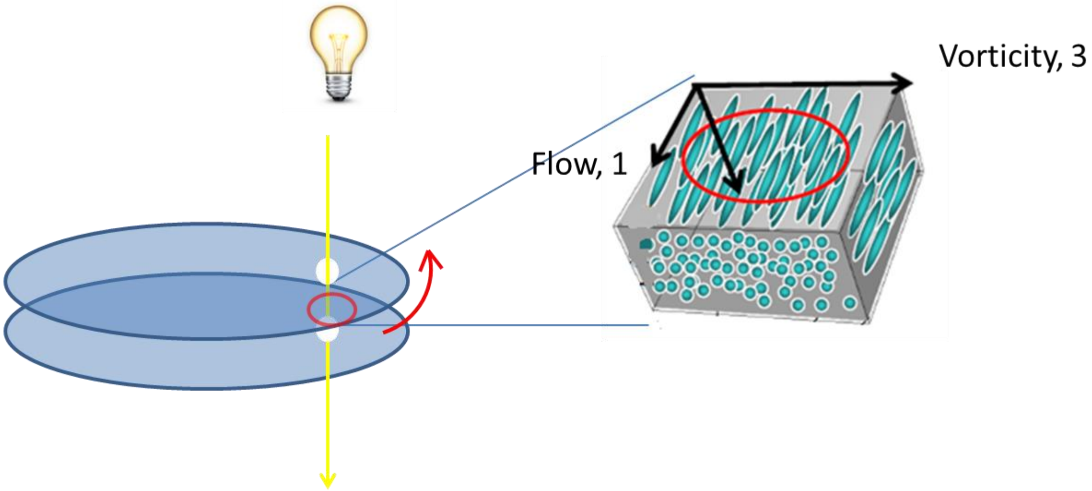

Figure 3.2 Schematic of flow plane visible in the Linkam Shear Cell.

3.4.1.1 Optical Contrast Measurements

A Nikon DS-Ri2 microscope camera mounted on a Nikon Eclipse 80i optical microscope equipped with cross-polarizers was used to measure light intensities for optical contrast (*OC*) measurements. The intensity of the light transmitted through the crossed polarizers was calculated by Nikon Elements imaging software by averaging the RGB intensities of each pixel of an 8-bit image. For consistency, the maximum intensity (I_{max}) was always assumed to be when the flow direction was oriented 45^{o} with respect to the polarizer axis, while the minimum intensity (I_{min}) was when the flow direction was in line with the polarizer. Equal exposure time was used for both I_{max} and I_{min} measurements.

3.4.2 Rheology

CNC dispersions were analyzed using an Anton Paar MCR301 rotational rheometer. For each concentration, steady shear viscosity versus shear rate curves were generated from 0.01 to 100 s^{-1}. The time to steady state for each concentration was determined by a start-up flow test at 0.01 s^{-1}, the sample time was then decreased linearly with increasing shear rate. Some points for the low concentration dispersions were below the sensitivity of the torque transducer; these points are not shown. Oscillatory measurements were performed within the linear viscoelastic region (LVE) for each dispersion from 0.1 to 100 rad/s (0.01 to 100 rad/s for the 15.8 vol % sample). The LVE was determined by amplitude sweeps at a constant frequency of 10 rad/s. Since small changes in concentration can cause large variations in rheological properties, measurements were made at 10 $^{\circ}$C and an evaporation blocker was used. The low viscosity isotropic sample was tested using a Mooney-Ewart fixture geometry, while the biphasic, liquid crystalline and gel samples were tested using 50 mm parallel plates. Both geometries were tested for the biphasic dispersion to ensure no experimental artifacts were present.

3.4.3 Small-Angle Neutron Scattering

All neutron scattering experiments were conducted in collaboration with Dr. Kathleen Weigandt on the NGB 30m small angle neutron scattering (SANS) beam line at the NIST Center for Neutron Research in Gaithersburg, MD. For flow experiments, the instrument was configured with 6 Å neutron wavelength and a sample to detector distance of 8.5 m. For samples at rest, two additional configurations were used; 6 Å neutron wavelength and sample to detector distance of 1.9 m, and 8.4 Å neutron wavelength and sample to detector distance of 13.7 m. The sample environment was an Anton Paar MCR501 rotational rheometer with a titanium cup and bob (48.0 mm bob diameter and 50.0 mm cup internal diameter). All measurements were performed at 10 ^{o}C. Measurements were performed in both radial and tangential arrangements in order to probe the microstructure in the flow-vorticity and gradient-vorticity planes, respectively. A schematic of the Couette cell and the flow planes is shown in Figure 3.3. The scattering data was reduced to an absolute scale using the standard NIST Igor procedures.[77] Due to the complicating effects of the curved transmission path in the tangential configuration, the tangential scattering data was scaled to match the absolute radial scattering intensity in the common (vorticity) direction.

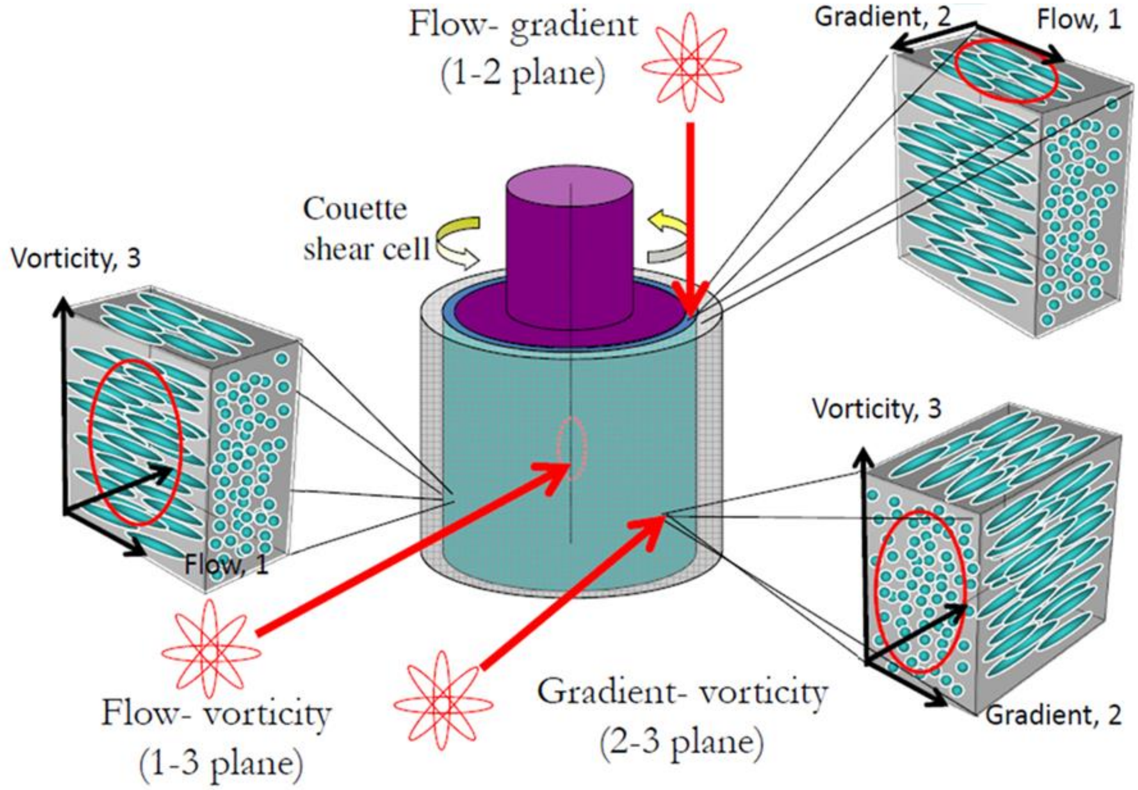

Figure 3.3 Schematic of flow planes that are accessible by rheo-SANS.[78]

3.4.4 Microspectrophotometry

Visible spectra were obtained from the CNC films using a CRAIC technologies 20/20 PV microspectrophotometer. Samples were placed between crossed polarizing films and data was collected from 400 to 700 nm. Images of the sample area were taken using an Ultrafluar 10x/0.2NA Quartz Zeiss objective lens.

3.4.5 Confocal Microscopy

Confocal microscopy was conducted using a Nikon A1R MP Confocal Microscope at the Auburn University Research Instrumentation Facility. For confocal microscopy, CNC were labeled with 5-(4, 6-dichlorotriazinyl) aminofluorescein (DTAF) using established methods.[79] All images were taken using a 40x objective and an excitation wavelength of 543 nm. 3D images of the z-stacked images were rendered using Nikon Elements software.

3.4.6 TGA-FTIR

Thermogravimetric analysis (TGA) is a testing method typically used to determine the thermal decomposition behavior of a material. Specifically, the mass of a sample is monitored as a function of temperature as it is subjected to a controlled temperature profile in a controlled atmosphere. TGA can also be used to measure the concentration of certain components in a mixture. The TGA used in this research was a TA Instruments (New Castle, DE) TGA Q50. It consists of a high-precision balance with a platinum pan for loading the sample. The balance is enclosed in a small furnace which can be purged with inert gas such as argon. Inert gas can be used to prevent combustion or to prevent oxidation of metal samples. In this research, TGA was used to determine the concentration of CNC dispersions and to study the thermal decomposition behavior of each type of CNC.

TGA can be coupled with Fourier transform infrared spectroscopy (FTIR) to determine the chemical composition of thermal decomposition products. FTIR takes advantage of the fact that molecular bonds vibrate at different frequencies depending on the chemical elements and type of bond. Vibrations can be caused by the absorption of infrared (IR) light of energy (determined by wavelength) equal to the difference in energy of two vibrational states. In a FTIR spectrometer a beam containing multiple wavelengths of IR light is used. This beam first shines through a Michelson interferometer where mirrors are used to cause wave interference and modulate the spectrum of the light. Raw data of absorption versus mirror position, called an interferogram, is collected and processed using a fast Fourier transform algorithm to produce the spectrum. The FTIR used in this research was a Thermo Scientific (Waltham, MA) Nicolet iS10 FTIR equipped with TGA-IR interface. The TGA is connected to the FTIR via a heated flow line. The decomposition gasses are analyzed in a gas flow cell contained within an oven to prevent the gasses from condensing.

3.4.7 Atomic Force Microscopy

Atomic force microscopy (AFM) is a form of scanning probe microscopy with resolution on the order of fractions of a nanometer. The AFM consists of a cantilever with a probe tip at its end that is used to scan the material surface. When operated in non-contact mode, as in the current research, the cantilever is oscillated at a frequency just above its resonance frequency and is brought very close to the sample surface. Electrostatic forces between the surface and the cantilever dampen the oscillation of the cantilever. Deflection of the cantilever is measured by reflecting a laser beam off the back of the cantilever onto a position sensitive detector.   A feedback loop is used to maintain constant oscillation of the cantilever by adjusting the tip-to-sample distance. Measurement of the tip-to-sample distance at each point along the surface allows the AFM to develop a topographical image of the sample surface.

In this research, AFM was used to compare the roughness of films prepared from different CNC samples as well as photoresist roughness after plasma treatment. Additionally, AFM was used to determine whether CNC was dispersed as individuals or as a dispersion of aggregates by allowing CNC form a dilute dispersion to adsorb onto a molecularly smooth substrate. A Pacific Nanotechnology Nano-R SPM AFM and an AFM Workshop TT-AFM were used in this work.

3.4.8 Contact Angle Measurement

Water contact angle measurements were used to determine the wettability of photoresist surfaces after various treatments. The contact angle is measured as the interior angle between the wetted surface and the water droplet. Surfaces with water contact angles below 90^o are considered to be hydrophilic, while above 90^o are hydrophobic. A schematic of the contact angle is shown in where θ is the contact angle. Water contact angles were measured using a Rame-Hart Instrument Co. (Succasunna, NJ) standard goniometer. The setup consists of a CCD digital camera, a backlight source, a moveable sample stage, and a liquid injection syringe calibrated to deliver controlled liquid drop sizes to the sample surfaces. DROPimage software was used to analyze images of the water droplet and determine the contact angle.

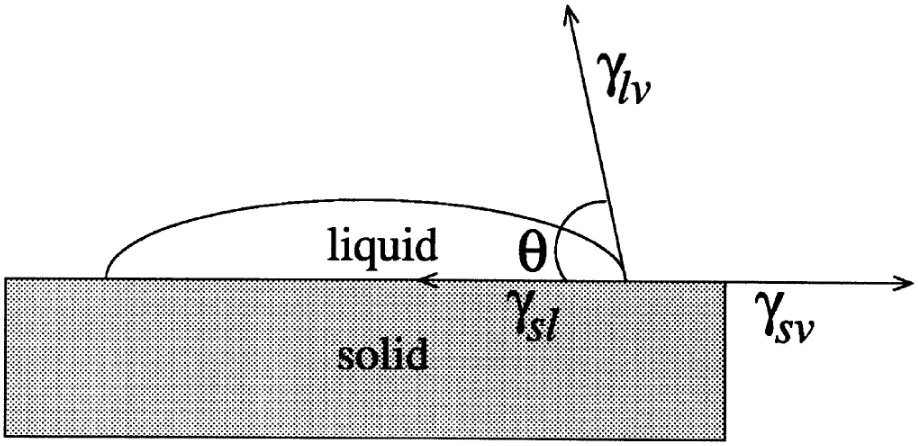

Figure 3.4 Schematic of contact angle measurement where θ is the contact angle.[80]

3.4.9 Mechanical Testing

An Instron 5565 Tensile Tester was used to obtain stress versus strain curves for each film with a crosshead speed of 0.5 mm/min with a 100 N load cell. From these curves the tensile strength, Young’s modulus, and toughness were measured for each film.. To prepare each film for tensile testing, paper holders were placed on the ends of the film with Gorilla Glue before being placed into the tensile tester.

3.5 Microelectromechanical System Fabrication

3.5.1 1st Generation MEMS

Cellulose nanocrystal MEMS were fabricated using a simple surface micromachining technique in which the structural layer was deposited and etched on top of a standard 4” silicon substrate. A layer of photoresist on the silicon substrate was first deposited and patterned with holes to enable anchoring of the devices to the substrate. Next a cellulose nanocrystal film was applied followed by another photoresist layer. An upper photoresist layer was subsequently deposited and patterned and the exposed cellulose was etched using oxygen plasma. Finally, the remaining photoresist was removed with acetone leaving the CNC test devices on the substrate.

Photoresist adhesion was promoted by priming the silicon substrate or CNC film with hexamethyldisilazane (HMDS) vapor. The wafer was placed in a closed desiccator with a small amount of liquid HMDS for 5 minutes, where HMDS vapors react with the surface to form a hydrophobic layer. Spin coating was used to deposit a film of AZ Electronic Materials P4620 photoresist on the wafer. A Brewer Science CE 100 spin coater was used. The photoresist, a viscous cresol novolak solution, was dispensed in the middle of the silicon wafer and was spread by spinning up to 500 rpm for 5 s at a ramp rate of 100 rpm/s. The photoresist film was thinned to the desired thickness by spinning at between 2000 and 5000 rpm for 25 s with a ramp rate of 500 rpm/s. The thickness of the film was determined by the final spin speed. Excess solvent was removed by soft baking on a hot plate at 110^{o}C for 1.5 to 3 min depending on the thickness of the photoresist film.

The photoresist layers were patterned by photolithography. AZ P4620 is a positive photoresist containing a UV sensitive diazonaphthaquinone additive. The additive renders UV exposed regions of the photoresist film preferentially soluble in a developer solution. The wafer was exposed to UV light through a custom designed hard photomask (chrome on quartz) which blocks some UV light to produce the desired pattern. A Karl Suss MA/BA 6 mask aligner was used with exposure energy of 50 mJ/cm^{2}. The exposure time was varied depending on the thickness of the photoresist layer. The exposed regions of photoresist were removed by immersion in a 3:1 mixture of DIW and AZ Electronic Materials 400K developer solution for 90 seconds.

An air plasma treatment of the patterned wafer was used to promote adhesion of the CNC film to the photoresist layer. The wafer was treated in a custom plasma chamber at 0.5 torr and 100 W power for 1 minute. This treatment significantly hydrophilized the surface to allow a more uniform coating from aqueous dispersion. CNC films were deposited using either dip coating or doctor blade coating. The films were stabilized for MEMS processing by vacuum heat treatment at 60^{o}C overnight. The CNC film was etched using a Matrix Oxygen Plasma Asher at a pressure of 5 torr and 300 W RF forward.

3.5.2 2nd Generation MEMS

In collaboration with Partha Saha variations were made to the CNC MEMS fabrication procedure to improve the devices. An image reversal positive photoresist AZ5214E was spin coated on HMDS coated silicon substrate (100). Silicon was chosen for convenience, but other substrates may be used. Hot plate drying at 110^{o}C for 1 min was applied to achieve a photoresist thickness of 2 μm, using a ramp of 500 rpms^{-1} and rpm of

1500. Next, using the anchoring mask, the thin layer was UV exposed and developed with a potassium based developer AZ400K (1 part developer to 3 parts water). The exposed photoresist part was washed off with DI water followed by air drying. In the following step, a wafer with an anchor pattern of photoresist was treated with air plasma at 0.05 torr and 100 watt for 1 min. After plasma treatment, the water contact angle of the patterned surface decreased from 53^{o} to 17^{o}. Afterwards, the CNC dispersion was sheared and dried onto the photoresist layer. Next, a 10 nm thin layer of Ti/ TiO_2 was e-beam deposited on the CNC film. This was followed by spin coating of second photoresist layer, AZP4620. In a convection oven, the wafer was heated at 50 - 60 ^{o}C for 10 minutes to cross-link the second photoresist layer to the Ti/TiO_2. After sufficient cooling, the dried photoresist was UV exposed in a similar fashion as before, except a device mask was used to create the device pattern. After developing, some parts of the Ti/TiO_2 coated CNC film were covered under the second photoresist layer with the actual structural profile of the MEMS devices. The uncovered area of the Ti/TiO_2 coated CNC film was then plasma etched to shape out the device profiles of the CNC MEMS. The 10 nm Ti/TiO_2 film was etched out first, applying inductively coupled plasma using CF_4. Along with induction coil power, a platen bias voltage was applied to make the etching anisotropic from top to bottom. Afterwards, the Ti/TiO_2 free CNC film was plasma etched using O_2. Etching quality was confirmed by cross-polarized reflected microscopy. Diced pieces of wafer with devices were submerged into stagnant isopropyl alcohol and acetone was used to wash off the residual photoresist layers. Released devices were rinsed using 99% IPA solution, submerge in the IPA, and transferred to a critical point dryer. They were dried using supercritical CO_2 at 1400 psi and 32^{o}C. The final devices were stored in a desiccation chamber.

Chapter 4 Nematic Films for MEMS Applications

This chapter summarizes the results from collaborative research between the Davis and Ashurst Groups at Auburn University and the Kitchens Group at Clemson University. The overall objective of this work was to prepare CNC films with controlled morphologies, such that their mechanical properties were suitable for the production of microelectromechanical systems (MEMS). CNC offer a number of advantages over traditional silicon MEMS for some applications. These include renewability, biodegradability, an easily tunable surface chemistry, and simple processing schemes, which do not require high temperatures or harsh chemicals. Additionally, anisotropic mechanical and optical properties can result from CNC alignment, which is not possible with silicon.

A bottom-up approach was used to fabricate CNC MEMS, starting with dispersions of CNC with three different surface chemistries (CNC-SA, CNC-AA, and CNC-HCl). The dispersion properties of each type of CNC were investigated, and CNC-SA was determined to be the most promising for fabrication into MEMS test devices. An extensive rheo-optical study was performed that investigated the combined effects of initial dispersion microstructure, flow behavior, and relaxation during drying on the final microstructure of CNC-SA films. Finally, MEMS test structures were designed and a fabrication method was devised and optimized using commonplace microfabrication techniques such as photolithography and etching. The elastic modulus, residual stress, and fracture strength for the CNC MEMS were measured with these devices.

4.1 CNC-HCl

As received from our collaborators at Clemson University the CNC-HCl dispersion was 0.88% vol %. This dispersion was significantly more opaque than CNC-SA dispersions of similar concentration, but it appeared to be stable over a period of weeks. The dispersion was concentrated by slow evaporation and samples were taken at 1.24, 1.57, 2.37, 2.73, and 3.06 vol %. Although a rheological study of CNC-HCl was not performed, the viscosity appeared to increase rapidly as the concentration was increased. Araki et. al. also saw a rapid increase in viscosity with concentration for CNC-HCl.[55] At 3.06 vol %, the dispersion did not flow without the application of shear.

The CNC-HCl dispersions were observed using cross-polarized optical microscopy. A number of bright spots were observed in CNC-HCl dispersions over the entire range of concentrations studied. These spots were typically rectangular with some irregularity in shape and were more prevalent in higher concentration dispersion. When rotated under crossed polarizers the spots transitioned from light to dark indicating nanocrystal alignment within these regions. When viewed without crossed polarizers it was determined that the bright regions in the images were caused by large aggregates of CNC-HCl in the dispersions and not by liquid crystalline domains. Alignment within the aggregates is due to CNC's tendency to aggregate laterally rather than randomly.[81] These aggregates are largest in concentrated dispersions and have been observed at over 50 μm in length. Figure 4.1 shows images of a large aggregate at high magnification viewed with and without crossed polarizers.

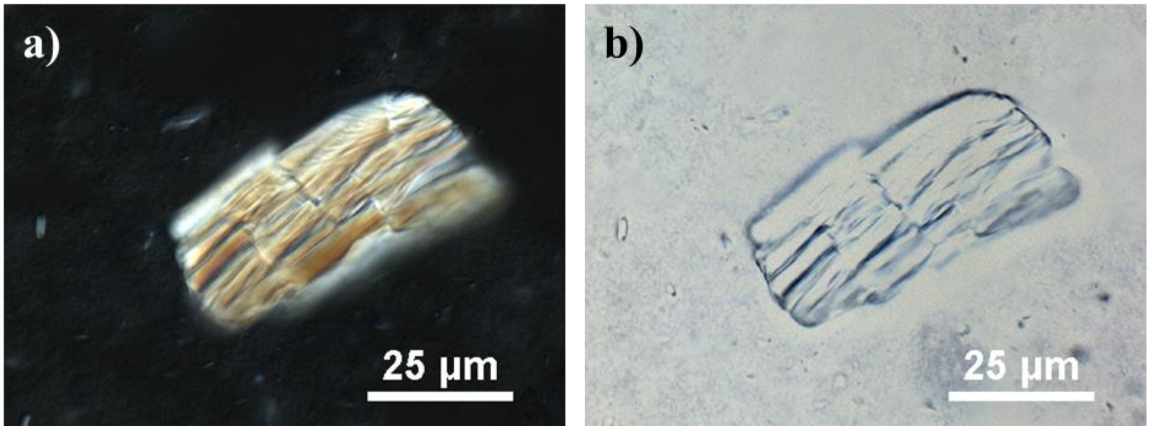

Figure 4.1 Large birefringent aggregate found in a 3.06 vol % CNC-HCl dispersion viewed by optical microscopy a) with and b) without crossed polarizers.

Figure 4.2 shows microscope images of both dilute and concentrated CNC-HCl dispersions. At concentrations of 1.57 vol % and below, no birefringence was observed outside of the large aggregates when the sample was rotated between crossed polarizers. At higher concentrations, while the majority of the dispersion appeared isotropic, birefringent areas could be found in the samples. The birefringent areas of the dispersion displayed a polydomain structure where different regions went light and dark as the sample was rotated. The birefringent regions did not exhibit any of the common textures typically seen in liquid crystalline dispersions. As seen in Figure 4.2f, when a spaces is not used between the slide and the coverslip during sample preparation, the dispersion separates into regions of flocculated CNC in coexistence with regions of almost entirely pure water. This is likely due to the smaller gap. In samples where a spacer is used the flocculated regions are likely piled on top of each other, resulting in a more uniform image. The origin of the birefringent regions at higher concentrations is unknown, however, it could be caused by lateral alignment in flocculated CNC-HCl.

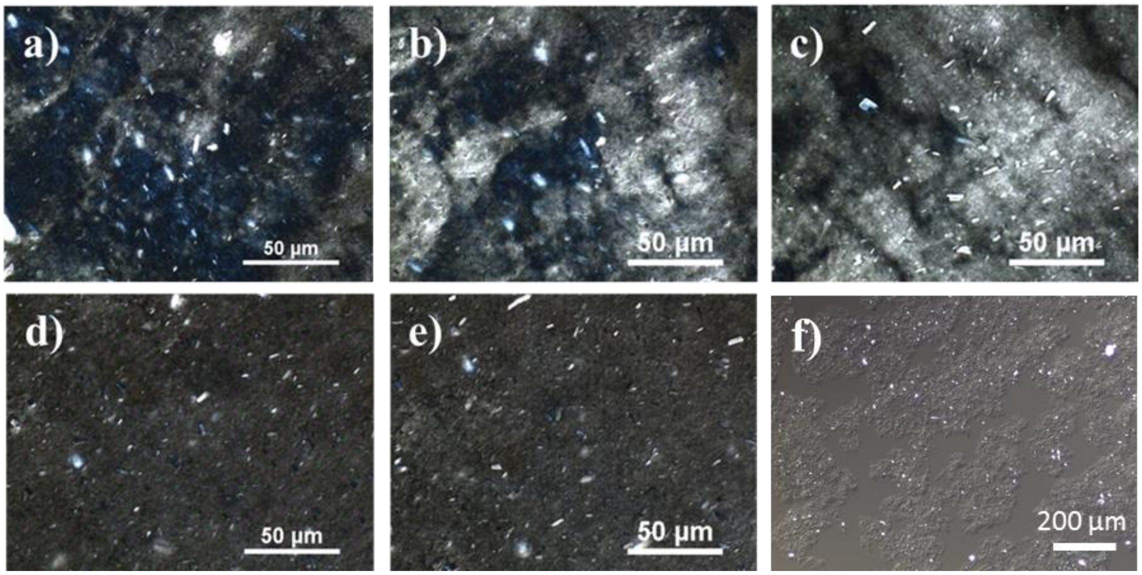

Figure 4.2 Cross-polarized optical microscope images of CNC-HCl dispersions, where a), b), and c) are 3.06 vol % rotated at 0°, 45°, and 90°, respectively and d) and e) are 1.57 vol. % rotated at 0° and 45° respectively. In images a) – e) a 120 µm spacer was used between the slide and the coverslip. In f) a 1.07 vol % dispersion is shown using crossed polarizers and differential interference contrast, without a spacer between the slide and the coverslip.

CNC-HCl films prepared by drop casting and doctor blade coating are shown in Figure 4.3. The drop cast films exhibited birefringence throughout, while only the large aggregates were observed to be birefringent in the doctor blade films. The MEMS fabrication process was attempted with CNC-HCl films, however as can be seen in Figure 4.3c, the large aggregates disrupted the spin coating of photoresist and resulted in cracks in the photoresist layer. Due to this, the use of CNC-HCl was not further pursued in this work.

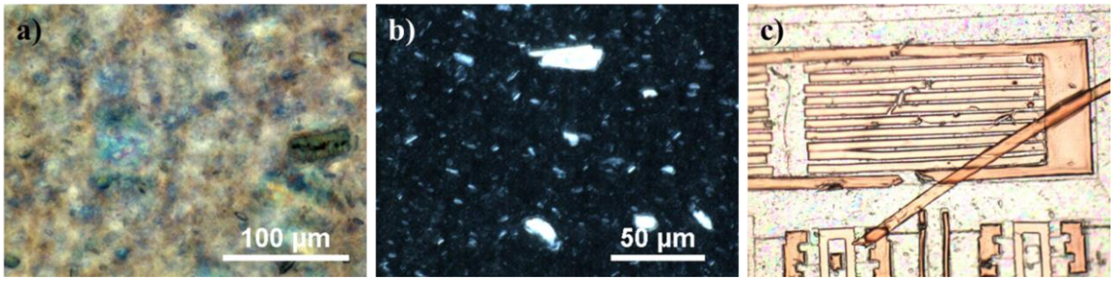

Figure 4.3 Optical microscopy images of CNC-HCl films: a) is a drop cast film from a1.57 vol % dispersion, b) is a doctor blade coated film from a 3.06 vol % dispersion, and c) shows cracking in the photoresist layer caused by large aggregates during the MEMS fabrication process.

4.2 CNC-AA

The CNC-AA dispersion received from our collaborators at Clemson University was 0.67 vol %. As with CNC-HCl, it was a milky white opaque dispersion that was apparently stable for a period of weeks. The dispersion was diluted by the addition of deionized water or concentrated by slow evaporation to achieve concentrations of 0.48, 0.84, 1.51, and 3.46 vol %. As with the CNC-HCl, a rheological study was not performed, but the viscosity appeared to increase rapidly with increasing concentration.

The CNC-AA dispersions were observed using cross-polarized optical microscopy. Unlike the CNC-HCl dispersions, large aggregates were not seen. Otherwise, the CNC-AA dispersions behaved similar to the CNC-HCl dispersions. Figure 4.4 shows cross-polarized microscope images of 1.51 and 3.46 vol % CNC-AA dispersions. Birefringence is seen in both samples with areas transitioning from light to dark as the sample is rotated between the polarizers. Again, when a sample was prepared without a spacer between the slide and coverslip, the dispersion separated into regions of flocculated CNC-AA and regions that are mostly solvent.

AFM was also used to investigate the dispersion state of CNC-AA in water. A droplet of 0.05 vol % CNC-AA was placed on a freshly cleaved mica surface. The dispersion was allowed to sit for 5 minutes for the CNC to adsorb onto the surface, and then the sample was blown dry. For comparison, the same procedure was followed for a CNC-SA dispersion, which is well known to disperse easily as individuals. The AFM images of both samples are shown in Figure 4.5. While to CNC-SA adsorbed as individuals onto the mica surface, the CNC-AA appear largely as bundles. In the CNC-AA bundles, the individual rods are associated in a lateral fashion. This side-to-side association has been

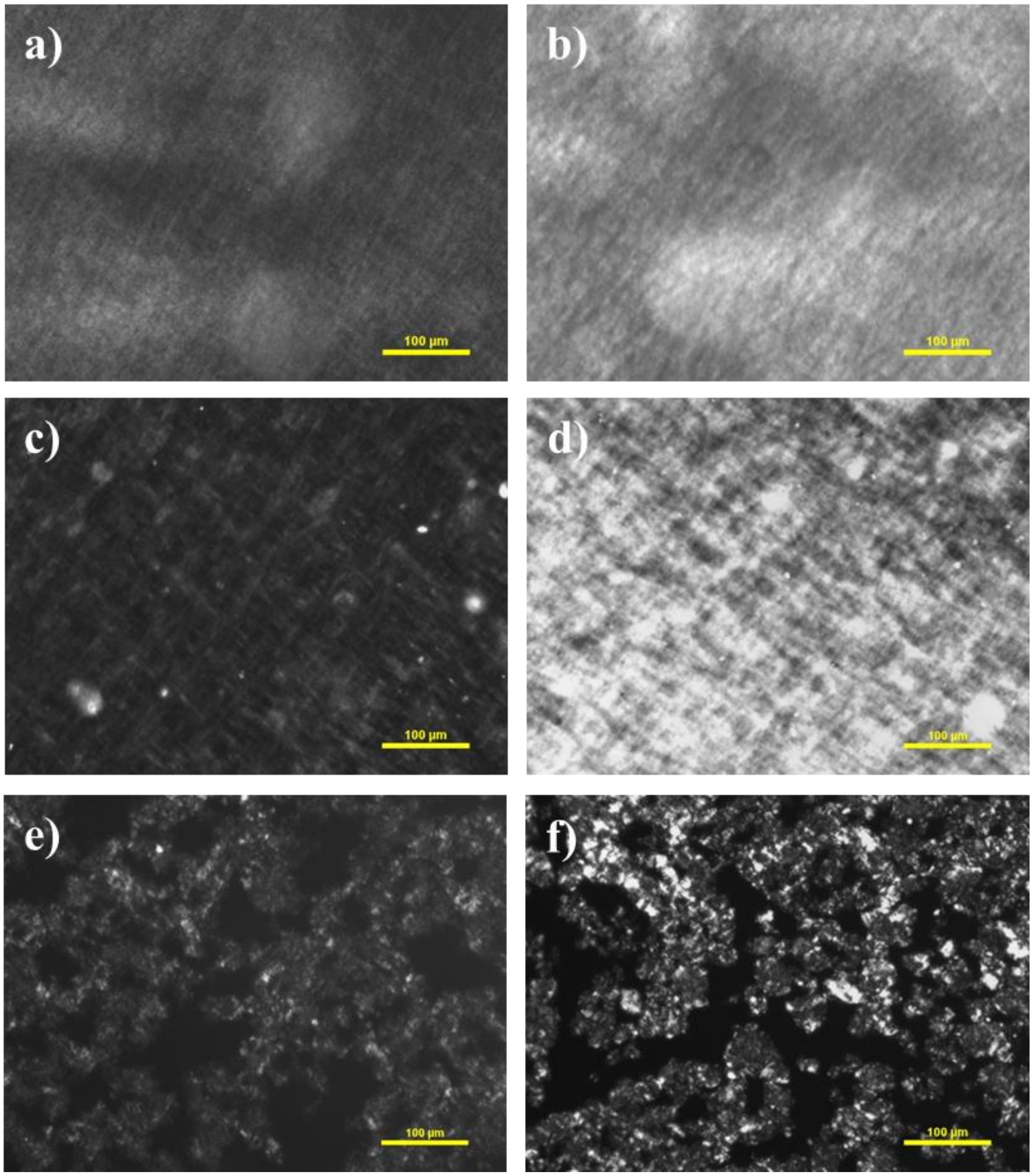

Figure 4.4 Cross-polarized optical microscopy images of CNC-HAA dispersions, where a) and b) are 1.51 vol % rotated at 0^o and 45^o, respectively and c) and d) are 3.46 vol. % rotated at 0^o and 45^o respectively. In images a) – d) a 120 μm spacer was used between the slide and the coverslip. In e) and f) the 1.51 vol % and 3.46 vol % dispersions shown, respectively, without a spacer between the slide and the coverslip.

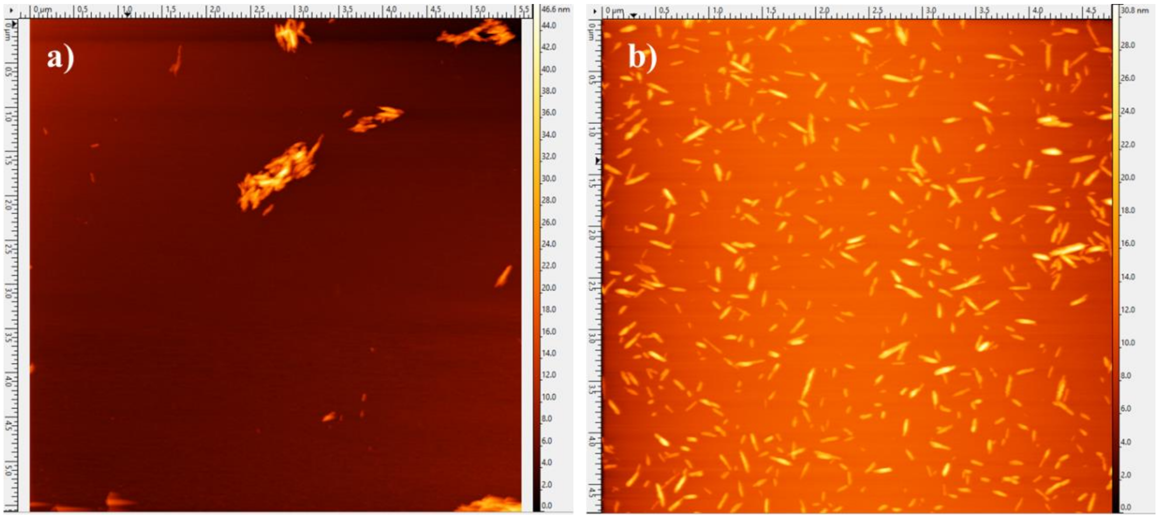

Figure 4.5 AFM images of a) CNC-AA, and b) CNC-SA adsorbed onto a mica surface.

seen previously for CNC.[81] The lateral flocculation of the CNC is the likely cause of birefringence in the cross-polarized optical images.

In order to further investigate the dispersion state, the 0.93 vol % CNC-AA dispersion was fluorescently labeled with 5-(4, 6-dichlorotriazinyl) aminofluorescein (DTAF) using established methods.[79] The labeled CNC-AA were diluted to 0.06 vol % and both dispersions were imaged with confocal microscopy. Figure 4.6 shows a 3D representation of z-stacked confocal microscope images of the 0.06 vol % CNC-AA dispersion. In this image, the dispersion appears to consist of regions of loosely associated CNC-AA and regions that contain almost pure solvent. This is consistent with what was seen in the optical microscopy images of samples prepared with no spacer. At 0.93 vol %, as shown in Figure 4.7, the loosely associated CNC-AA occupy a larger percentage of the volume. However, there are still some regions that are mostly solvent, with little CNC-AA. In this image, there are also some small areas with high fluorescence intensity. These are likely strongly associated aggregates of CNC-AA.

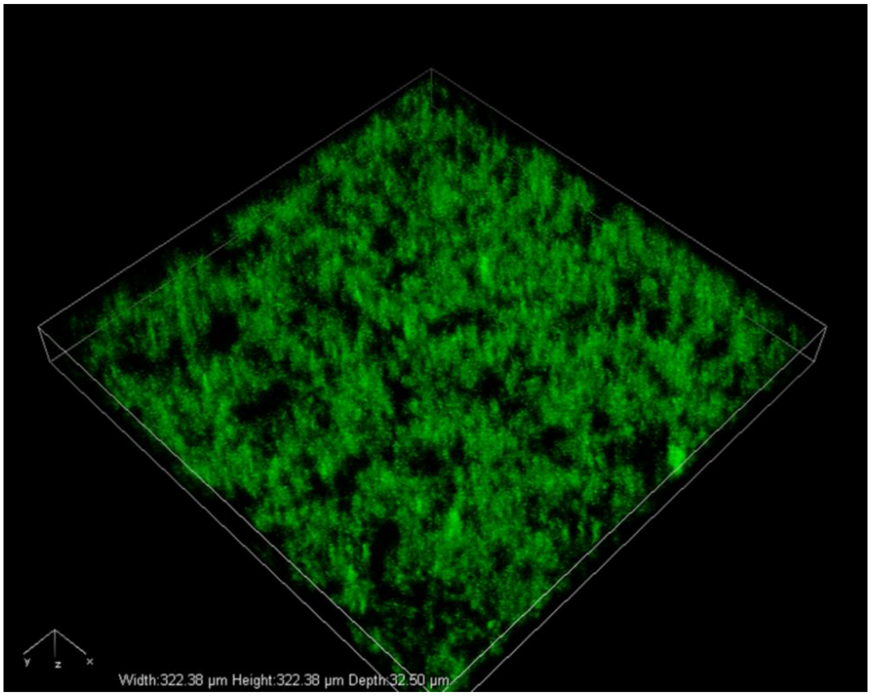

Figure 4.6 3D representation of confocal microscope z-stacked images of a 0.06 vol % CNC-AA dispersion.

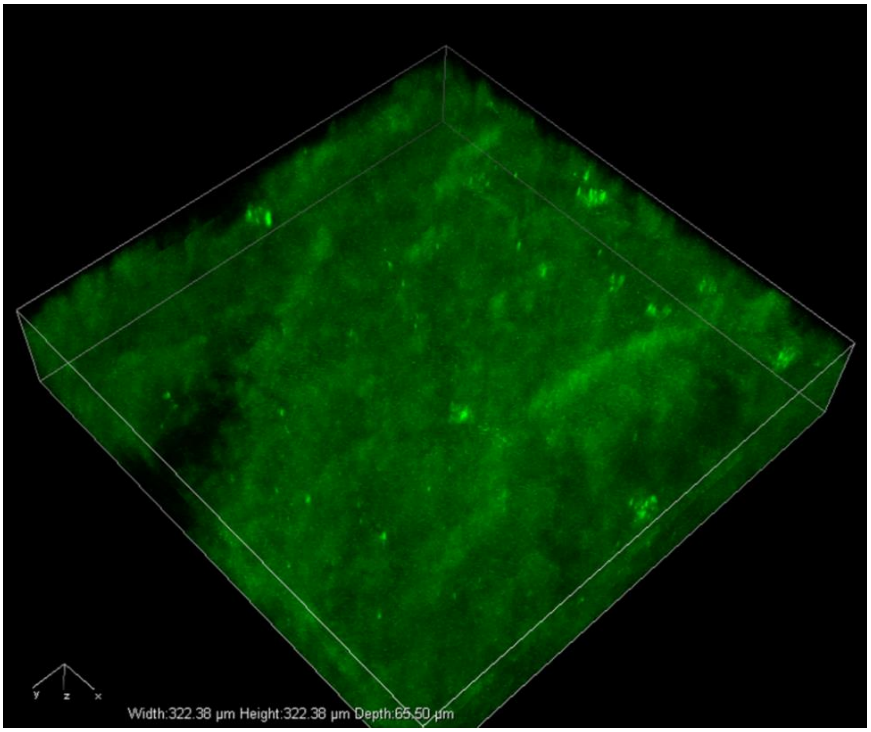

Figure 4.7 3D representation of confocal microscope z-stacked images of a 0.93 vol % CNC-AA dispersion.

Finally, cryogenic scanning electron microscopy (cryo-SEM) was used in hopes of better observing the dispersion state of individual CNC-AA. This work was done at the CIF Microscopy Lab at Tulane University. However, the freezing rate was not sufficient to avoid microstructural changes resulting from the water freezing front. In a process known as ice-segregation-induced self-assembly (ISISA), the CNC were organized by rejection from the growing ice crystals. This resulted in a ribbon like morphology, which is shown in Figure 4.8. Generally, the structure of the frozen CNC was dependent on dispersion concentration, and as concentration was increased the ribbons become larger and bridges are formed which connect the ribbons. However, other structures, such as a layer-like structure and a network structure were observed (Figure 4.9). These structures can be preserved as aerogels by lyophilization. While cryo-SEM did not allow for imaging of dispersion microstructure, it sparked an interest in a new research area of CNC aerogels. Future work on CNC aerogels should focus on how the CNC concentration, dispersion microstructure, freezing rate, lyophilization conditions effect the structure of the final product.

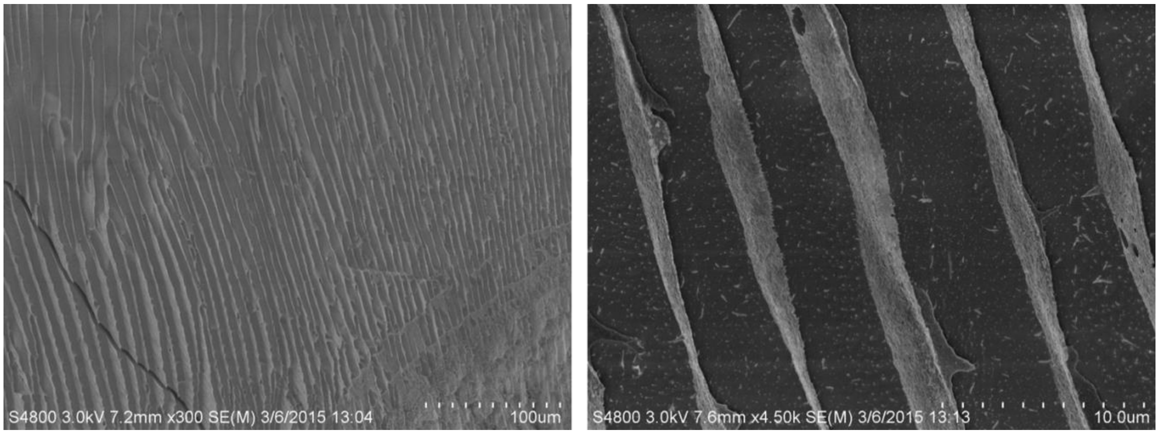

Figure 4.8 Cryo-SEM images of 1.84 vol % CNC-AA dispersion showing the ribbon like morphology resulting from ISISA

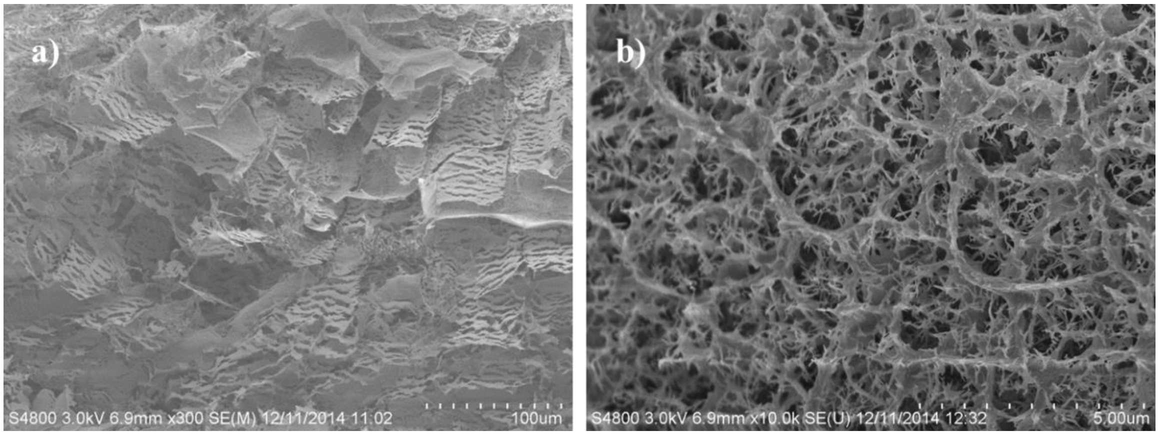

Figure 4.9 Cryo-SEM image of a) 0.77 vol % CNC-AA dispersion showing a layer like structure, and b) 1.54 vol % CNC-AA dispersion showing a network like structure.

4.3 CNC-SA

The rheology and phase behavior of CNC-SA was investigated in a previous study conducted by the Davis Group at Auburn University and the Kitchens Group at Clemson University.[19] Due to their easy dispersability at high concentration and liquid crystalline phase behavior, CNC-SA were chosen as the ideal candidate for films for CNC MEMS. An extensive rheo-optical study was performed that investigated the combined effects of initial dispersion microstructure, flow behavior, and relaxation during drying on the final microstructure of CNC-SA films.

4.3.1 CNC Characterization

For this work, CNC were prepared from cotton cellulose by sulfuric acid hydrolysis as described previously in Section 3.1.1. Based on AFM, the size average CNC length was 112 nm with a standard deviation (σ) of 39 nm, the average width was 27 nm ($\sigma = 7.3$ nm), and the average height was 5.5 nm ($\sigma = 2.3$ nm). The CNC dispersions were acidic due to the presence of -SO_3H introduced to the surface during hydrolysis. The pH of a 1.59 vol %

dispersion was 2.32. Conductiometric titration with 10 mM sodium hydroxide showed there were 208 mmol of $–SO_3H$ per kg of CNC.

4.3.2 Rheology

The ability of CNC to form aligned films is highly dependent on the initial dispersion microstructure. The rheology and liquid crystalline phase behavior of cotton CNC has previously been investigated by several researchers.[19, 61, 82] For example, Ureña-Benavides et. al. determined that the isotropic to biphasic, biphasic to liquid crystalline, and liquid crystalline to gel transitions occur at 3.07, 11.2, and 14.5 vol %, respectively. However, it is well established that batch to batch variations in aspect ratio, polydispersity, ionic strength, and surface charge can alter the phase transitions and rheological properties. Therefore, rheological characterization was performed on the dispersions used in this investigation. The resulting viscosity versus shear rate data is shown in Figure 4.10.

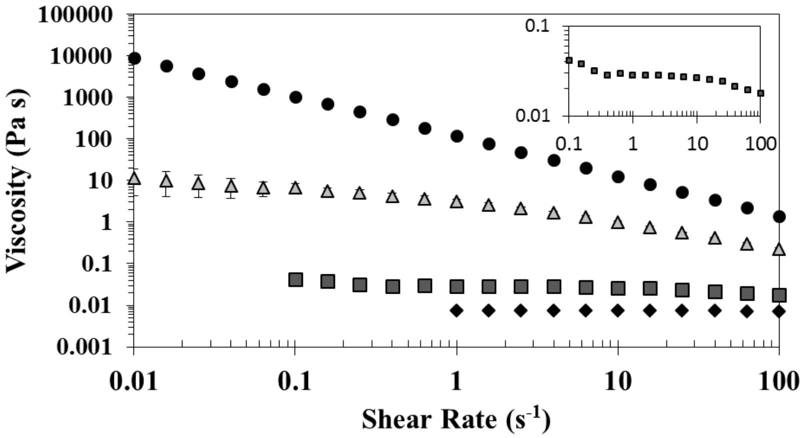

Figure 4.10 Steady shear viscosity of aqueous CNC dispersions as a function of shear rate. Diamonds are the 3.27 vol % dispersion, squares are 6.98 vol %, triangles are 11.6 vol % and circles are 15.8 vol %. Error bars are smaller than symbol size for most data. Inset highlights three region behavior of the 6.98 vol % dispersion.

At 3.27 vol % the behavior was nearly Newtonian. For the 6.98 vol % dispersion, shear thinning was initially observed for shear rates below 0.4 s^{-1}, followed by a plateau between 0.4 s^{-1} and 10 s^{-1}, and again shear thinning above 10 s^{-1}. This type of three region behavior is typically associated with lyotropic liquid crystalline dispersions.[45] The origin of the initial region I shear thinning region is typically associated with director tumbling or variations in the polydomain defect texture of the liquid crystal with flow.[83] The region II plateau at intermediate shear rates has been attributed to director wagging, or vorticity alignment. The final, region III, shear thinning region is caused by rod alignment in the flow direction.[19, 42, 47] For the 11.6 and 15.8 vol % dispersion, shear thinning was observed at all shear rates.

Viscoelastic property measurements showed that the 3.27 vol % and 6.98 vol % dispersions behaved as purely viscous fluids while the 11.6 vol % dispersion was predominantly viscous (*G”* > *G’*), with a strong dependence of *G’* on frequency. The 15.8 vol % dispersion was a rheological gel, *G’* was greater than *G”* at all frequencies (tan $\delta < 1$) and *G’* was independent of frequency. Oscillatory rheology data for the 11.6 and 15.8 vol % dispersions are shown in Figure 4.11.

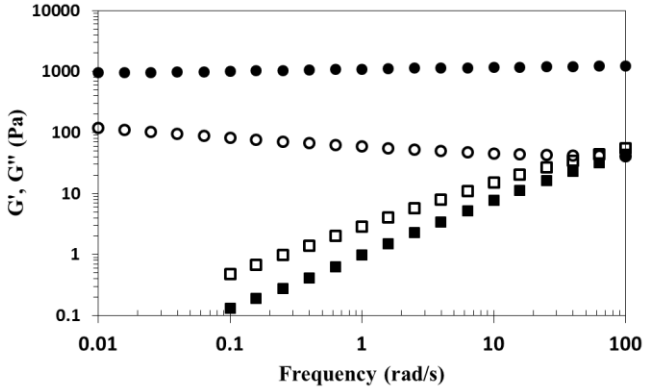

Figure 4.11 The storage modulus G’ and loss modulus G” of CNC dispersions at 11.6 and 15.8 vol %. Open symbols are G” and closed symbols are G’. Squares are for the 11.6 vol% dispersion and circles are for the 15.8 vol % dispersion.

4.3.3 Optical Microscopy

4.3.3.1 Initial Dispersion Microstructure

Polarized optical microscopy of the dispersions as a function of concentration and shear rate are shown in Figure 4.12; rows are in order of increasing concentration and the columns are in order of increasing shear rate. The 3.27 vol. % dispersion is not shown, it was completely isotropic. At 0 s^{-1}, the 6.98 vol. % sample is biphasic with “bullseye” liquid crystalline domains interspersed in an isotropic phase. At the phase boundary for a spherical droplet, the surface energy is minimized when the director is tangential to the phase boundary, resulting in the cholesteric structure forming a concentric system of spheres.[84] In Figure 4.12f, at 11.6 vol % the sample is completely birefringent and exhibits the fingerprint pattern that is typical of a cholesteric liquid crystal. An enlarged version of Figure 4.12f which clearly shows the fingerprint texture is shown in Figure 4.13. It should be noted that the helix alignment is not uniform throughout the sample; there is local helix alignment within the domains, but the dispersion is globally isotropic. When the concentration is increased to 15.8 vol % (Figure 4.12k), the fingerprint texture is replaced by a more random texture characteristic of transition to a gel phase in agreement with the frequency independence of G’. Cross-polarized images of dispersions that were allowed to settle in sealed cuvettes for several months are shown in Figure 4.14. These images confirm the phase behavior of the dispersions and exemplify the dispersions’ stability.

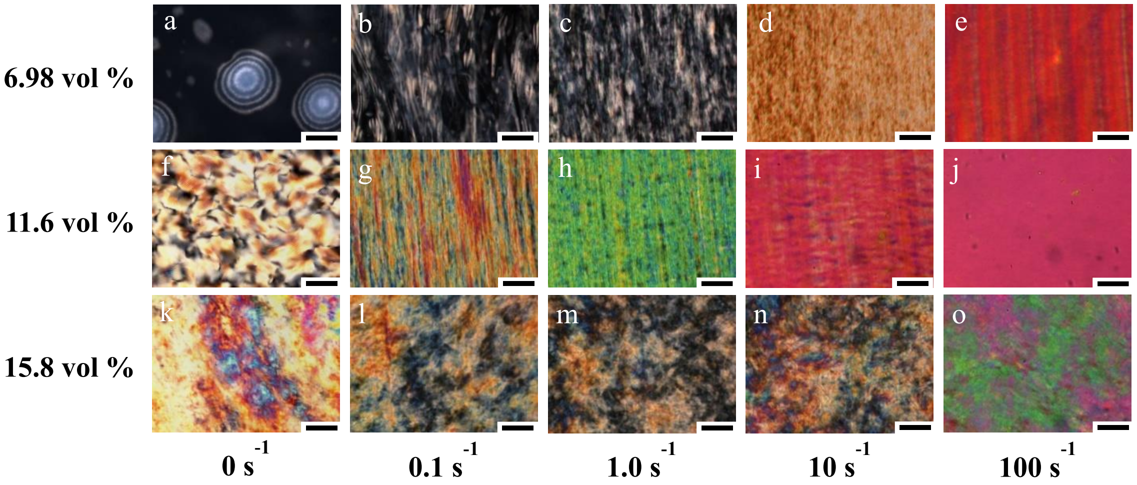

Figure 4.12 Cross-polarized optical microscopy images of CNC dispersions after shear. Dispersion concentrations are indicated for each row and shear rate is indicated for each column. Scale bars are 100 µm.

Figure 4.13 Enlarged region of Figure 4.12f showing the cholesteric fingerprint texture. Scale bar is 100 µm.

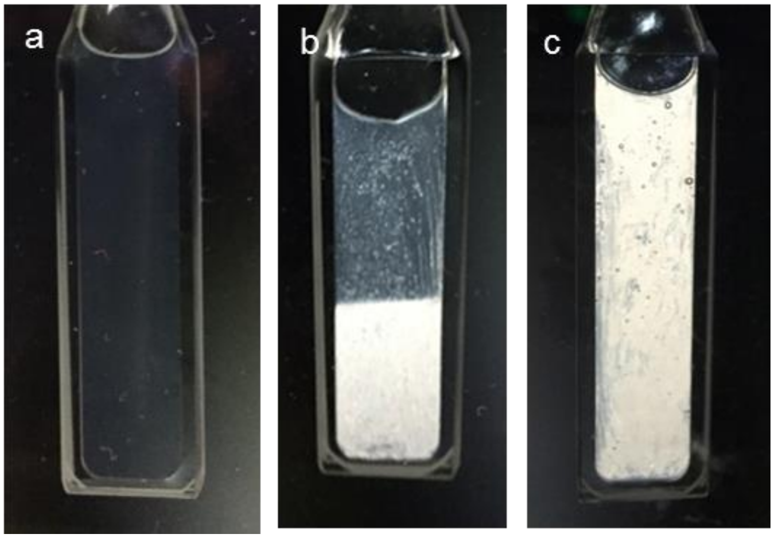

Figure 4.14 Cross-polarized images showing phase behavior of CNC suspensions in cuvettes at a) 3.29, b) 6.98, and c) 11.6 vol. %. The liquid crystalline phase is birefringent, while the isotropic phase appears dark.

4.3.3.2 Rheo-Optics

The first row of Figure 4.12 shows images of the 6.98 vol % biphasic CNC dispersion at shear rates ranging from 0-100 s^{-1}. In Figure 4.12b (0.1 s^{-1}) the discrete domains begin to breakup and elongate in the direction of shear. Remnants of the “bullseye” texture can be observed as a fingerprint texture oriented perpendicular to the flow direction. This indicates that the shear is not strong enough to unwind the cholesteric pitch, but has begun to orient the helical axes of the domains. Rheo-NMR experiments by Geng et. al. also indicated that the cholesteric structure is retained when shearing a lyotropic hydroxypropyl cellulose (HPC) dispersion at low shear rates in the region I tumbling regime.[85] In Figure 4.12c, as the shear rate is further increased into the region II plateau (at 1.0 s^{-1}), the domains begin to merge and the isotropic fraction decreases, indicating that the initially isotropic phase is beginning to be oriented by shear. The absence of the fingerprint texture is indicative of a shear induced unwinding of the cholesteric pitch and transition towards nematic alignment. In Figure 4.12d (10 s^{-1}) the region III shear thinning is beginning and the image is relatively uniform in color and texture. No isotropic domains remain as all the CNC are aligned in the direction of shear. As the shear rate is further increased to 100 s^{-1} (Figure 4.12e), the color shifts from orange to red with the texture becoming smoother.

Aligned nanorod dispersions and films are known to exhibit remarkable anisotropic optical properties, such as birefringence.[86] It is this birefringence that causes the colors seen in cross-polarized optical images as certain wavelengths either constructively or destructively interfere after passing through the sample. The interference color depends on the retardation which is a function of the birefringence and thickness of the sample. The relationship between color, retardation, thickness, and birefringence is illustrated in the Michel-Levy Chart (Figure 4.15).[87] In the chart, each order refers to approximately 550 nm of retardation with various colors in each order resulting from a particular optical retardation. For a nanorod dispersion or film, if the thickness and nanorod alignments are uniform, a uniform interference color will be observed. As the degree of alignment increases, the birefringence increases, and higher order interference colors are seen. Therefore, the shift from orange to red between Figure 4.12d and Figure 4.12e indicates increased order in the system.

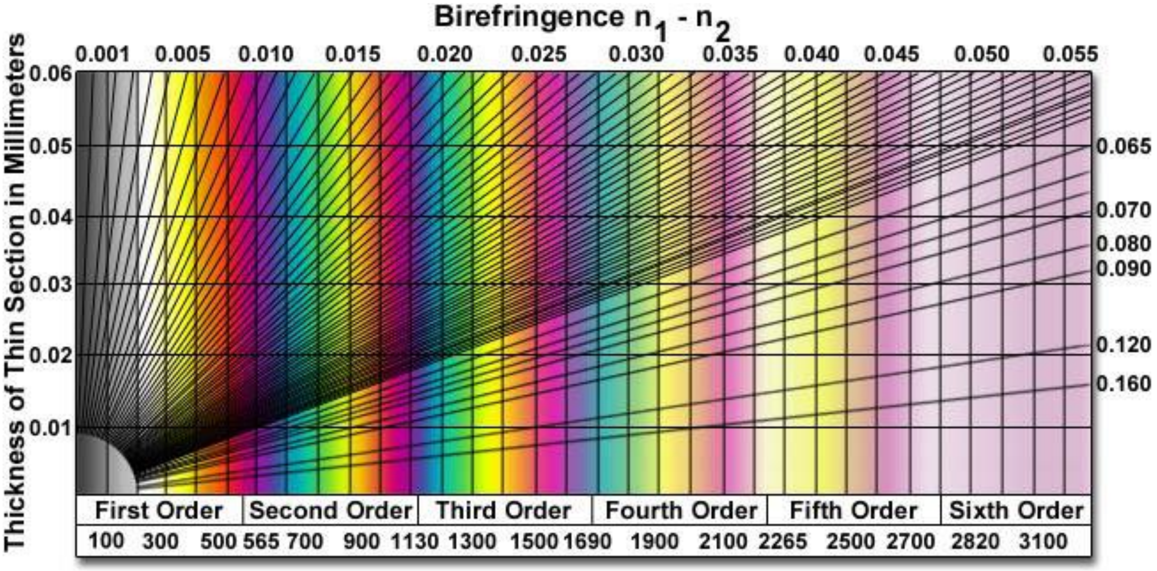

Figure 4.15 Michel-Levy birefringence chart. This chart gives interference colors as a function of sample thickness and birefringence. Sample thickness is on the y-axis and birefringence is indicated by the diagonal lines. The numbers on the x-axis are retardation.

The second row of Figure 4.12 shows images of the 11.6 vol % liquid crystalline dispersion under shear. Figure 4.12g (0.1 s^{-1}) clearly shows the elongation of domains to form ellipsoids oriented in the direction of shear. This behavior was also seen by Onogi et. al. for cholesteric dispersions of hydroxypropyl cellulose and nematic dispersions of poly-paraphenylene terephtalamide (PPTA).[88] Unlike the biphasic dispersion, no fingerprint texture is observed. However, colorful discontinuous stripes are seen, similar to those observed by Ureña-Benavides et. al. for a precholesteric dispersion.[19] As the shear rate is increased, the striped texture becomes less pronounced, giving way to a more uniform color. While a completely uniform interference color is not observed until above 25 s^{-1}, the image at 0.251 s^{-1} is predominantly first order orange. This transitions to a second order blue at 0.398 and 0.631 s^{-1}, a second order green in Figure 4.12h at 1.0 s^{-1}, and a second order orange at 2.51 s^{-1}. At 6.31 s^{-1}, the interference color reaches a second order pink, which becomes increasingly uniform as the shear rate is further increased. Additional images at intermediate shear rates not shown in Figure 4.12 are shown in Figure 4.16. As in the case of the 6.98 vol % dispersion, the thickness of the sample is constant. Therefore, the change in interference color must be attributed to an increase in birefringence of the sample, indicating that as the shear rate is increased the nanocrystals are increasingly aligned in the direction of shear. Little difference is observed in the sample from 25.1 s^{-1} to 100 s^{-1}, due to the nanocrystals reaching their maximum alignment. A plateau in order parameter was reported by Orts et. al. above 100 s^{-1} for CNC from kraft pulp which are larger than those from cotton.[67]

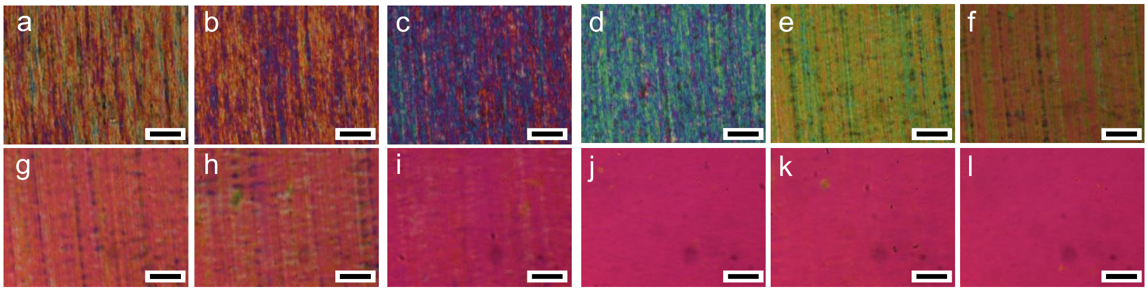

Figure 4.16 Sheared 11.6 vol % dispersions at additional shear rates of a) 0.158, b) 0.251, c) 0.398, d) 0.631, e) 1.58, f) 2.51, g) 3.98, h) 6.31, i) 15.8, j) 25.1, k) 39.8, and l) 63.1 s^{-1}. Scale bar is 100 μm.

The final row of Figure 4.12 shows images for the 15.8 vol % CNC gel. The texture and colors in Figure 4.12m, and n, are remarkably similar, indicating that there is very little change in the microstructure of the gel from 0.1-10 s^{-1}. Similar behavior was reported by Kiss et. al. up to 200 s^{-1} for a poly-β-benzyl-asparate gel.[89] In Figure 4.12, the colors change and the domains become larger. This is caused by a breaking of the gel structure and partial alignment in the direction of shear. However, 100 s^{-1} is not a high enough shear rate to fully break the gel and align the rods into a monodomain nematic structure.

Relaxation after the cessation shear is important for the manufacture of aligned solid films. If the drying time is too long, polydomain textures reappear as the solvent is removed. This is especially problematic for low viscosity isotropic and biphasic dispersions with short relaxation times.[86] For dispersions with higher initial concentration, solvent evaporation can quickly lock the system into a gel state where no further relaxation can occur.[76,90] To study relaxation, time lapse optical microscopy was performed after the cessation of shear at 100 s^{-1}, and the intensity of light transmitted through the crossed polarizers was measured. The light intensity I transmitted by a birefringent material between crossed polarizers can be expressed as in Equation 4.1:

$$I(\theta) = I_0 sin^2(2\theta) sin^2\left(\frac{\pi d \Delta n}{\lambda}\right) \tag{4.1}$$

where I_0 is the intensity when the polarizer and analyzer are parallel, θ is the angle between the polarizer and the optical axis of the material (in this case the orientation of the CNC), Δn is the birefringence, λ is the wavelength of light, and d is the film thickness.[86] Optical contrast (OC) is expressed as $(I_{max}-I_{min})/(I_{max}+I_{min})$, where I_{max} and I_{min} are the maximum and minimum values of I when varying θ. For a perfectly aligned system, the optical contrast would be 1, while it would be 0 for a completely isotropic system. For this case, I_{max} is assumed to always be $I(45^o)$, while I_{min} is always $I(0^o)$, resulting in the possibility of negative values due to random fluctuations in domain orientation.

4.3.3.3 Post Shear Relaxation

Cross-polarized optical microscopy images at $\theta = 45^o$ and 0^o and optical contrast data for the biphasic, liquid crystalline, and gel dispersions during relaxation are shown in Figure 4.17. The initial optical contrasts are 0.80, 0.91, and 0.69 for the biphasic, liquid crystalline, and gel dispersions, respectively. The biphasic dispersion relaxes relatively quickly, and it reaches a globally isotropic state after approximately five minutes. Fluctuations in the optical contrast after this point are due to random variations in the alignment of domains within the viewing area. The liquid crystalline dispersion retains its shear induced alignment for much longer. Ten minutes after the cessation of shear the optical contrast is 0.61 and the dispersion does not become globally isotropic until approximately 17 minutes after shearing. In the gel phase, the dispersion undergoes an initial relaxation in the first minute. It then reforms its gel structure and optical contrast is relatively constant thereafter. This behavior is likely due to the gel-sol transition described by Kim et. al. where shear breaks the gel structure which quickly reforms into an aligned gel after shear.[86] However, it is important to note that since the CNC gel structure is difficult to break the initial optical contrast is only 0.69 at 100 s^{-1}. While the liquid crystalline dispersion relaxes faster, higher optical contrast is possible. Note that the dispersion does not have to dry fully to lock in the alignment. As the solvent evaporates and concentration increases the relaxation will slow and form an aligned gel.

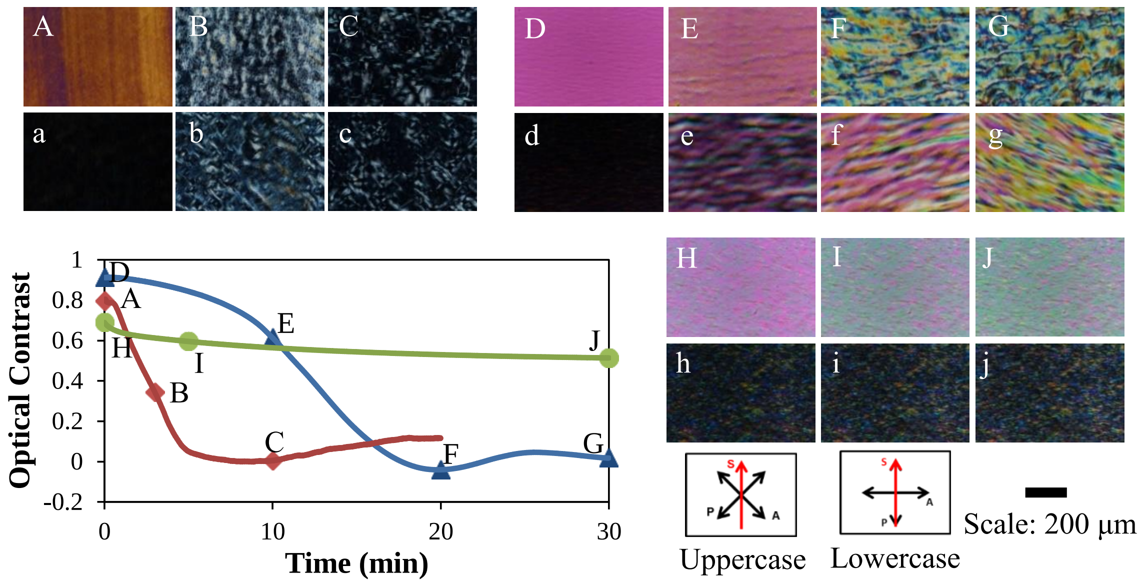

Figure 4.17 Cross-polarized optical microscopy images of CNC suspensions over time during relaxation from 100 s^{-1} shear. Graph shows optical contrast over time. Red=Biphasic, Blue=Liquid Crystalline, Green=Gel. Lines represent one data point per second. Symbols correspond to microscope images.

4.3.4 Film Properties

4.3.4.1 Drop Cast Films

Drop cast films were prepared by allowing 200 µl of each dispersion to dry at ambient conditions on a glass slide. Films cast from the isotropic, biphasic, and liquid crystalline dispersions each show a cholesteric polydomain structure indicated by the fingerprint texture oriented in varying directions (Figure 4.18). The fingerprint texture is less complete in the films cast from the isotropic and biphasic dispersions, as the liquid crystalline domains were not present in the initial dispersion and formed as a result of concentration increasing during drying. The color differences between the films are caused by variation in the thickness of the films. The lower concentration dispersions resulted in thinner films which exhibit less color than the film prepared from the liquid crystalline dispersion. Thickness variations within the film were also observed, with the edges being thicker than the centers. This is commonly observed for drop-cast colloidal and nanoparticle films and is caused by coffee ring formation where capillary forces cause the nanocrystals to flow towards the edge of the droplet.[91] This also results in further non-uniformity in alignment, with the nanocrystals near the edge being aligned tangential to the film edge.

4.3.4.2 Flow-Aligned Films

In Figure 4.19, images of doctor blade coated films from each of the four dispersions are shown with the flow direction oriented at 45^o and 0^o to the polarizer. These films were cast at a shear rate of approximately 100 s^{-1} with a wet thickness of 100 µm. As with the drop cast films, the films made from isotropic and biphasic dispersions have a

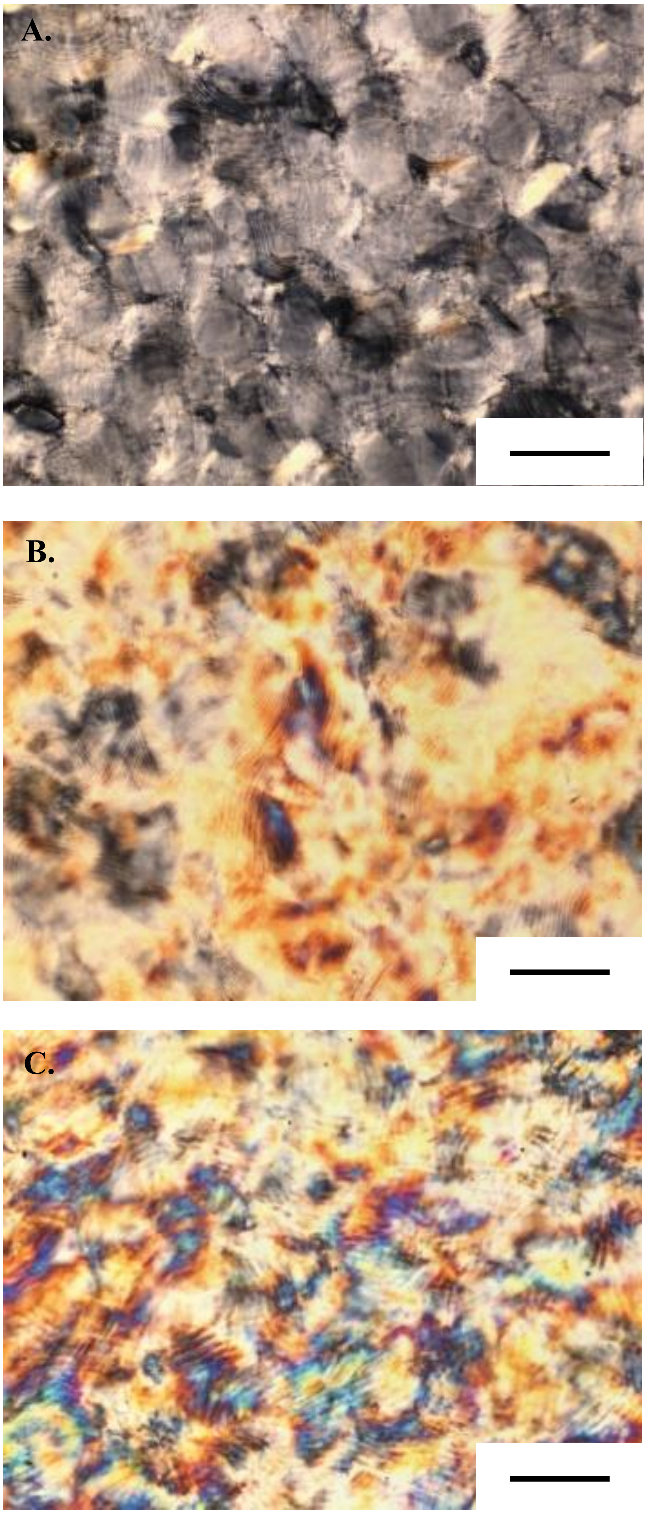

Figure 4.18 Cross-polarized optical microscope images of drop cast films. A) is from a 3.27 vol % dispersion, B) is from a 6.98 vol % dispersion, and C) is from a 11.6 vol % dispersion. Scale bar is 100 µm.

cholesteric fingerprint texture. Interestingly, the film made from the isotropic dispersion, which does not flow align in dispersion, has an optical contrast of 0.23. The beginnings of the fingerprint texture are elongated in the direction of shear, similar to what is seen in the biphasic dispersion during low shear. Although the rods are slightly aligned by flow, relaxation after shear is almost instantaneous while drying is not. Therefore, this alignment is more likely caused by capillary flow and going through the liquid crystalline phase transition during film drying than by any shear induced alignment from the doctor blade coating. Although the biphasic dispersion has an optical contrast of 0.80 when sheared at 100 s^{-1}, the shear induced alignment fully relaxes during film drying resulting in a polydomain film with an optical contrast of 0.01. Conversely, the gel dispersion relaxes slowly during film drying. However, due to the difficulty of initially aligning the gel with shear, the film is still non-uniform with varying interference colors and an optical contrast of 0.50. The film prepared from the liquid crystalline dispersion exhibits an exceedingly high optical contrast of 0.96 and a uniform structure as indicated by the uniform interference color. This suggests that the rods remain highly aligned during film drying and are locked into a gel state early in the drying process. This quick drying is possible due to the low wet thickness of the film. Films with greater wet thicknesses, typically over 250 μm, relax further during the drying process and the polydomain texture reappears. It is noted that the optical contrast of the film is higher than that of the initial dispersion at 100 s^{-1}. Similar results by Kim et. al. were explained to be caused by additional packing during the drying process.[86] It should be noted that at cracking is prevalent in CNC films above a critical cracking thickness, as is common for colloidal films.[92] In our case, cracking is more prevalent for flow-aligned films and the cracks propagate in the direction of shear.

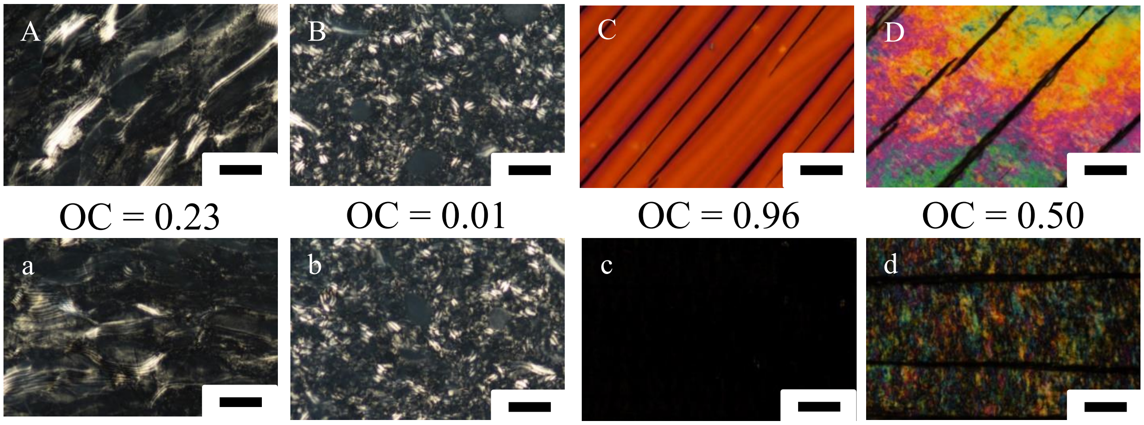

Figure 4.19 Doctor blade coated CNC films made from a) isotropic, b) biphasic, c) liquid crystalline and d) gel dispersions. In images with uppercase letters the flow direction is oriented at 45^{o} with respect to the polarizer while lower case letters indicate alignment with the polarizer. The scale bar is 100 μm.

4.3.4.3 Film Interference Colors

The retardation, and therefore the interference color, of the film can be tuned by changing the film thickness. Figure 4.20 shows images and CRAIC spectra of four CNC films prepared by doctor blade coating from the liquid crystalline dispersion at 100 s^{-1}. At 50 μm wet thickness, the resultant film is in the first order grey region of the Michel-Levy chart and exhibits high transparency throughout the visible region. As the wet thickness is increased to 100, 150 and 200 μm the interference colors step to a first order orange, second order blue, and second order yellow. This results in a narrowing of the transmitted spectral band of the film which could be tuned to any region of the visible spectrum by tighter control of the film thickness.

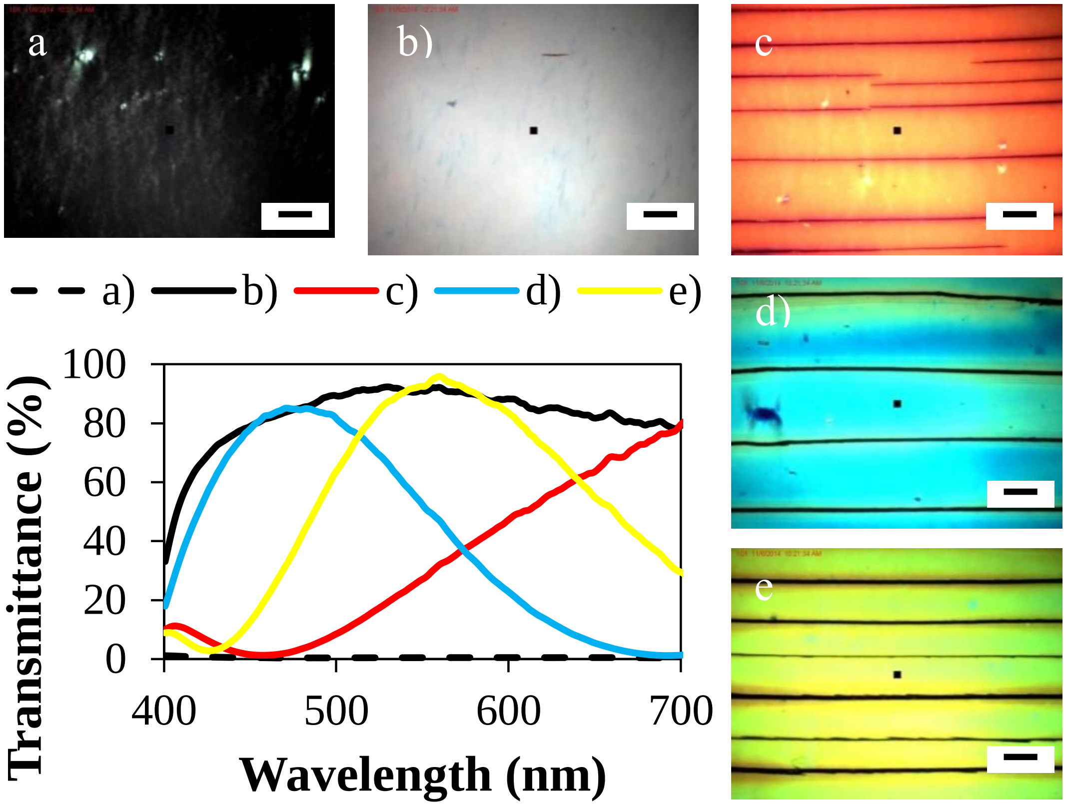

Figure 4.20 CRAIC spectra and images of CNC films prepared from liquid crystalline dispersion at wet thicknesses of a-b) 50 μm, c) 100 μm, d) 150 μm and e) 200 μm. Films a and b are rotated at 0° and 45° to the polarizer, respectively. Scale bars are 50 μm.

4.4 CNC/Polymer Films

As discussed in Section 4.3.4.3, nematically aligned CNC films tend to crack along the direction of alignment. In order to fabricate MEMS crack free films are necessary. The simplest method would be to prepare films below the critical cracking thickness. However, if thicker films are required another method would be necessary. We explored two hypotheses on methods to eliminate crack formation in films. The first was the addition of polyethylene oxide (PEO); PEO is a water soluble polymer frequently used to provide elasticity to nanomaterial assemblies. The effects of varying the molecular weight of PEO was explored. The second method was inspired by Singh et. al., who showed that flocculating a colloidal suspension before film casting can reduce or eliminate the cracking of thicker films.[92] We also explored a combination of flocculation and polymer in the films. This section will discuss results of experiments done in collaboration with undergraduate researcher Joshua Passantino on film cracking and the mechanical properties of these films. All CNC used in thes section were received as a 13 wt % (8.35 vol %) slurry from the US Forest Service's Cellulose Nanomaterials Pilot Plant at the Forest Products Laboratory.

Initially, CNC films were made at a dry thickness of 0.1 mm with a shear rate of 2.6 s^{-1}. At this thickness of film, cracking occurred in the majority of pure CNC films and cracking was also common in films with 13.3 wt% PEO in the dried film. Working with a flocculated dispersion, crack-free films could be consistently made, and tensile testing was performed on these films. This shows that 0.1 mm was above the critical cracking thickness for CNC films; adding PEO did not consistently stop cracks from forming, but flocculation increased the critical cracking thickness.

In order to compare films from a flocculated and non-flocculated dispersions, the thickness of the films were lowered to 0.05 mm and a shear rate of 5.2 s^{-1} was selected. At the new thickness, films from non-flocculated dispersions could be made consistently crack free and were still robust enough for mechanical testing. To see how the films at 0.1 mm thicknesses and 2.6 s^{-1} compared to the thinner films at 5.2 s^{-1}, the tensile strength and Young's modulus in the direction parallel to flow were compared for the films from flocculated dispersions (Figure 4.21). With the exception of the CNC/PEO (100k) film, the mechanical properties were independent of film thickness. Interestingly, the mechanical properties were largely independent of polymer addition for the flocculated flims.

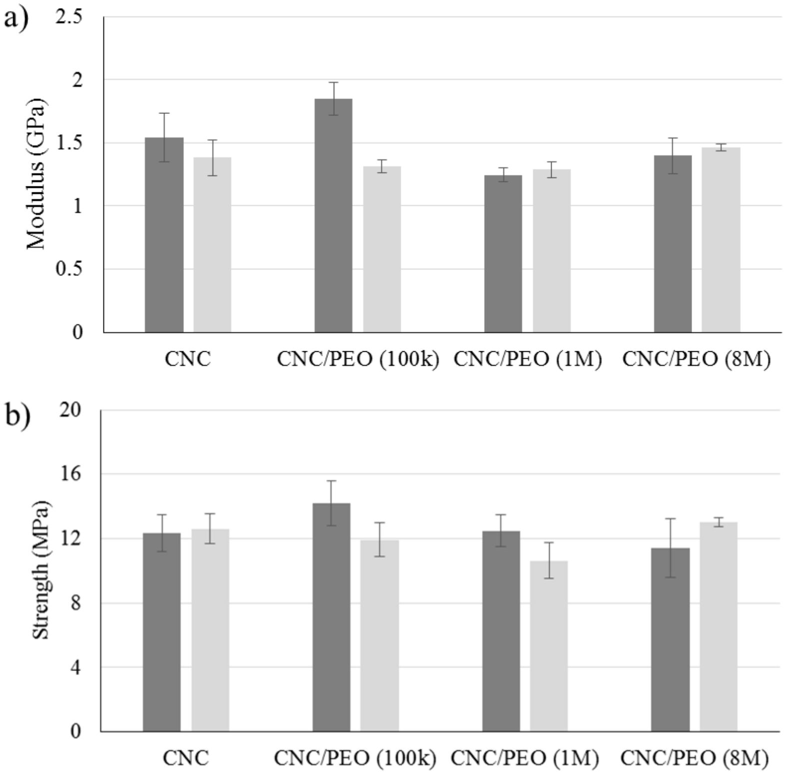

Figure 4.21 Comparison of the mechanical properties of flocculated films with different thicknesses : a) Young's modulus, b) tensile strength. The values in parenthesis are the molecular weights of the PEO. All films with PEO are 13.3 wt% PEO and 86.7 wt% CNC. Dark gray is 0.1 mm thickness and light gray is 0.05 mm thickness. The error bars shown are the standard error from each set of fims.

For the remainder of this work films were prepared with thicknesses of 0.05 mm. Figure 4.22 shows representative cross polarized optical microscopy images for films from each formulation. The images shown are of the center of the film; however, images were taken at multiple positions across the films to verify that the optical texture is uniform across the area. Optical contrast was used to indicate the degree of anisotropy in the films and is indicated in Figure 4.22.

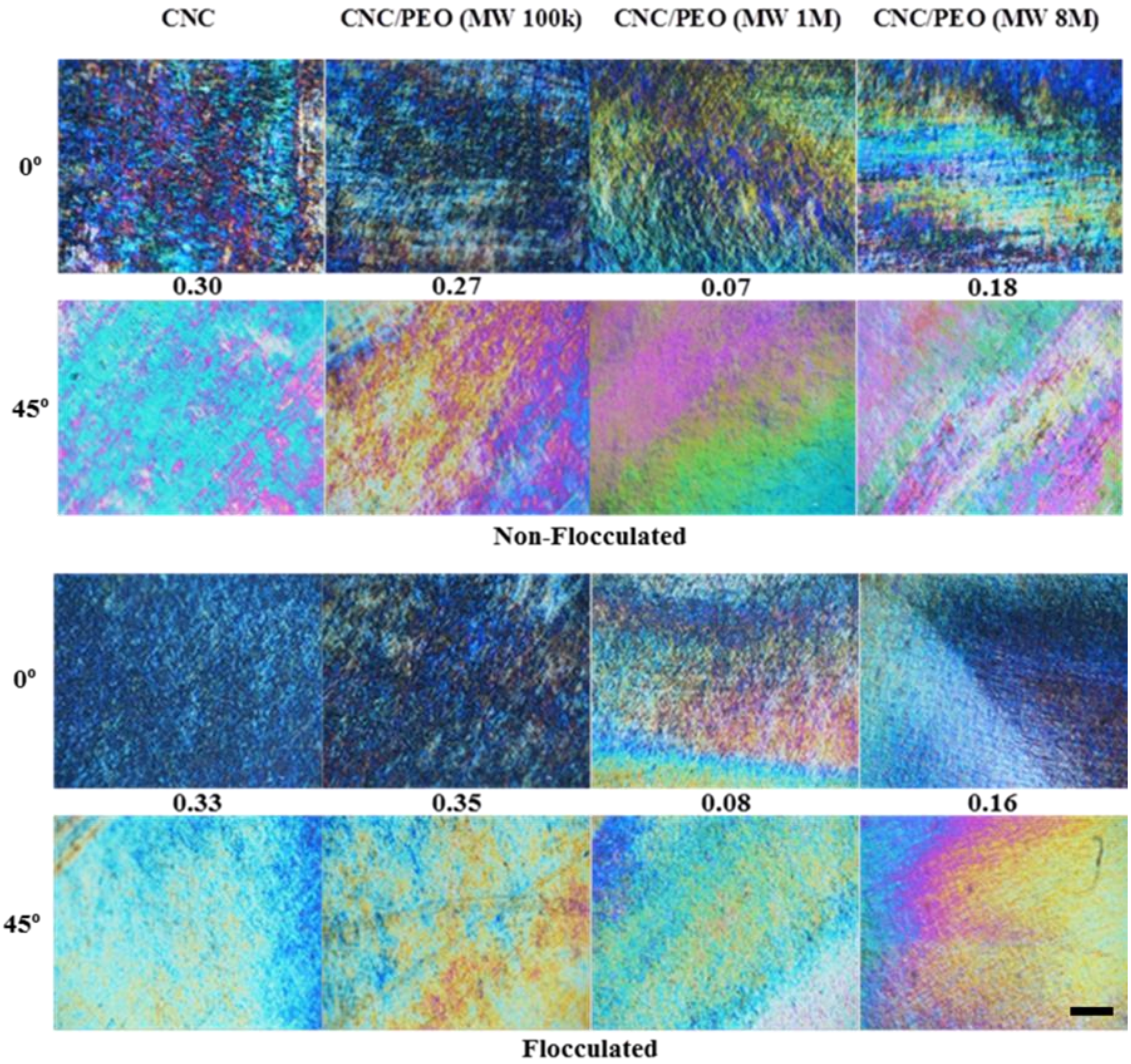

Figure 4.22 Representative cross-polarized microscopy images of all films in the CNC/PEO film study. The film formulation is indicated at the top of each column. The angle of the flow direction to the polarization axis is indicated at the left of each row. Flow direction is to the east in all 0^{o} images and northeast in all 45^{o} images. The top two rows are non-flocculated films and the bottom two rows are flocculated films. The numbers between each pair of films is the optical contrast. The scale bar is 100 µm.

Mechanical properties including Young’s modulus, tensile strength, and toughness for all of the CNC film formulations are shown in Figure 4.23. The pure non-flocculated CNC films had a Young’s modulus of 2.2 GPa parallel to the flow direction, this is 14 times smaller than what Reising et. al. measured in a previous study on aligned CNC films.[73] Perpendicular to the flow direction, our pure non-flocculated films had a Young’s modulus of 1.2 GPa, resulting in an anisotropy ratio of 1.8. The anisotropy ratio is the ratio of the parallel mechanical property to the perpendicular mechanical property. Reising's films had an anisotropy ratio of 4.4 for the Young's modulus, however, his films were prepared using a shear rate of 100 s^{-1} and a liquid crystalline dispersion, likely resulting in greater alignment and higher anisotropy. Values for tensile strength and toughness in our pure CNC films were closer to those measured by Reising. The average tensile strength was 31.5 MPa (parallel) and 12.3 MPa (perpendicular), only about three times lower than Reising's films. The average toughness values were 326 kJ/m^3 (parallel) and 76 kJ/m^3 (perpendicular), which was approximately double that of Reising. As with the Young's modulus the tensile strength and toughness showed mechanical anisotropy with anisotropy ratios of 2.6 and 4.3, respectively.

For the non-flocculated films, the addition of PEO resulted in a decrease in all mechanical properties relative to the pure CNC films. This effect was also seen by Bardet et. al. and is due to the plasticizing effect of the PEO.[93] Interestingly, while increasing the PEO MW resulted in decreased optical anisotropy it resulted in an increase in mechanical anisotropy. The Young's modulus of the non-flocculated films had anisotropy ratios of 1.8, 3.2, 4.2, and 6.0 for the pure CNC, CNC/PEO (100k), CNC/PEO (1M), and CNC/PEO (8M) films, respectively. The addition of 100k MW PEO resulted in films with no anisotropy of tensile strength. However, as the PEO MW is increased the films regain the tensile strength anisotropy that was seen in the pure CNC films, with anisotropy ratios of 2.2 and 3.1 for the CNC/PEO (1M) and CNC/PEO (8M) films, respectively. For the CNC/PEO (100k) films the toughness was higher perpendicular to flow, with an anisotropy ratio of 0.29. With higher MW there was no anisotropy in toughness of the films.

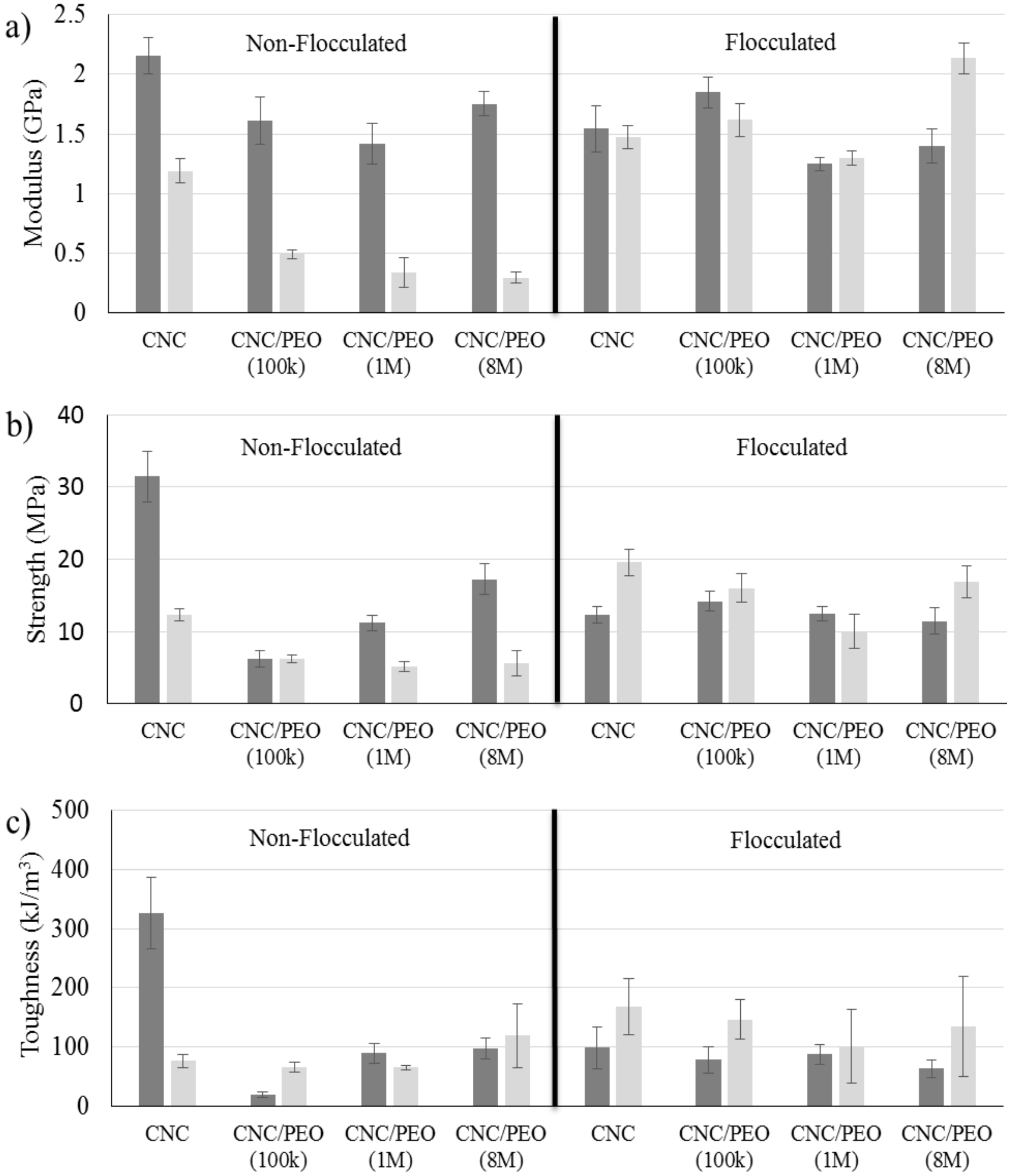

Figure 4.23 Mechanical properties of CNC/PEO Films: a) Young's modulus, b) tensile strength, and c) toughness. The values in parenthesis are the molecular weights of the PEO. All films with PEO are 13.3 wt % PEO and 86.7 wt % CNC. Dark gray is parallel to the flow direction and light gray is perpendicular to the flow direction. The error bars are the standard error for each set of films.

Flocculation of the dispersions prior to film casting also caused a reduction in the mechanical properties of the films when compared to the non-flocculated pure CNC film. This could be due to a reduction in the density of the films caused by gaps left between the flocs during drying. Interestingly, although the flocculated films show optical anisotropy, they exhibit little mechanical anisotropy. In the cases where mechanical anisotropy is present, the films typically have higher mechanical properties in the direction perpendicular to flow. The addition of PEO to the flocculated films has little effect on the mechanical properties when compared to the flocculated pure CNC film. This suggests that the flocs are the load bearing structure in these films.

4.5 CNC MEMS (1st Generation)

4.5.1 CNC MEMS Films

The fabrication of MEMS from CNC requires the ability to form smooth and uniform CNC films that adhere to both silicon and photoresist surfaces. Ordering of the CNC in the films could result in anisotropic mechanical properties that can be taken advantage of for novel MEMS devices. The films need to be stable enough to withstand the MEMS fabrication process, including exposure to water and some organic solvents. CNC films have been prepared on both substrates. Additionally, free standing films were made in order to study film microstructure.

4.5.1.1 CNC Films on Silicon

Initial attempts at dip coating and doctor blade coating of aqueous CNC dispersions onto silicon wafers resulted in the dispersion beading up in the center of the wafer and an uneven coating of the surface upon drying. The coating was improved by using a CNC dispersion in 70% ethanol, however the effects of the new solvent on the liquid crystalline phase behavior of the dispersion were unknown. Another method for improving the wettability of the silicon was a surface modification with aminopropyltrimethoxysilane (APTMS). This modification not only hydrophilizes the surface but the positive dipole of the amine acts as an adhesion promoter for the negatively charged CNC. The best films were prepared by immersing an APTMS modified silicon wafer into 0.61 vol. % CNC for 2 minutes. After removal non-adsorbed CNC was rinsed off by dipping in THF and the film was allowed to dry vertically. The resultant film appeared macroscopically smooth and uniform. AFM images of the film were taken in 3 locations on the film to test for variation in film roughness (Figure 4.24). Root mean squared (RMS) roughness values ranged from 4.0-5.5 nm and thicknesses ranged from 2.3 to 3.5 microns. Due to the vertical drying position some gravity induced alignment of the CNC is seen in the AFM image. CNC films were also prepared from CNC-HCl and CNC-AA. These films had RMS roughness values of 27.5 and 31.2 nm for CNC-HCl and CNC-AA, respectively. The increased roughness is due to the aggregates in the dispersion and could cause problems in MEMS devices. Current silicon devices have surface topographies that span the RMS roughness range of 0.2 to 15 nm.[94]

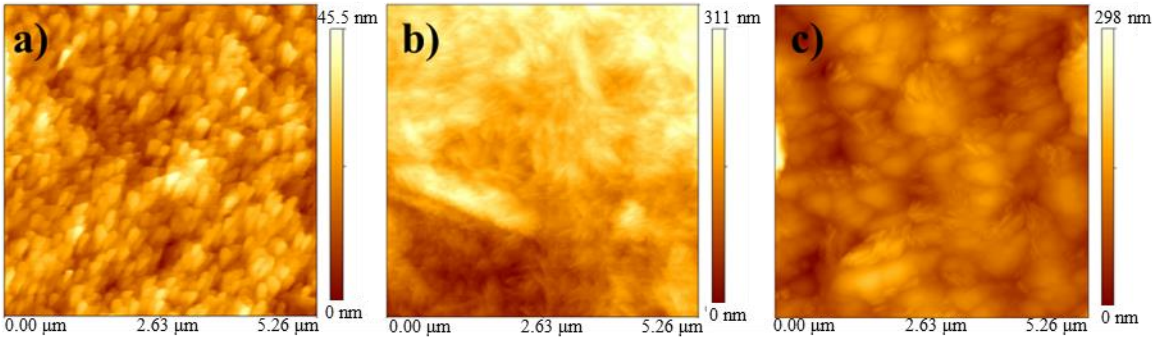

Figure 4.24 AFM images showing the surface topography of (a) CNC-SA, (b) CNC-HCl, and (c) CNC-AA films on silicon substrates.

4.5.1.2 CNC Films on Photoresist

Poor wettability of the hydrophobic polymeric photoresist layer again caused the aqueous dispersions to bead up in the center of the substrate resulting in poor uniformity of the film. APTMS could not be used to modify the surface because THF dissolved the photoresist layer. Therefore, an air plasma treatment was used to hydrophilize the surface. In this treatment, the top layer of photoresist was bombarded with oxygen ions from the air. In competing processes the ions both etch the surface of the photoresist and react to form oxygen containing groups on the surface. An untreated photoresist film had a water contact angle of 57^o and an RMS roughness of 0.24 nm. By varying the treatment zone, power and time a treatment protocol was determined that significantly hydrophilized the surface without causing significant damage. Treatment in the direct plasma stream was extremely effective in hydrophilizing the surface resulting in a contact angle of 12.5^o. However, the RMS roughness of the surface was increased to 1.18 nm. By treating outside the direct plasma stream in the quiescent zone the increase in roughness was minimized while still significantly decreasing in the water contact angle. Table 4.1 shows contact angle and RMS roughness values for photoresist surfaces treated using a variety of protocols. It was determined that for MEMS fabrication treatment in the quiescent zone at 100 W for 60 s would result in the best balance of etching and hydrophilization. This treatment resulted in a contact angle of 16.4^o and a RMS roughness of 0.80 nm.

Table 4.1 Water contact angle and RMS roughness of photoresist films after various air plasma treatment protocols.

Treatment Zone	Treatment Power	Treatment Time	Contact Angle	RMS Roughness
Untreated	N/A	N/A	57.0^o	0.24 nm
Direct	50 W	60 s	12.5^o	1.2 nm
Quiescent	50 W	60 s	19.5^o	0.29 nm
Quiescent	50 W	30 s	19.9^o	0.59 nm
Quiescent	50 W	10 s	15.9^o	0.54 nm
Quiescent	10 W	60 s	18.7^o	0.87 nm
Quiescent	100 W	60 s	16.4^o	0.80 nm

4.5.2 CNC Film Stabilization

During MEMS processing, the CNC films are exposed to an aqueous photoresist developer and to acetone, used a photoresist stripper. Therefore, the films must be stable when exposed to acetone and water. Wetting tests showed that the films were not affected by acetone, however after short periods of exposure to water, CNC films would begin to soften, swell, and redisperse. It has been shown that a mild thermal treatment will render the films stable in water.[71] The exact mechanism of the stabilization is unknown, although it has been suggested that desulfation renders the films stable in water.[95] It was found that treatment at 105 ^oC overnight would stabilize the film and prevent it from swelling and redispersing when exposed to water. A milder treatment at 60 ^oC under vacuum was also sufficient to stabilize the film.

At such low temperatures desulfation of the CNC should not occur. Roman and Winter found that the onset temperature for CNC degradation due to desulfation occurs above 180 ^oC.[96] TGA-FTIR was used to explore the mechanism of stabilization. The TGA curves (Figure 4.25) show the main difference between heat treated and non-heat treated films was the amount of residual water evaporating between 20 and 120^oC. After heat treatment, residual water decreased from 5.4% to 2.9%. Each film shows significant mass loss at 180°C which is not seen in the decomposition of CNC-HCl or CNC-AA. This mass loss is attributed to desulfation and acid catalyzed dehydration of the CNC. This is corroborated by the FTIR spectra of the decomposition products at 180°C (Figure 4.26) where the peaks between 1000 and 1200 cm^{-1} indicate the removal of sulfate groups. While other groups can result in FTIR peaks in this region, these peaks were not present for CNC-HCl, where there are no sulfate groups on the CNC. Therefore they were attributed to desulfation of the CNC. Since the heat treatment was at T < 180°C, the mechanism of stabilization is not desulfation of the nanocrystals, but is likely a cocrystallization between CNC due to removal of excess water trapped between the particles. A similar mechanism of cocrystallization is well documented in the pulp and paper industry,[97] however in the case of CNC adhesion is likely stronger because there are no amorphous regions in the material.

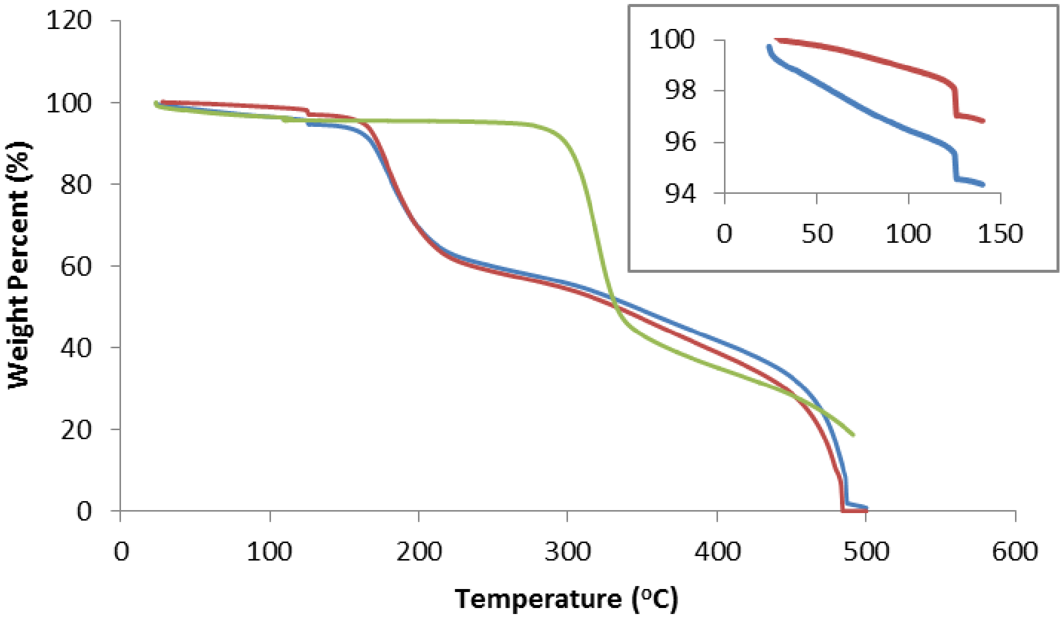

Figure 4.25 TGA weight percent versus temperature curve for (blue) original and (red) heat treated CNC-SA films and (green) CNC-HCl film. The inlay shows water loss up to 120°C for the CNC-SA films.

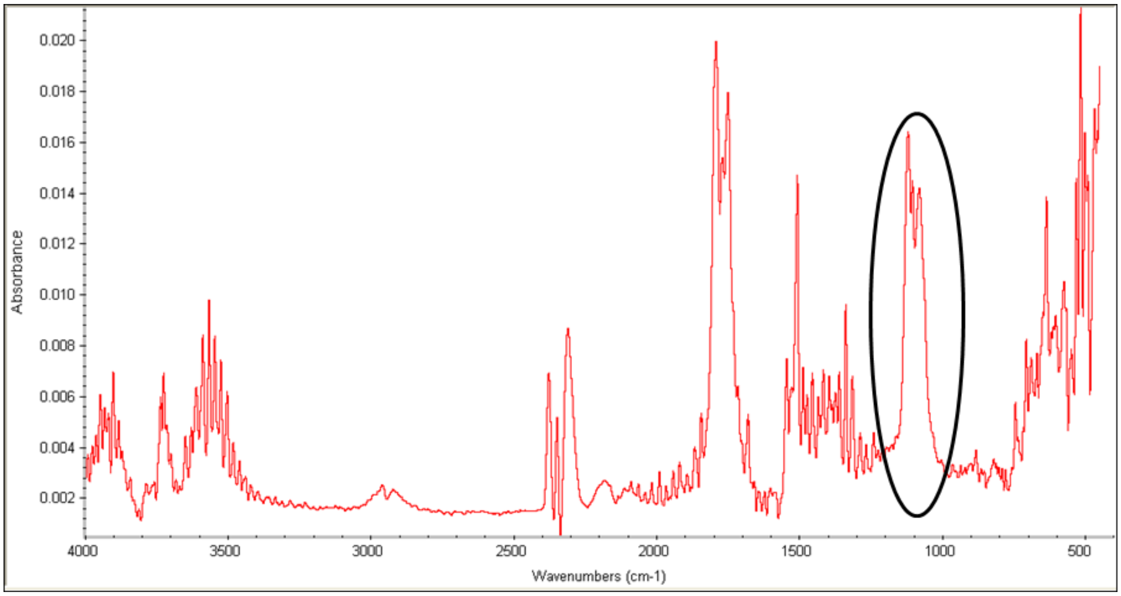

Figure 4.26 FTIR Spectra of CNC-SA film decomposition products at 180°C. The circled peaks between 1000 and 1200 cm^{-1} indicate removal of sulfate groups.

4.5.3 MEMS Test Platform Design

A MEMS test platform was designed with test structures to allow for the measurement of four material properties of the CNC film. A test platform with each microinstrument on the same module ensured that each device was exposed to identical experimental characteristics. Each module includes numerous copies of each device to test for any local variation in film properties. Additionally, devices on each module were designed with varying orientation to test for anisotropic properties caused by alignment of CNC in the film. Since the properties of the film were initially unknown, each device was designed over a range of size scales. A schematic of the test module scaled for use on a 4" wafer is shown in Figure 4.27. Each device was designed to be fabricated from a single 3 μm thick CNC film. This will required the use of two photomasks; one to create holes to anchor the devices to the substrate and a second to shape the microinstruments themselves. Both masks were designed using Layout System for Individuals (LASI) software.

Test devices included the residual stress tester (RST), the mechanical strength tester (MST), the resonator, and the cantilever beam array (CBA). A schematic of each test device is shown in Figure 4.28. All devices were modeled after those of Naveed Ansari.[94] The RST was used to measure the residual stress in a released CNC film. RSTs consists of a suspended I-shaped beam that is supported when released by two thin cantilever beams located equidistant from the midpoint of the central arm. Since the supporting beams are located on opposite sides of the central arm when released a torque is induced at the center of the I-shaped beam causing it to rotate. By measuring the rotation of the beam the residual stress in the film could be calculated using Equation 4.2.

$$\sigma_R = \frac{E\theta d}{2} \tag{4.2}$$

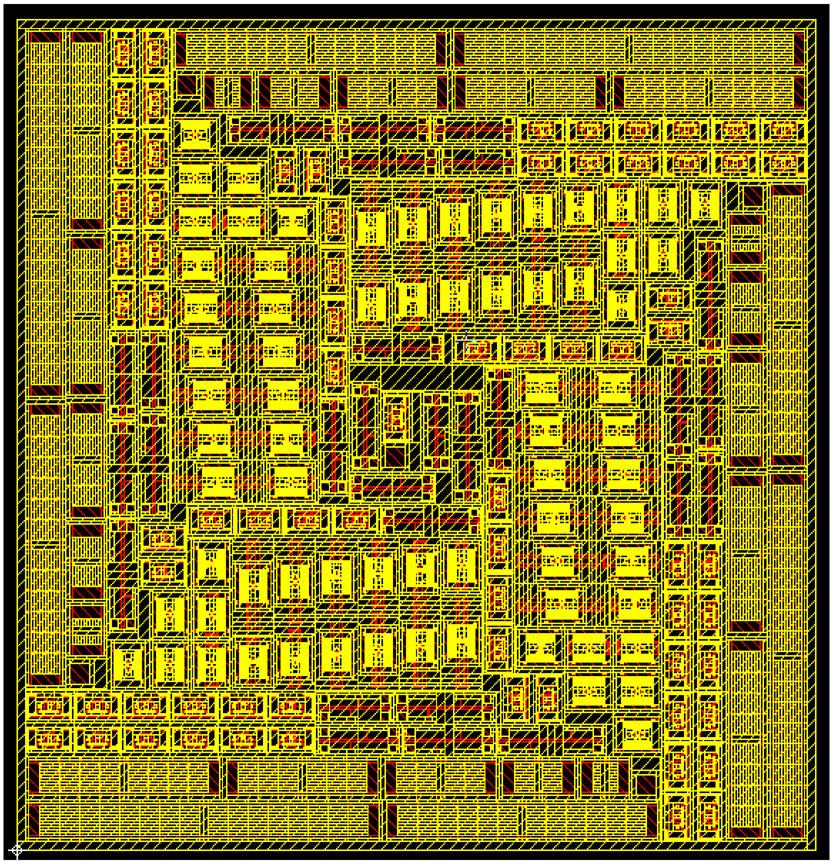

Figure 4.27 LASI layout of CNC MEMS module.

here, σ_R is the residual stress in the film, E is the elastic modulus of the film, θ is the amount (in radians) that the I-shaped beam rotates, and d is the distance between the two supporting beams. Since the residual stress was unknown, RSTs were designed with d ranging from 100 to 500 μm, to account for the possibility of residual strain induced fracture in the smaller devices.

MSTs were used to determine the fracture strength of the CNC film. They consisted of a central shuttle supported on each side by two flexure beams. Each side of the shuttle had three fracture beams of length 50, 60, and 70 μm. While the fracture beams on each device had the same width, there were three sets of devices on the test platform with beam widths of 3, 4, and 5 μm. The device was actuated by a micromanipulator that pushed on the central shuttle until the beams were fractured by the anchored stoppers. By measuring the distance the shuttle has traveled at fracture, the fracture strain of the film was calculated using Equation 4.3.

$$\epsilon_f = \frac{3w\delta_f}{2L_c^2} \tag{4.3}$$

here, ϵ_f is the fracture strain, w is the width of the fractured beam, δ_f is the shuttle displacement at fracture, and L_c is the distance between the shuttle and the anchored stopper. This equation was used to design the lengths and widths of the fracture beams of the MST using an estimated fracture strain of 1.5% as determined from a tensile test. Estimated fracture displacements were between 3.50 and 12.6 μm which were in the measurable range.

The resonators were used to determine the elastic modulus (E) of the CNC film. They consisted of two banks of interlocking comb fingers on each side of a moveable shuttle. The shuttle was suspended by two sets of flexure beams, each consisting of four beams connected to each other by a truss. The resonator was actuated electrostatically by a drive signal that is increased from zero until it reached the resonance frequency of the device. The resonance frequency was determined by a number of device parameters including the length of the supporting beams, and can be expressed by Equation 4.4, which was derived from the harmonic oscillator equation.

$$f_R^2 = E\left(\frac{tw^3}{2\pi^2 M_{eff} L^3}\right) \tag{4.4}$$

here, f_R is the resonance frequency of the resonator, t, w, and L are the thickness, width, and length of the supporting beams, respectively, and M_{eff} is the effective mass of the shuttle. When all variables are measured this equation can be used to determine the elastic modulus of the CNC film. Resonators were designed using an estimated elastic modulus of 6.7 GPa, based on nanoindentation measurement of a CNC-SA film. M_{eff} was determined using the density of CNC (1.636 g/cm^3). Using these values a number of resonators were designed with supporting beam length between 100 and 500 μm. Length variations in the supporting beam length were used to account for any differences between the estimated and actual values.

The cantilever beam arrays (CBA) were used to determine the residual stress gradient in the film. Each CBA consisted of 20 cantilever beams of 30 μm width with 5 μm spacing between cantilevers. Since the residual stress gradient in the CNC film was unknown, CBAs were designed with lengths ranging from 100 to 2000 μm to encompass a large range of possibilities. The reason for using a CBA instead of a single beam is to minimize any variance in the boundary conditions where the beam is connected to the substrate. Analysis of the CBA after release involved measuring deflection and curvature of the beam. From the profile of the beam, the residual stress gradient can be determined using a number of methods, such as that of Fang and Wickert.[98] In this method, the rotation and curvature components of the beam deflection are decoupled and used to derive the mean and gradient components of the residual stress, respectively.

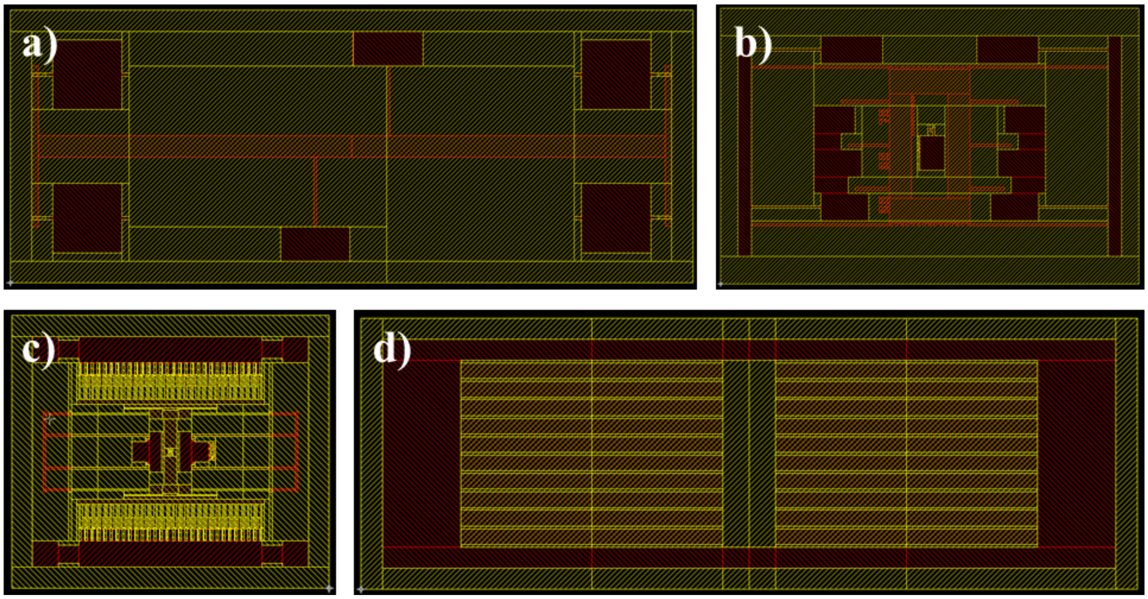

Figure 4.28 LASI layout of a) residual stress tester, b) mechanical strength tester, c) resonator, and d) cantilever beam array.

4.5.4 MEMS Fabrication Process

The CNC MEMS fabrication process can be broken down into seven basic steps: 1) coating of substrate with photoresist, 2) UV exposure and development, 3) CNC film formation, 4) coating of CNC film with photoresist, 5) alignment, UV exposure, and development, 6) plasma etching, and 7) release. In the first step, silicon wafers were coated with hexamethyldisilazane (HMDS), which acted as an adhesion promoter between the wafer and the photoresist. Spin coating was used to coat the substrate with a photoresist film. It was determined that a spin speed of 5000 rpm would result in a 4.2 μm film. This is twice the thickness of sacrificial layer used by Ansari,[94] however spinning at higher speeds results in non-uniform striations in the photoresist film. For films of this thickness, 90 s on a hot plate at 110^{o}C was a sufficient soft bake to remove solvent from the photoresist film.

The light energy dose necessary for photolithography varies with the photoresist film thickness. Dose is simply a product of the exposure time and light intensity. If the dose is insufficient, called underexposure, the photoresist will not become completely soluble in the developer and the pattern will only partially develop. In the case of overexposure, when too much light energy reaches the photoresist, stray light can reach areas that are supposed to be masked. The correct dose of light energy was determined by trial and error on a series of photoresist covered wafers. It was found that for a 4.2 μm thick AZ P4620 photoresist layer three cycles of 5 seconds of exposure, with 30 seconds of wait time between exposures resulted in good pattern resolution. The wait time between exposures was to allow for outgassing of nitrogen produced by the chemical reaction in the film. Images of patterned and developed photoresist, both overexposed and optimally exposed, are shown in Figure 4.29.

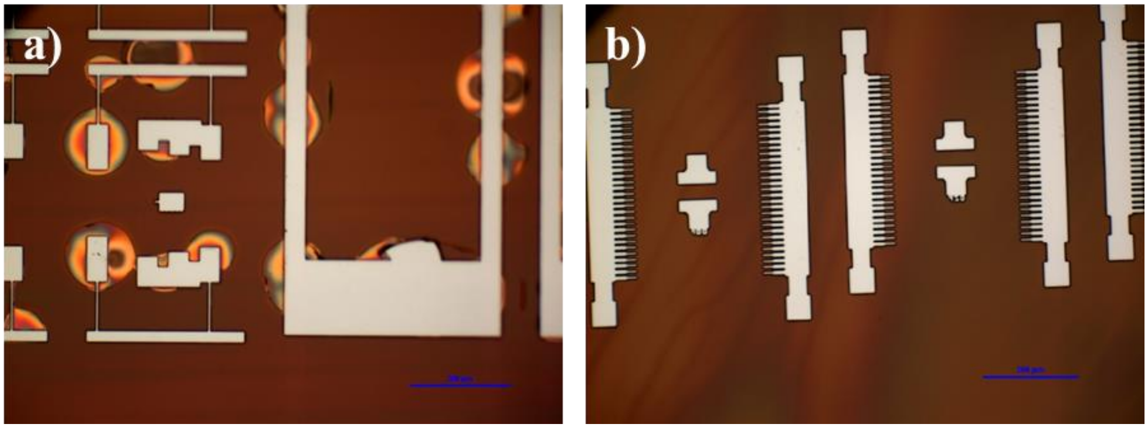

Figure 4.29 Developed patterns in photoresist film where (a) is an example of overexposure and (b) shows good resolution after a correct UV radiation dose. Scale bars are 200 μm.

Cellulose nanocrystal films were deposited by dip coating or doctor blade coating onto the photoresist layer with adhesion promoted by air plasma treatment. Films were prepared from either CNC-SA or CNC-HCl. Additional problems with hydrophobic hydrophilic interactions were encountered with the second photoresist layer. After deposition, exposure, and developing of the photoresist the majority of the unexposed regions did not adhere to the cellulose surface. During developing, the photoresist would separate from the surface, float, and deposit elsewhere after drying. An example of this is shown in Figure 4.30 where MST photoresist pieces shifted position. HMDS treatment of the CNC film was used to promote adhesion between the layers and resulted in some improvement but there were still some problems with photoresist adhesion to the CNC layer. Despite these issues, in 1st generation devices, we showed that the desired patterns could be etched into CNC films. However, the etch time used was too low and the device was not functional. Figure 4.31 shows images of failed fabrication attempts of CBAs in both CNC-HCl and CNC-SA.

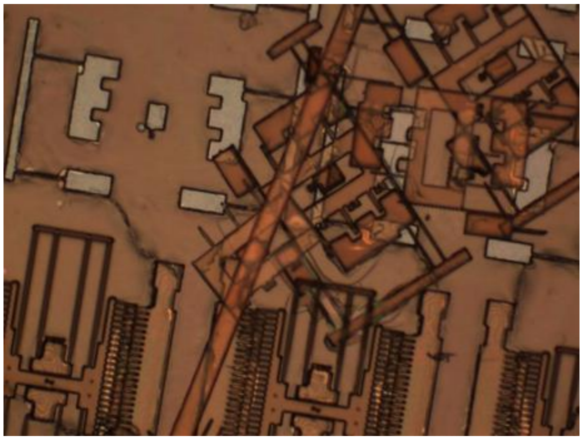

Figure 4.30 Adhesion problem between CNC film and second photoresist layer. During developing, the photoresist separated from the surface and deposit elsewhere after drying.

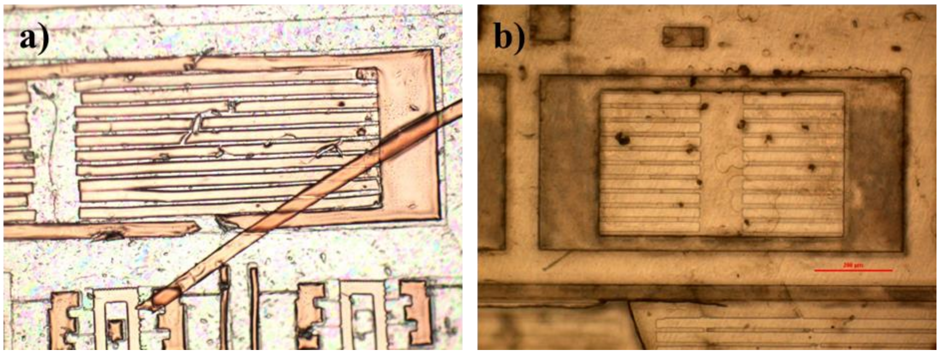

Figure 4.31 Failed fabrication of CBAs where in (a) there is severe cracking of the photoresist layer due to CNC-HCl aggregates and (b) incomplete etching of the CNC-SA film resulted in a non-functional device.

4.6 CNC MEMS (2nd Generation)

As described in Section 4.5, in the early part of this work, a CNC MEMS test platform was designed and devices were fabricated as a proof of concept. Later, in collaboration with Partha Saha, the CNC MEMS fabrication process was improved and functional CNC MEMS devices were fabricated and tested. Additionally, doubly clamped beam arrays (DCB) were added to the platform. Examples of each device are shown in Figure 4.32.

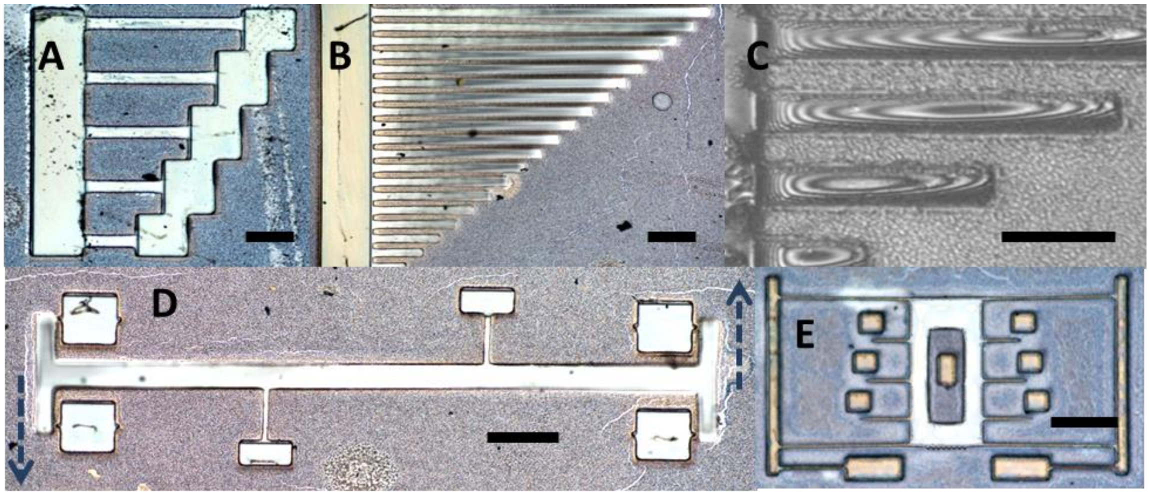

Figure 4.32 Representative reflected light microscopy images of CNC-MEMS devices. A) doubly clamped beam array (DCB), B) Cantilever beams array (CBA), C) Interferograms of the cantilevers in (B) obtained using phase shifting interferometry

(PSI), D) Residual stress tester (RST), and E) Mechanical strength tester (MST). Scale bars are 100 µm. (Images by Partha Saha)

4.6.1 MEMS Fabrication Process

The initial steps of the MEMS fabrication process were the same as in 1st generation CNC MEMS. However, after the CNC film is deposited on the patterned photoresist surface, the process changes for the 2nd Generation CNC MEMS. Figure 4.33 shows the evolution of CNC-MEMS devices through a surface micromachining approach, starting with a shear dried CNC film (Figure 4.33A) on a patterned photoresist film. Next, A 10 nm Ti/-TiO_2 layer was then e-beam deposited on the CNC; this changed the reflected color under cross-polarized light (Figure 4.33B). The thin layer of Ti/-TiO_2 was used as a novel method for improving the adhesion and curing of the second layer of photoresist to the CNC film. Figure 4.33C shows the cured structural profile of MSTs after deposition, and development of the second patterned photoresist layer. In the next step, the parts of the CNC film which were not masked by the photoresist layer were plasma etched. An inductively coupled plasma (ICP) system with a bias voltage was used to achieve anisotropic/directional etching[99] resulting in a device structure with residual photoresist on top of and beneath it (Figure 4.33D). A combination of CF_4 and O_2 was used with very short plasma cycles to prevent micro-crack formation and photoresist rounding problems. Figure 4.33E and Figure 4.33F show the etched MSTs after washing of the residual photoresist layers using acetone and isopropyl alcohol followed by drying in a critical point drier.

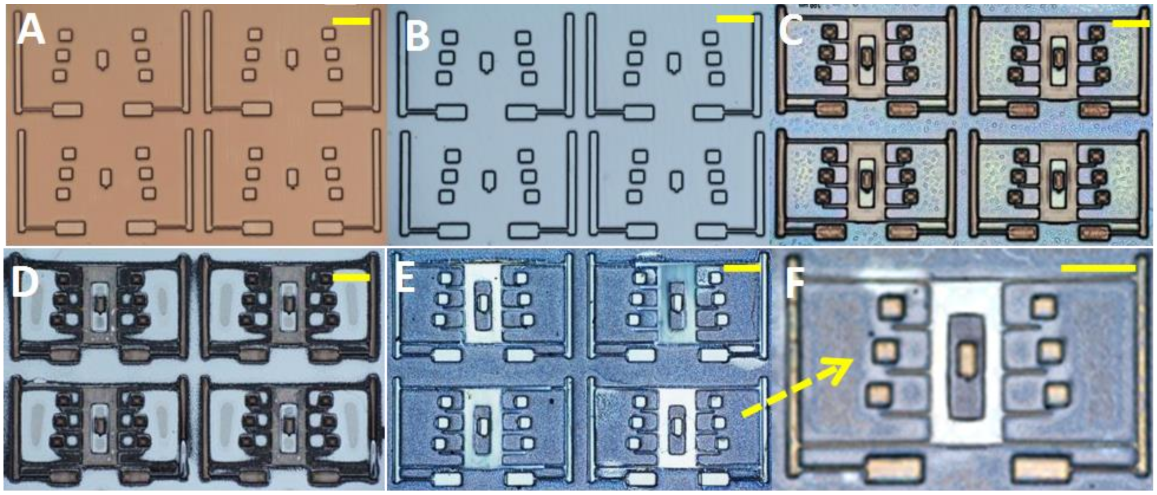

Figure 4.33 Reflected optical microscopy images showing the steps involved in photolithographic fabrication scheme for 2nd Generation CNC MEMS. A) CNC film on a patterned photoresist layer. B) Same CNC film after E-beam deposition of 10 nm thick Ti/TiO_2 layer. C) After creating the device pattern using a second photoresist layer achieved by photoresist coating, drying, UV exposure through aligned mask, and developing. D) Etched out device profiles after using inductively coupled plasma, white and black areas indicate etched film and residual photoresist film respectively. E) Released devices after washing off residual photoresist layers using acetone followed by IPA rinsing. F) Higher magnification image of a released MST device after critical point drying. Scale bars are 100 µm. (Images by Partha Saha)

4.6.2 Anisotropic Properties

The micromechanical devices made from the CNC films were freestanding and possessed tunable mechanical and optical properties. The reflected optical microscopy images in Figure 4.34 show the effects of thickness and shear alignment on the anisotropic stress gradient in suspended cantilever beams. When the CNC were aligned parallel to long axis of the beam they exhibited significantly less curvature than when they were oriented perpendicular to the long axis. This effect was more pronounced for the 2 µm thick beams (Figure 4.34A and C) than the 4 µm beams (Figure 4.34B and D). Similarly, RSTs exhibited more curvature when CNC were aligned perpendicular to the beam’s long axis than when aligned parallel to the long axis. The stress gradient decreased with thickness.

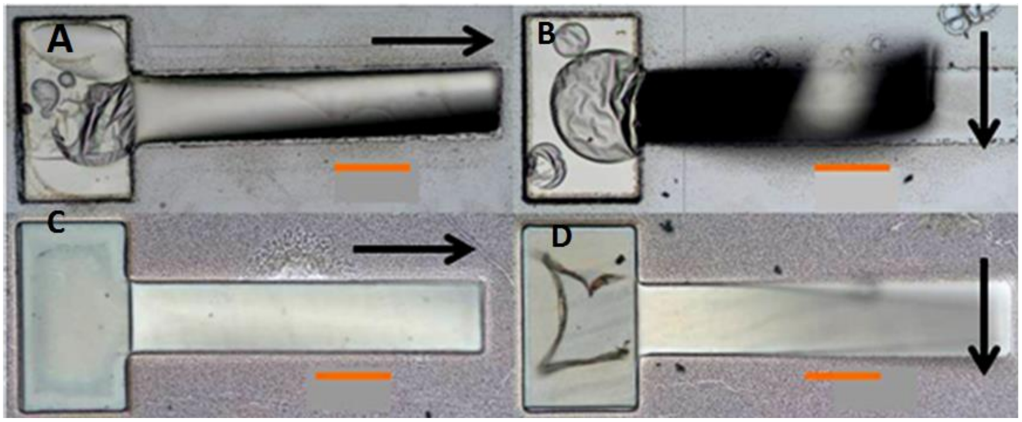

Figure 4.34 Reflected microscopy images showing the effect of the stress gradient developed in CNC cantilevers depends on the CNC alignment direction and device thickness. Arrows show the shear alignment direction. (A), (B) and (C), (D) show 2 µm and 4 µm thick released cantilevers respectively. Scale bars are 50 µm. (Images by Partha Saha)

4.6.3 Mechanical Properties

Phase shifting interferometry (PSI) was used to determine the suspended cantilevers' height profile and the nature of the stress gradient. The PSI based height profile (Figure 4.35A) for a 300 µm long cantilever shows the freestanding microstructure with a downward arc like curvature confirming the compressive stress gradient. Based on linear elastic theory for DCBs, the elastic modulus of CNC-MEMS was derived using point load beam deflection by nanoindentation.[100-101] As longer doubly clamped beams buckled more, only the linear region of the force versus deflection curve was considered to determine the slope (µN/µm) for the 100 µm long DCB; this value was further used for the elastic modulus calculation (Figure 4.35B). The thickness and width of the DCBs were measured using SEM and optical microscopy. The elastic modulus for CNC-MEMS beams measured from three separate wafers was 56 ± 22 GPa for 2 µm thick beams and 72 ± 14 GPa for 4 µm thick beams. The variation in mechanical property measurements is attributed to variations in shear, thickness, drying and fabrication conditions between manually prepared wafers. The compressive residual stress developed in the 2 μm and 4 μm thick film was a 244 ± 93 kPa and 55 ± 11 kPa respectively based on the microscopically measured angle of rotation of the released RSTs (Figure 4.36). Figure 4.35C shows the MST actuation graph for 4μm thick device showing the fracture distance of 4.82 μm for 60 μm long fracture beams on the suspended shuttle while the shuttle was pushed against the stopping posts. Based on the distance travelled by the shuttle in *x*-direction before suspended beam fracture occured, the fracture strength of the 4 μm thick MST was 2.0 ± 0.4 GPa. The MSTs made from 2 μm thick films were more flexible and the suspended beams did not fracture even at the maximum shuttle displacement possible for this structure. A summary of the measured mechanical properties is in Table 4.2.

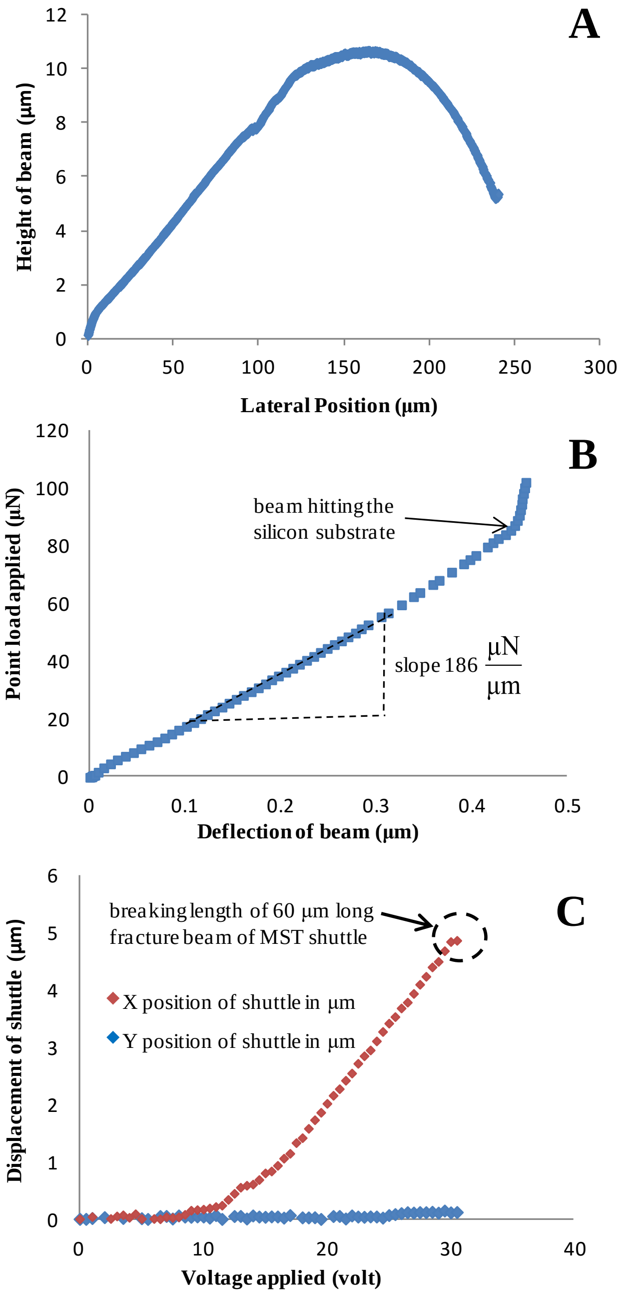

Figure 4.35 Micromechanical property analysis graphs of CNC-MEMS devices. A) Height profile for a 300 µm long, 30 µm wide, and 2 µm thick suspended cantilever showing complete suspension with a compressive stress gradient. B) Force versus deflection curve for 100 µm long DCB with 2 µm thickness, triangle shows the selected linear region used to extract the slope needed for elastic modulus calculation following linear-elastic beam theory. (C) Change in X and Y position of MST shuttle (4 µm thick) during mechanical actuation using an open loop piezo assisted micromanipulator, the suspended shuttle was pushed towards X direction until 60 µm long fracture beams on both sides fractured giving the breaking length for fracture strength calculation. (Data by Partha Saha)

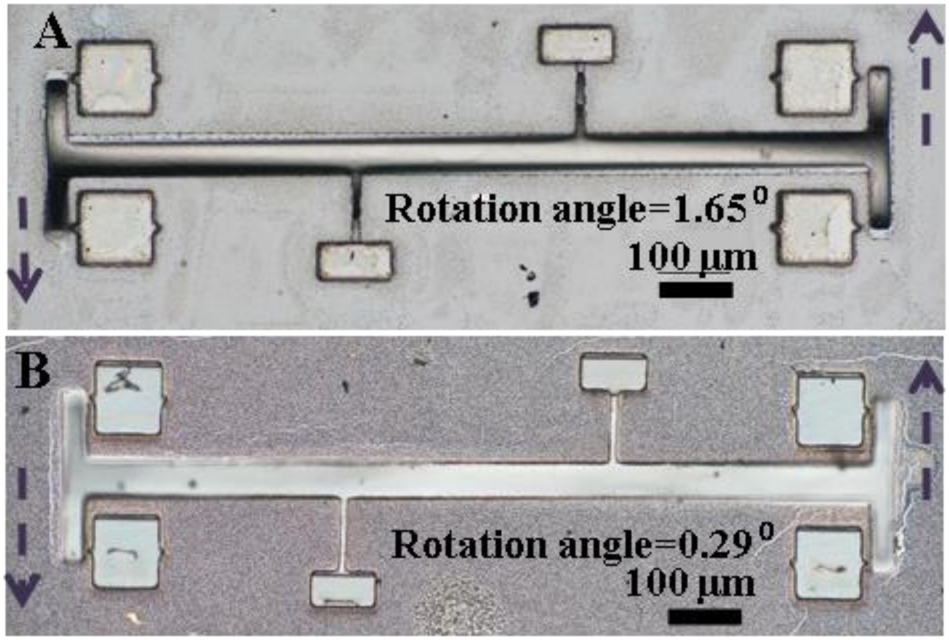

Figure 4.36 Reflectance micrograph showing thickness dependent compressive stress developed in CNC-RSTs. Anti-clockwise rotation in (A) 2 µm and (B) 4 µm thick RSTs with a lever arm of 300 µm; I shaped beam is along the shear alignment direction of individual nanocrystals. (Images by Partha Saha)

Table 4.2 Summary of CNC MEMS mechanical properties. (Data by Partha Saha)

Micromechanical properties of CNC-MEMS	Elastic Modulus E (GPa)	Residual Stress σ_R (kPa)	Fracture Strength σ_f (GPa)
Equations used for calculations	$I = \frac{wt^3}{12}$ $E = \frac{mL^3}{192I}$	$\sigma_R = \frac{E\theta d}{2}$	$\sigma_f = \frac{3Ew\delta_f}{2L_c^2}$
2 µm thick devices	56 ± 22	244 ± 93	Did not fracture
4 µm thick devices	72 ± 14	55 ± 11	2 ± 0.4

Chapter 5 Chiral Films for Optical Applications

There are two possible methods to prepare CNC films with controlled chiral structure using shear. The first is to apply shear at low rates to control the unwinding of the cholesteric pitch. The second is to shear at high rates, and control the relaxation during drying to lock in the desired pitch. The shear rates required for the first method are too low for high throughput processing, therefore, we decided to first explore the second method. In order to precisely control the helix alignment and pitch through shear, it is necessary to first understand the effects of flow on the microstructure of the CNC dispersion as a function of original microstructure, shear rate, and relaxation time. This chapter summarizes the results from collaborative research between the Davis Group at Auburn University and the Green Group at Texas A&M University on experiments and modeling to understand the effect of shear on cholesteric CNC liquid crystals and their processing into chiral films.

5.1 Rheo-SANS of CNC

5.1.1 CNC Characterization

The rheological properties and liquid crystalline phase behavior of CNC dispersions are strongly influenced by size distribution and electrostatic stabilization. This portion of the research used CNC from the US Forest Service’s Cellulose Nanomaterials Pilot Plant at the Forest Products Laboratory (Lot # 2012-FPL-CNC-051). Based on AFM, the average CNC length was 163 nm with a standard deviation (σ) of 43 nm, the average width was 33 nm (σ = 7.2 nm), and the average height was 6.3 nm (σ = 1.6 nm).

5.1.2 Phase Behavior and Microstructure

Due to their anisotropic shape and rigidity, CNC follow lyotropic liquid crystalline phase behavior and aqueous dispersions are known to form cholesteric liquid crystals.[12] Figure 5.1 show cross-polarized optical microscope images of the CNC dispersions from 3.16 to 8.48 vol %. At 2.49 vol %, the dispersion was completely isotropic. At 3.16 vol %, a few small liquid crystalline droplets were dispersed in a predominantly continuous isotropic phase, indicating the isotropic to biphasic transition concentration $\phi_I \approx 3.16$ vol %. At 3.83 vol % the number of liquid crystalline droplets in the dispersion significantly increased. As the concentration was further increased, the fraction of liquid crystalline phase increased and the anisotropic droplets became larger. At 5.83 vol %, the droplets appeared to merge; the microstructure suggests a co-continuous matrix of isotropic and liquid crystalline phases. Between 3.83 and 5.83 vol % the dispersions had the layer-like striped disclination pattern typical of cholesteric droplets with perpendicular surface anchoring.[102] At 6.50 vol % the image was completely birefringent and displayed a variety of colors; the characteristic fingerprint pattern of a cholesteric liquid crystal was not observed. At 7.16 vol % and above, the dispersions had the random bright colorful texture expected of a birefringent gel.

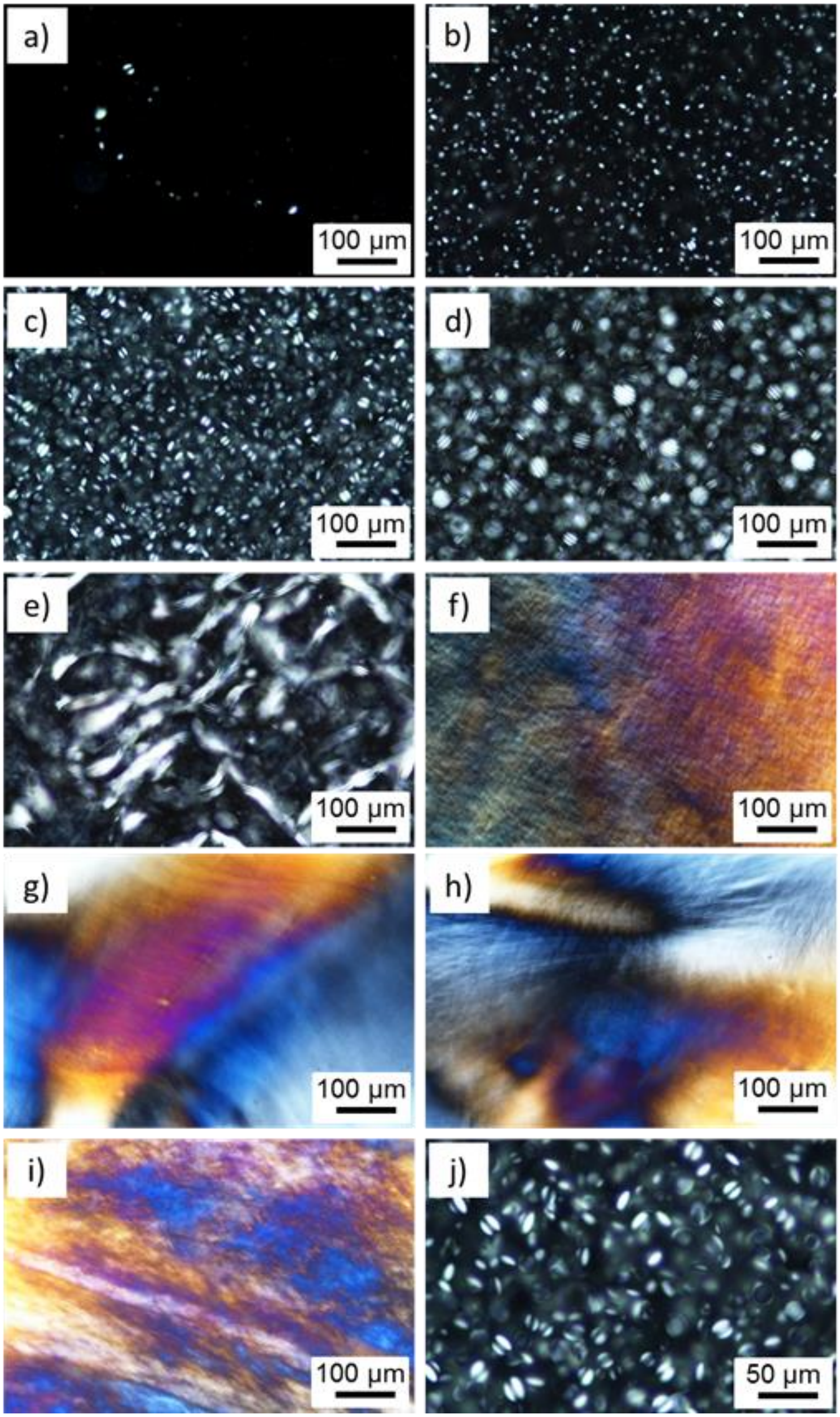

Figure 5.1 Polarized optical microscopy images of CNC dispersions at a) 3.16, b) 3.83, c) 4.50, d) 5.16, e) 5.83, f) 6.50, g) 7.16, h) 7.82, and i) 8.48 vol %. In j) the 4.50 vol % image is magnified to clearly show the texture of the liquid crystalline droplets.

5.1.3 Viscoelastic Properties

The storage modulus G’, loss modulus G”, tan δ = G”/G’, and complex viscosity η^* are shown in Figure 5.2. Biphasic samples $3.83 < \phi < 5.83$ vol % behaved as predominantly viscous fluids (tan $\delta > 1$), while for $\phi > 6.50$ vol % the dispersions were elastic fluids (tan $\delta < 1$). A significant decrease in tan δ was seen between 6.50 and 7.16 vol %. Additionally, at 6.50 vol % there was still a dependence of G’ on ω, while at 7.16 vol % and higher G’ was independent of ω. This, along with the microscopy images (Figure 5.1) and the steady shear rheology data discussed below, indicates that 6.50 vol % is near the liquid crystalline to gel transition concentration.

5.1.4 Steady Shear Rheology

As shown in Figure 5.3, the steady shear rheology of CNC in D_2O had similar features to the previous studies in water. In the isotropic regime at 2.49 vol % the behavior was nearly Newtonian. At 3.16 vol %, near the onset of the biphasic regime, the onset of shear thinning was at 10 s^{-1}. The 3.83, 4.50, 5.16, and 5.83 vol % dispersions exhibit three region behavior similar to that which is typically associated with lyotropic liquid crystalline dispersions; the inset of Figure 5.3, more clearly shows this behavior for the 4.50 vol % dispersion.[45] This behavior has often been seen in biphasic CNC rheology, and was observed by Orts et. al. for liquid crystalline CNC.[67] While the origin of region I, the initial shear thinning region, remains controversial,[103-104] it is typically attributed to director tumbling or variations in the polydomain defect texture of the liquid crystal with flow.[83] The region II plateau at intermediate shear rates is commonly attributed to director wagging or alignment of the rods in the vorticity direction, while the

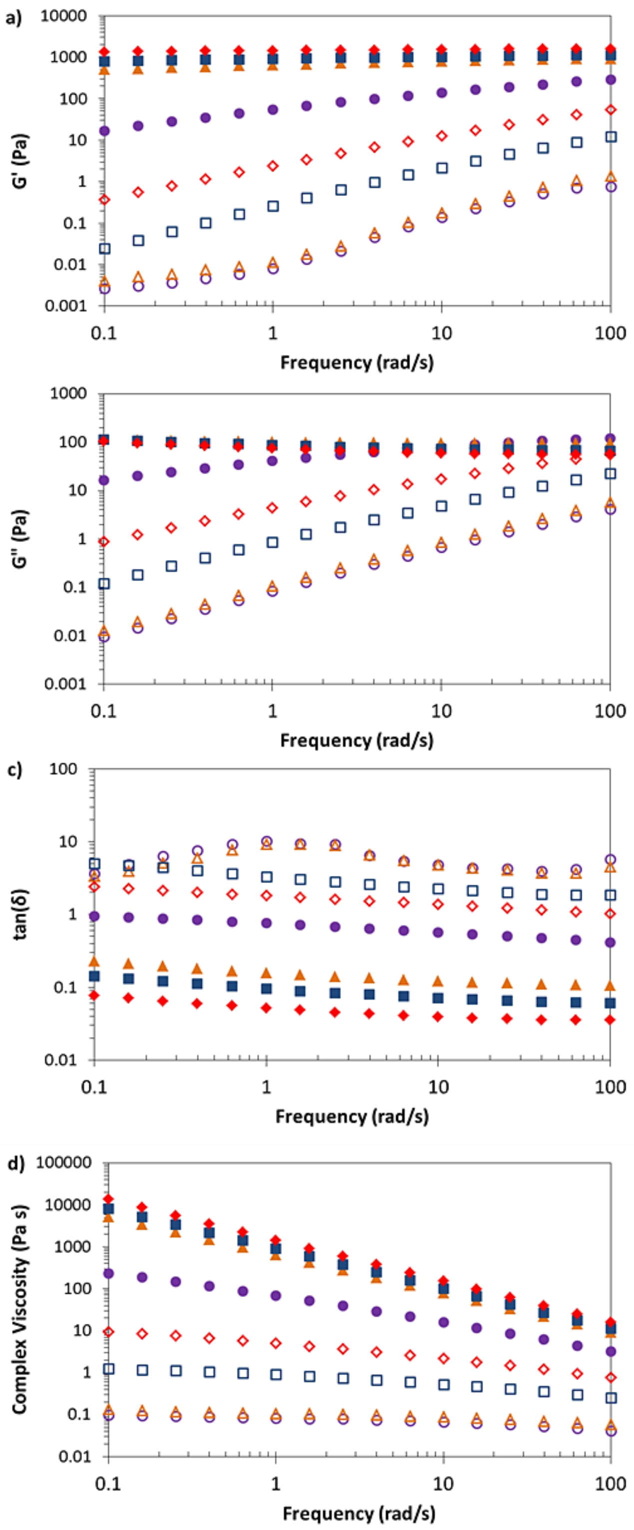

Figure 5.2 Linear viscoelastic properties of CNC dispersions at 3.83 vol % (purple open circles), 4.50 vol % (orange open triangles), 5.16 vol % (blue open squares), 5.83 vol % (red open diamonds), 6.50 vol % (purple closed circles), 7.16 vol % (orange closed triangles), 7.82 vol % (blue closed squares), and 8.48 vol % (red closed diamonds).

final shear thinning region III is caused by particle alignment in the flow direction.[19, 42, 47] In this case, the onset of the region II plateau was 0.398 s^{-1} for the 3.83 vol % dispersion and shifted to lower shear rates as concentration increased, taking place at 0.251 s^{-1} for 4.50 vol % and 0.0398 s^{-1} for 5.16 and 5.83 vol %. As in several other nanocylinder dispersion rheology studies,[19, 31, 64, 105-106] region II was not as flat or as broad as was often observed for lyotropic liquid crystalline polymers.[45] In the gel regime $\phi > 6.50$ vol % the samples were power law fluids, $\eta = K\dot{\gamma}^{n-1}$; where η is viscosity, $\dot{\gamma}$ is shear rate, K is the consistency coefficient, and n is the rate index. The values of n are shown in Table 5.1 for both regions I and III where applicable, as well as shear rates at region transitions. There is a significant shift in the rate index between 6.50 and 7.16 vol % consistent with a liquid crystalline to gel transition.[19]

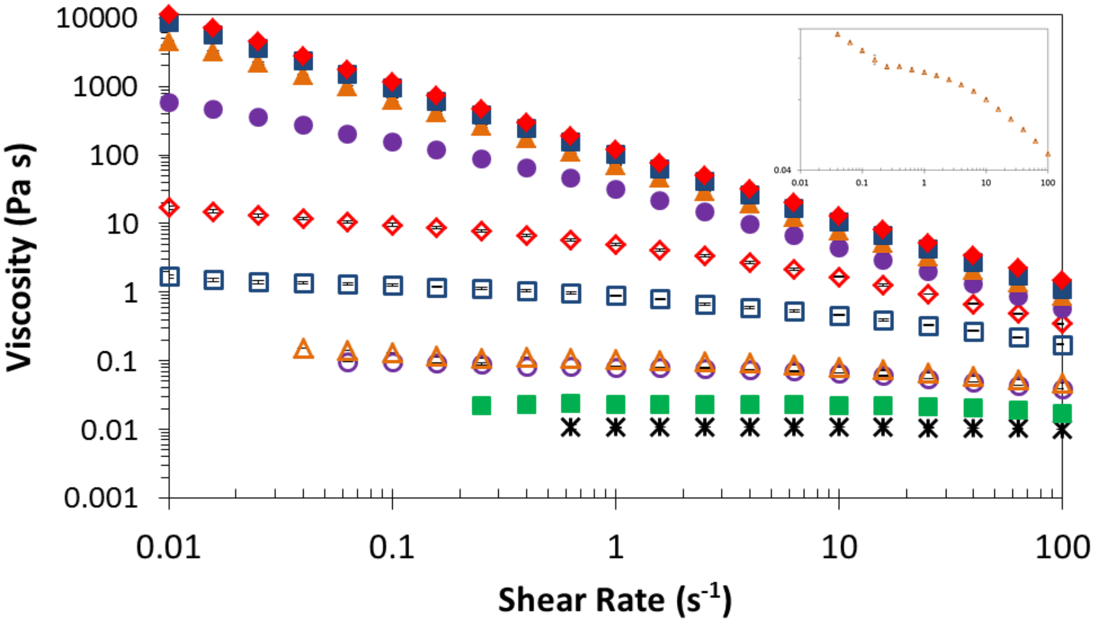

Figure 5.3 Viscosity versus concentration curves for CNC dispersions at 2.49 vol % (black stars), 3.16 vol % (green closed squares), 3.83 vol % (purple open circles), 4.50 vol % (orange open triangles), 5.16 vol % (blue open squares), 5.83 vol % (red open diamonds), 6.50 vol % (purple closed circles), 7.16 vol % (orange closed triangles), 7.82 vol % (blue closed squares), and 8.48 vol % (red closed diamonds). Inset highlights the 4.50 vol % dispersion.

Table 5.1 Shear rate at region transitions and rate index during each region for CNC dispersions from rheology data.

Conc. (vol %)	**Region I →II $\dot{\gamma}$**	**Region I n**	**Region II →III $\dot{\gamma}$**	**Region III n**
3.83	0.398	0.923	2.51	0.936
4.50	0.251	0.824	1.58	0.900
5.16	0.0398	0.837	0.251	0.844
5.83	0.0398	0.728	0.158	0.694
6.50	N/A	N/A	N/A	0.238
7.16	N/A	N/A	N/A	0.059
7.82	N/A	N/A	N/A	0.024
8.48	N/A	N/A	N/A	0.027

5.1.5 Neutron Scattering

In contrast to the rheological behavior typically associated with lyotropic liquid crystalline dispersions, there is no maximum observed in the biphasic region of the viscosity versus concentration curve for CNC.[19, 60-62] Additionally, the three region viscosity versus shear rate behavior is seen in biphasic CNC dispersions but not in fully liquid crystalline dispersions.[19, 60-61] In order to further elucidate the origin of these anomalous rheological behaviors of CNC in the biphasic regime, neutron scattering was used to quantify the structural changes that take place in the dispersions during flow. To collect scattering data for the dispersions at rest, the samples were allowed to relax for up to 60 minutes after loading into the rheometer. Dispersions at 5.83 vol % and below exhibited isotropic scattering patterns after this relaxation time. This shows that although there is local order within the liquid crystalline domains, the dispersion is globally isotropic since the domains had different director orientations. Above 5.83 vol %, anisotropic scattering patterns were observed, due to artifacts from shear associated with loading the sample and slow relaxation kinetics. These dispersions could not be allowed more than 60 minutes to relax due to beamtime constraints, however, at longer times isotropic scattering patterns would be expected. Once scattering data was collected after the initial relaxation time, the samples were subjected to shear at 0.01 s^{-1} to erase any remaining shear history.

Scattering curves for each dispersion at rest are shown in Figure 5.4a. As the CNC concentration increases the position of the peak moved to a higher q value. From this q_{peak} the spacing distance (d) between the rods was calculated using Bragg's law, $d = 2\pi \sin(\theta)/\lambda = 2\pi/q_{peak}$, and is shown in Figure 5.4b.[67] CNC spacing decreased with increasing concentration and was independent of shear rate.

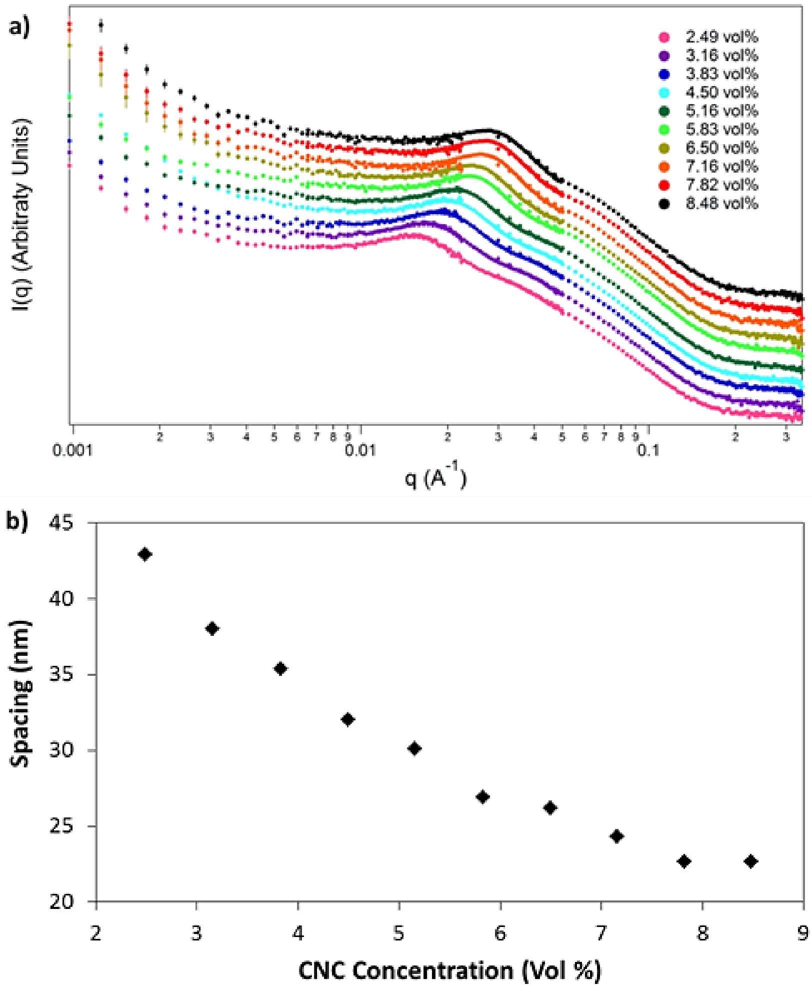

Figure 5.4 a) Scattering curves for each CNC dispersion. For clarity the intensities have been offset on the y axis. b) CNC spacing as a function of concentration as calculated by Bragg's law.

Two-dimensional scattering data for the 2.49, 4.50, and 7.16 vol % dispersions over a range of shear rates are shown in Figure 5.5. Qualitatively, at 2.49 vol % an isotropic ring pattern was observed at all shear rates. For the biphasic 4.50 vol % dispersion, anisotropy was seen in the scattering pattern beginning at $\dot{\gamma} = 0.158\ s^{-1}$. The anisotropy increased with increasing shear rate until $\dot{\gamma} = 0.1\ s^{-1}$. At intermediate shear rates ($\dot{\gamma} = 0.1\text{-}10\ s^{-1}$) the scattering pattern remained relatively constant. High intensity nodes were present perpendicular to the flow direction, while an isotropic ring was still visible. This suggests that while a portion of the rods aligned in the flow direction, some fraction of rods remain randomly aligned. When $\dot{\gamma} = 100\ s^{-1}$ the scattering pattern is significantly more anisotropic with high intensity nodes perpendicular to the flow direction. This indicates that the rods were preferentially aligned in the flow direction. Little change was seen in the intensity of the isotropic ring from 0.1 to 10 s^{-1}, but the intensity decreased noticeably from 10 to 100 s^{-1}. As discussed previously, shear during loading caused the 7.16 vol % dispersion to exhibit an anisotropic scattering pattern at 0 s^{-1}. At 0.01 s^{-1} there was some initial alignment in the flow direction, but the pattern remained predominantly isotropic. At 0.1 s^{-1} two high intensity nodes were observed perpendicular to the flow direction and little isotropic ring remained. Unlike the more sudden drop in the biphasic dispersion, for the gel, the intensity of the remaining isotropic ring decreased steadily as the shear rate increased from 0.1 to 100 s^{-1}.

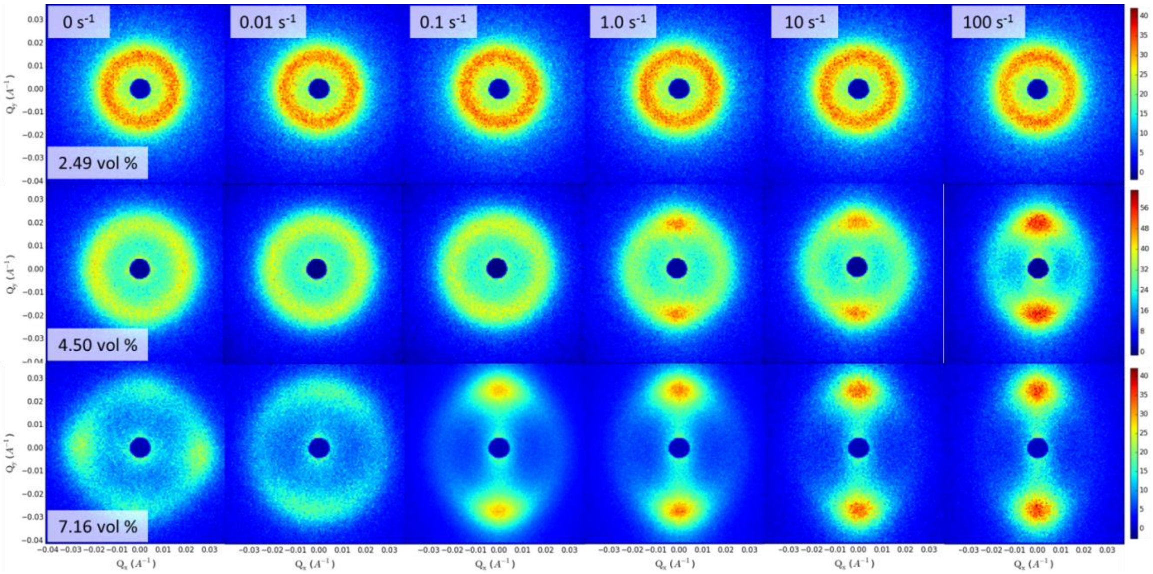

Figure 5.5 Reduced two-dimensional scattering data for the 2.49, 5.16, and 7.16 vol % dispersions at a range of shear rates between 0 and 100 s^{-1}. Note that the anisotropy in the 7.16 vol % at 0 s^{-1} is caused by shear during sample loading and is not representative of the dispersion's rest state.

In order to quantify the degree of CNC alignment, an annular average was calculated for each 2D scattering pattern. The average was taken over a 0.0056 Å q range centered on the maximum intensity for each respective concentration. These annular averages were used to calculate the order parameter $\bar{P}_2$ using the method presented by Burger et. al.[107] The orientational distribution function F(q,ϕ), given by the annular averages are well fit by a Legendre series expansion:

$$F(q,\phi)=\sum_{n=0}^{\infty} a_n P_{2n}(\cos\phi) \tag{5.1}$$

where the values, a_n, are fitting coefficients, the functions, P_{2n}, are even Legendre polynomials, and ϕ is the azimuthal angle. The first six terms of the expansion were used to fit the annular averages. Experimental annular averages and Legendre series fits are shown in Figure 5.6. The order parameter is directly related to the a_1 coefficient from the Legendre expansion.[107]

$$\bar{P}_2 = \frac{a_1}{5} \tag{5.2}$$

The value of $\bar{P}_2$ will vary from 0 for random CNC orientation to 1 for rods perfectly aligned in the flow direction. The order parameter was calculated for all samples at all shear rates tested and is shown in Figure 5.7.

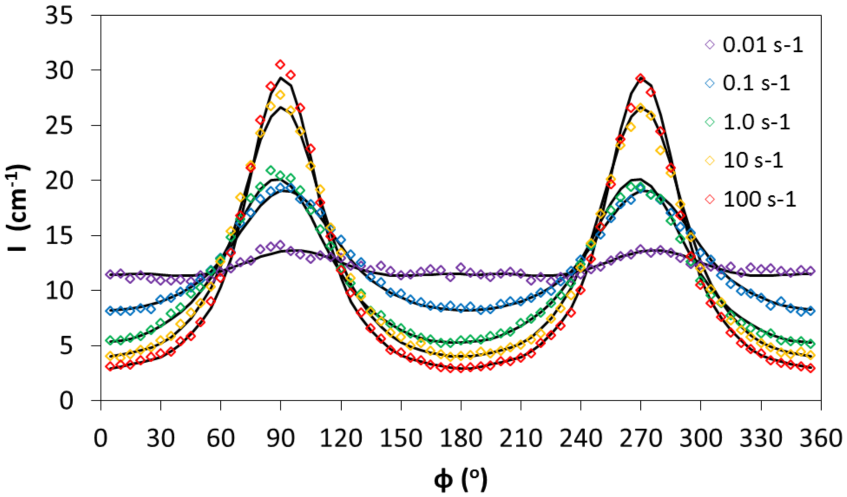

Figure 5.6 Annular averages of 2D scattering patterns for 8.48 vol % CNC at shear rates ranging from 0.01 to 100 s^{-1}. Solid lines are Legendre expansion fits.

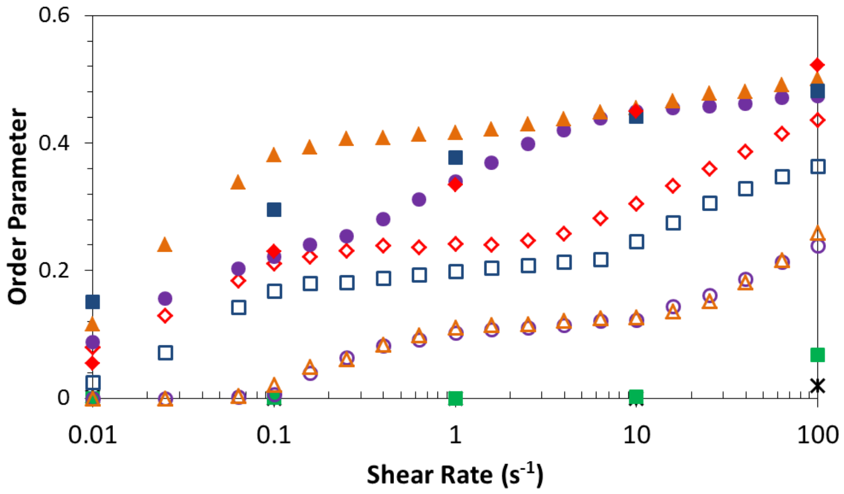

Figure 5.7 Order parameter versus shear rate for CNC dispersions at 2.49 vol % (black stars), 3.16 vol % (green closed squares), 3.83 vol % (purple open circles), 4.50 vol % (orange open triangles), 5.16 vol % (blue open squares), 5.83 vol % (red open diamonds), 6.50 vol % (purple closed circles), 7.16 vol % (orange closed triangles), 7.82 vol % (blue closed squares), and 8.48 vol % (red closed diamonds).

At 2.49 and 3.16 vol %, where the dispersions were either completely or predominantly isotropic, the order parameter remained 0 until the shear rate was between 10 and 100 s^{-1}. This agrees well with the onset of shear thinning at 25 and 10 s^{-1} for these dispersions, respectively. The biphasic dispersions from 3.83 to 5.83 vol % had three region order parameter versus shear rate curves similar to those of the viscosity versus shear rate curves. However, in each of these curves, the transitions between regions were shifted to a higher shear rate than for viscosity versus shear rate data. Additionally, the region II plateaus were flatter and more broad than those in the viscosity versus shear rate curves. The region I to II transition occurred at 1.0 s^{-1} for the 3.83 and 4.50 vol % dispersions and at 0.158 s^{-1} for the 5.16 and 5.83 vol % dispersions. The transition from region II to region III occured at 10 s^{-1} at 3.83 and 4.50 vol %, and at 6.31 and 3.98 s^{-1} for 5.16 and 5.83 vol %, respectively (Table 5.2). Interestingly, although Orts et. al. observed a three region viscosity versus shear rate curve for their liquid crystalline sample, they did not see three regions in the order parameter versus shear rate curve.[67] In fact, they saw the order parameter increase at its highest rate during the plateau in viscosity. This suggests that there may be a different mechanism behind region II behavior in biphasic dispersions. We suggest that in region I CNC liquid crystalline domains elongate and the directors are aligned in the flow direction; this would result in the observed increase in order parameter and a corresponding decrease in viscosity. At the transition to region II, all the liquid crystalline domains have their directors oriented in the direction of shear, however the shear rate is not high enough to align the CNC in the isotropic domains. This results in the biphasic dispersions at intermediate shear rates having scattering patterns that consisted of both anisotropic nodes and an isotropic ring. Vorticity alignment has also been suggested as a possible mechanism for region II behavior.[47] However, scattering patterns collected in tangential beam alignment showed only isotropic rings, suggesting no alignment of the CNC in the vorticity direction in contrast to Ebeling et. al.[68] The transition to region III occurred when the shear rate was high enough to begin aligning the isotropic domains in the flow direction; in the 3.16 vol % dispersion shear alignment began at 10 s^{-1} and in the 3.83 and 4.50 vol % the onset of region III was at 10 s^{-1}. The 5.16 and 5.83 vol % transitioned to region III at lower shear rate ($\dot{\gamma} = 1.0\ s^{-1}$), which is likely a result of a higher concentration of rods in the isotropic phase at the higher overall dispersion concentration, as shown by Dong et. al.[108] As the shear rate was further increased in region III the liquid crystalline and isotropic domains merged and all rods were further aligned in the flow direction.

Table 5.2 Shear rate at region transitions for CNC dispersions from SANS data.

Conc. (vol %)	**Region I →II $\dot{\gamma}$**	**Region II →III $\dot{\gamma}$**
3.83	1.0	10.0
4.50	1.0	10.0
5.16	0.158	6.31
5.83	0.158	3.98

Cross-polarized optical microscope images are shown for the 4.50 vol % dispersion during flow in Figure 5.8. At $\dot{\gamma} = 1.0\ s^{-1}$the domains are clearly elongated in the flow direction, however, as indicated by bright birefringent domains at both polarization angles, the domain directors are not uniformly oriented in the flow direction. By $\dot{\gamma} = 1.0\ s^{-1}$, at the region I → II transition, the 0^o image shows significantly fewer birefringent domains than the 45^o image, indicating that the domain directors are aligned in the direction of flow. A decrease in domain size is also observed from 0.1 to 1.0 s^{-1}. This could explain the shift in the region transitions to lower shear rates in the viscosity curves, as viscosity is dependent on domain size while order parameter is not.[43] In region II ($\dot{\gamma} = 1.0 - 10\ s^{-1}$) some further domain breakup and alignment is observed, however in region III ($\dot{\gamma} = 10 - 100\ s^{-1}$) the liquid crystalline and isotropic domains are seen to fully merge into a monodomain aligned in the flow direction.

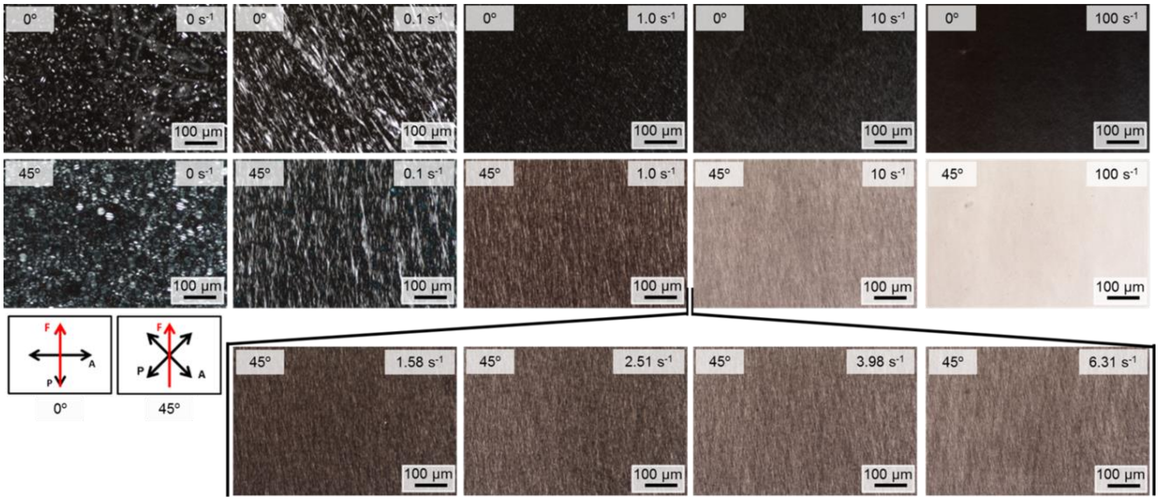

Figure 5.8 Shear cell cross-polarized optical microscope images of the 4.50 vol % dispersion. The top two rows show the beginning of each decade of shear. In the top row the flow direction is parallel to the polarization axis, on the middle row the flow direction is at 45° to the polarization axis. The bottom row shows region II behavior with the flow direction at 45° to the polarization axis.

While the viscosity versus shear rate curves of the 6.50 vol % and 7.16 vol % gels had a single power law, the order parameter curve showed a transition from high slope to low slope at 6.31 and 0.1 s^{-1} for the 6.50 and 7.16 vol % dispersions, respectively. However, the 7.82 and 8.48 vol % exhibit a single slope with the maximum observed order parameter of 0.52 occurring for the 8.48 vol % gel at 100 s^{-1}. Orts and Ebeling observed maximum order parameters of 0.92 and 0.75 for their liquid crystalline dispersions, however this was at at $\dot{\gamma} > 1000\ s^{-1}$.[67-68] In the gel regime, as the concentration and viscosity increased, the increased resistance to flow was evident at low shear rates. At $\dot{\gamma} < 10\ s^{-1}$ the order parameter for the 7.16 vol % gel is higher than that of the 7.83 and 8.46 vol % gels (Figure 5.9).

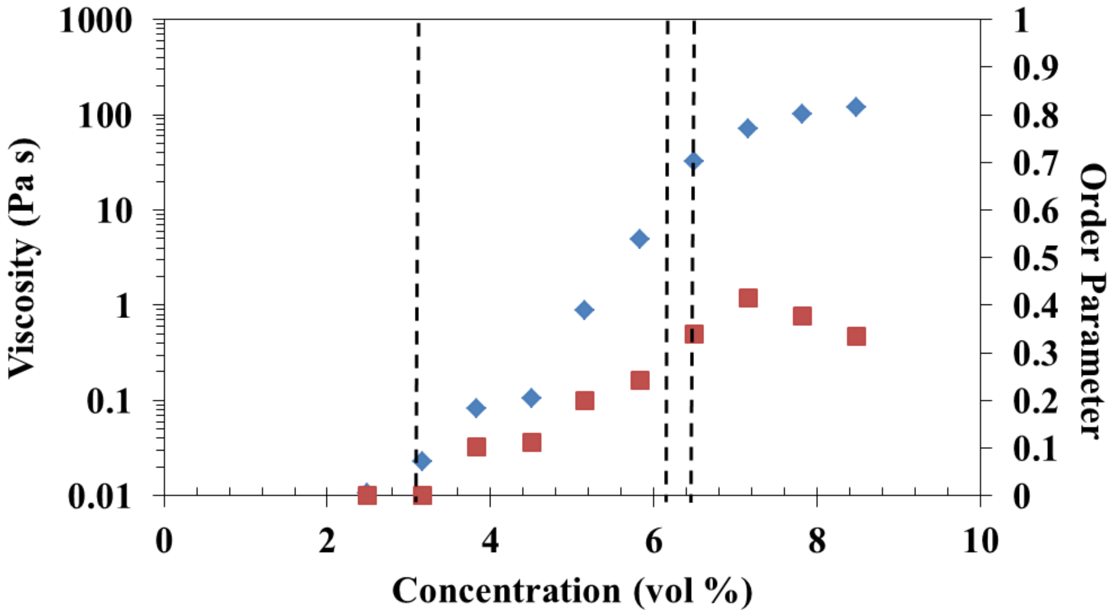

Figure 5.9 Order parameter (red squares) and viscosity (blue diamonds) versus concentration for CNC dispersions at $\dot{\gamma}$ = 1.0 s^{-1}. The vertical dashed lines indicate approximate phase transitions from isotropic to biphasic, biphasic to liquid crystalline, and liquid crystalline to gel.

Scattering data was also collected, and the order parameters calculated, for up to 60 minutes after the cessation of shear ($\dot{\gamma}$ = 100 s^{-1}); the changes in order parameter versus relaxation time are shown in Figure 5.10. In the isotropic dispersions, the relaxation occurred almost immediately after flow was stopped. The scattering patterns for the 3.83 and 4.50 vol % dispersions become isotropic after approximately 10 minutes of relaxation; as the concentration was further increased the relaxation time continued to increase. The 8.48 vol % dispersion showed no significant relaxation over one hour. In fact, the order parameter increased slightly from 0.52 to 0.59 after flow is stopped. This increase was also seen by Orts et. al. and was attributed to rod “wobbling” due to the velocity gradient in the Couette cell.[67]

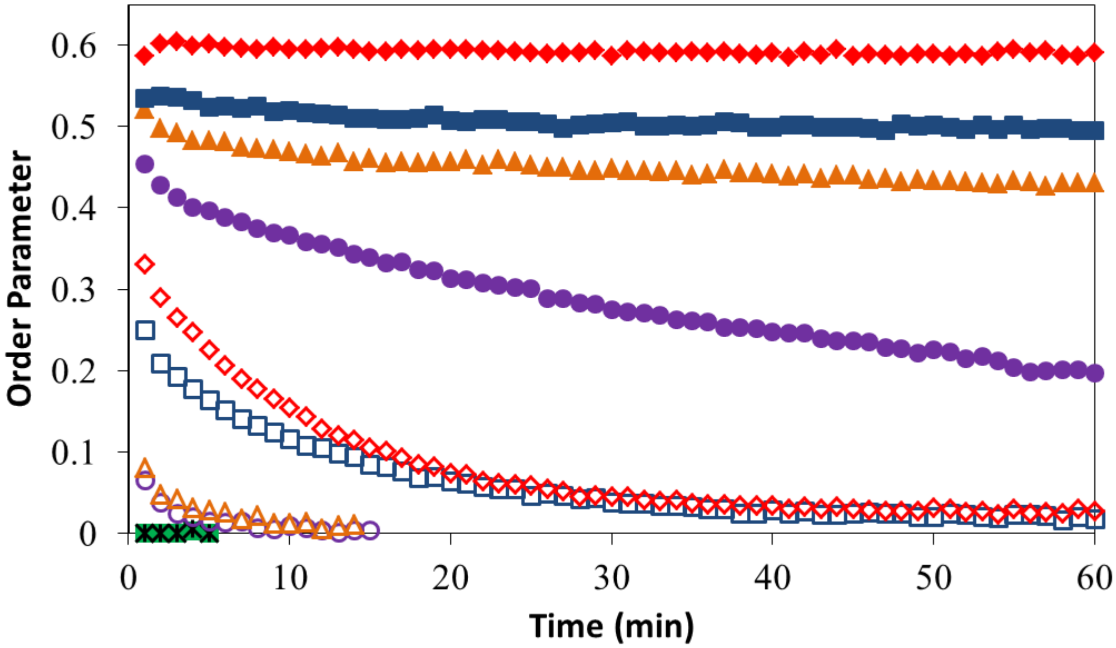

Figure 5.10 Order parameter vs. time after cessation of shear ($\dot{\gamma}$ = 100 s^{-1}) for CNC dispersions at 2.49 vol % (black stars), 3.16 vol % (green closed squares), 3.83 vol % (purple open circles), 4.50 vol % (orange open triangles), 5.16 vol % (blue open squares), 5.83 vol % (red open diamonds), 6.50 vol % (purple closed circles), 7.16 vol % (orange closed triangles), 7.82 vol % (blue closed squares), and 8.48 vol % (red closed diamonds).

5.2 Modeling

In collaboration with the Green Group at Texas A&M, a model for flow behavior in chiral liquid crystals has been built using COMSOL, a finite elements modeling software. The model is based on an approach which combines the original Doi-Edwards model[30] and Leslie-Ericksen theory[109], which has been termed Landau-de Gennes, and has been used by a number of researchers in recent years.[110-113] While Landau-de Gennes describes nematic liquid crystals, it can be modified with a chiral term to account for cholesterics.[114] While this theory is well-described, virtually all prior work on cholesteric systems has been limited in geometry and helicity of the cholesteric phase.[115-117] The model that has been developed by the Green Group allows for 3D freedom of the cholesteric helix and variation in pitch. The model is described by Equation 5.3:

$$\begin{aligned}\frac{dQ}{dt} &= W \bullet Q - Q \bullet W + \frac{2}{3}\beta A + \beta\left[A \bullet Q + Q \bullet A - \frac{2}{3}(A:Q)I \right] \\ &- \frac{1}{2}\beta\left[(A:Q)Q + A \bullet Q \bullet Q + Q \bullet A \bullet Q + Q \bullet B \bullet A((Q \bullet Q):A)I\right] \\ &- \frac{6R}{Er}\left[(1 - {}^{U}\!/_{3})Q - UQ \bullet Q + U(Q:Q)(Q + {}^{I}\!/_{3})\right] \\ &+ \frac{1}{Er}\left[\nabla^2 Q + \frac{1}{2}\frac{L_2}{L_1}(\nabla(\nabla \bullet Q) + (\nabla(\nabla \bullet Q)^T) - \frac{2}{3}tr(\nabla(\nabla \bullet Q)I \right] + P\end{aligned} \tag{5.3}$$

Where: $P = \frac{\theta}{Er}(\in_{mik}\ Q_{mj,k} + \in_{mjk}\ Q_{mi,k})$

In this equation Q is the orientation tensor, W is the vorticity tensor, β is the shape factor which is used to describe the shape of the mesogens, A is the rate of deformation which relates to velocity and shear rate, R is a short range interaction to long range elasticity term, Er is the Erickson number, U relates to the concentration of the dispersion, L_2/L_1 describes twist, bend and splay, and P is the chiral term where θ is the chiral force parameter. The first two lines of the equation contain flow terms, the third line contains thermodynamic terms which describe the nematic behavior of the system, the fourth line (excluding P) contains elastic or gradient penalizing terms, and P is the chiral term. In the model x is the flow direction, z is the vorticity direction, and y is the gradient direction.

At this point in the research, the model has only been used qualitatively by comparing it to polarized microscope images taken during the relaxation of liquid crystalline CNC dispersions after flow. Figure 5.11 shows representative images from the model and experiments for short, intermediate, and long time after the cessation of flow. In Figure 5.11 a and d, at short time, all of the CNC are oriented in the flow direction, as indicated by the orientation of the ellipsoids in the model and the single color of the microscope image. At intermediate times a zig-zag pattern emerges in both the model and the microscope image. While the model shows more variation along the vorticity direction than the microscope image, the general trend is the same.

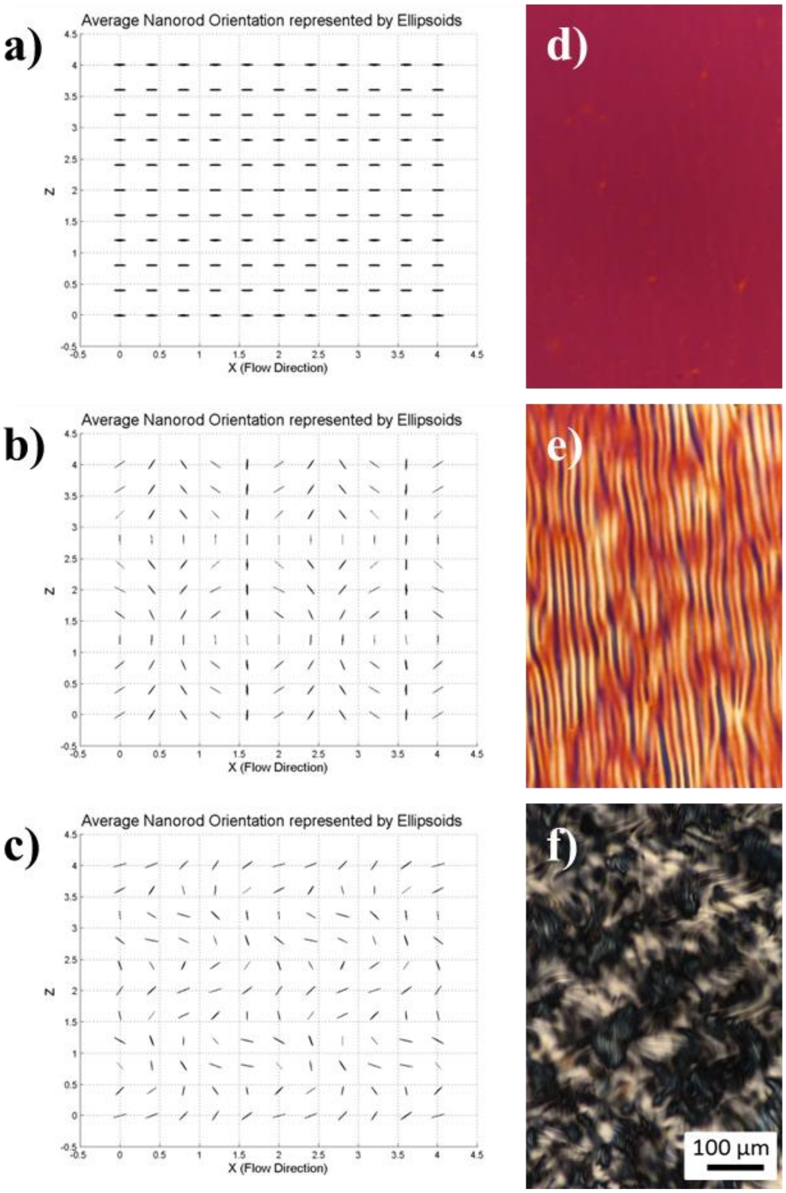

Figure 5.11 Model results and cross-polarized optical microscope images for liquid crystalline dispersion relaxation after high shear. a) and d) show time 0 where all rods are aligned in the flow direction. b) and e) show intermediate time where a zig-zag pattern is present. c) and f) show a long time after shear where the cholesteric structure has formed.

After the zig-zag pattern shown in Figure 5.11b and Figure 5.11e, the dispersions transitions to a polydomain cholesteric structure as seen in Figure 5.11f. While the model does not currently take polydomain structure into account, by focusing on a small region of the microscope images you can see the zig-zag pattern transition into a cholesteric fingerprint within a domain, as the model does between Figure 5.11b and Figure 5.11c. This transition is shown on the optical microscope in Figure 5.12.

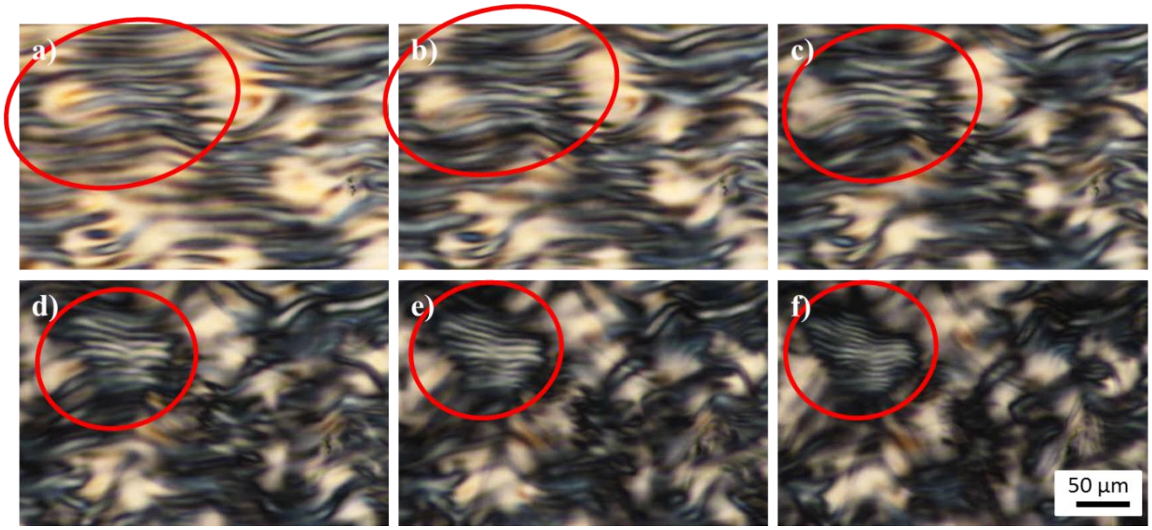

Figure 5.12 Polarized optical microscope image showing transition from zig-zag pattern to cholesteric fingerprint texture within a domain. Time is increasing from a) to f).

Future modeling work includes quantifying the alignment in the model as an order parameter. To will be done by taking the volumetric average of Equation 5.4.

$$S = 3/2(Q : nn) \tag{5.4}$$

Where Q is the orientation tensor for every point in the mesh and n is the unit vector in the flow direction. Model parameters will then be fit with experimental neutron scattering data.

Chapter 6 Conclusion

This dissertation has presented the results of highly collaborative research on the fluid-phase assembly of cellulose nanocrystals (CNC) into nematically aligned and chiral films for application in microelectromechanical systems (MEMS) or optical devices. The key contribution of this research has been to obtain insight into the relationship between dispersion microstructure, shear response, and the final structure and properties of the film. These results can be used to guide the development of specific applications based on CNC films. The results of this work largely stem from the combination of rheological measurements with structural measurements from optical microscopy and small-angle neutron scattering (SANS).

Rheo-optical images along with optical contrast measurements were used as a unique, effective, and facile method for quantifying alignment in CNC dispersion, microstructural relaxation after shear, and the anisotropy of CNC films. Flow alignment of CNC dispersions strongly depended on the initial dispersion microstructure. In the biphasic regime at $\dot{\gamma} = 100\ s^{-1}$, the dispersion had an optical contrast of 0.80, and relaxed within minutes of cessation of shear. The gel dispersion showed a strong resistance to flow, it had an optical contrast of 0.69 at $\dot{\gamma} = 100\ s^{-1}$ and retained its structure for hours after the cessation of shear. In contrast, due to its intrinsic alignment from liquid crystalline ordering, the liquid crystalline dispersion was easily aligned by flow. It had an optical contrast of 0.91 and maintained significant alignment for approximately ten minutes. Both the flow alignment of the dispersion and the microstructural relaxation were shown to be important in the casting of flow-aligned films. Upon film casting, the biphasic dispersion relaxed during drying resulting in a film with no optical contrast and therefore no global alignment. While the gel retained its flow induced alignment in the film, the optical contrast was low due to the dispersion's resistance to flow. The combination of high flow induced alignment and longer microstructural relaxation time in the liquid crystalline dispersion resulted in films with optical contrast values as high as 0.96, resulting from the high alignment of the CNC. Depending on their thickness, these highly aligned CNC films can be optically transparent in the visible regime or exhibit tunable interference colors.

The aligned CNC films prepared through simple doctor blade coating were used as a novel material platform for MEMS. Conventional microscale test structures were fabricated from CNC films. Using those structures, an elastic modulus that is not vastly different (*i.e.*, within an order of magnitude) from that of polycrystalline silicon was measured. Moreover, anisotropic mechanical properties were qualitatively observed in the micro-cantilever beam arrays, which is not possible in current silicon devices. This finding leads the way to a new paradigm in MEMS fabrication, sensing, and specialty application areas.

Within the growing body of work on the rheology of CNC dispersions, multiple variations from the typical rheological behavior of lyotropic liquid crystals has been observed. The first being the absence of a maximum in the viscosity versus concentration curve, and the second being three region like behavior in biphasic dispersions and not liquid crystalline dispersions. Rheo-SANS was used to investigate the flow induced structure of CNC in the biphasic regime in hopes of elucidating the reason behind these observations. The region I and III behavior of the biphasic CNC dispersions was consistent with the typically accepted causes. Region I shear thinning was caused by alignment of the liquid crystalline domain directors in the flow direction, while region III was caused by CNC alignment in the flow direction. We propose however, that region II is caused by an intermediate shear rate range where the flow is strong enough to fully align the directors of the liquid crystalline domains, but is not yet strong enough to align the isotropic CNC. While the cause of the absence of a maximum in the viscosity versus concentration curve was not elucidated by this study, it could be due to the increase in the coexistence concentrations of the biphasic regime as predicted by SLO theory. Future work to test this hypothesis should include rheology of CNC dispersions through the biphasic and liquid crystalline regions where the pH is adjusted to remain constant. The current rheo-SANS data will be used in future modeling work to better understand the reformation of the cholesteric phase after the cessation of shear. This model will be used to guide the production of chiral films with controlled structure and optical properties.

The studies presented in this dissertation on the flow behavior of CNC liquid crystal highlight the interplay between dispersion microstructure, shear response, and microstructural relaxation. The processing methods studied provide a foundation for establishing the processing route for large-scale assembly of CNC films with controlled morphology.

References

1. Roman, M.; Winter, W. In *Cellulose Nanocrystals: From Discovery to Application*, Proceedings of International Conference on Nanotechnology, Atlanta, Georgia, 2006.
2. Charreau, H.; L Foresti, M.; Vazquez, A., Nanocellulose Patents Trends: A Comprehensive Review on Patents on Cellulose Nanocrystals, Microfibrillated and Bacterial Cellulose. *Recent Patents on Nanotechnology* **2013,** *7* (1), 56-80.
3. Wegner, T. H.; Jones, P. E., Advancing Cellulose-Based Nanotechnology. *Cellulose* **2006,** *13* (2), 115-118.
4. Davis, V. A., Liquid Crystalline Assembly of Nanocylinders. *Journal of materials research* **2011,** *26* (02), 140-153.
5. Liu, J.-W.; Liang, H.-W.; Yu, S.-H., Macroscopic-Scale Assembled Nanowire Thin Films and Their Functionalities. *Chemical reviews* **2012,** *112* (8), 4770-4799.
6. Huang, Y.; Duan, X.; Wei, Q.; Lieber, C. M., Directed Assembly of One-Dimensional Nanostructures into Functional Networks. *Science* **2001,** *291* (5504), 630-633.
7. Kiss, G. Rheology and Rheo-Optics of Concentrated Solutions of Helical Polypeptides. Dissertation, University of Massachusetts-Amherst, Amherst, MA, 1979.
8. Green, M. J.; Behabtu, N.; Pasquali, M.; Adams, W. W., Nanotubes as Polymers. *Polymer* **2009,** *50* (21), 4979-4997.
9. Green, M. J.; Parra-Vasquez, A. N. G.; Behabtu, N.; Pasquali, M., Modeling the Phase Behavior of Polydisperse Rigid Rods with Attractive Interactions with Applications to Single-Walled Carbon Nanotubes in Superacids. *The Journal of Chemical Physics* **2009,** *131* (8), 084901.
10. Davis, V. A.; Parra-Vasquez, A. N. G.; Green, M. J.; Rai, P. K.; Behabtu, N.; Prieto, V.; Booker, R. D.; Schmidt, J.; Kesselman, E.; Zhou, W.; Fan, H.; Adams, W. W.; Hauge, R. H.; Fischer, J. E.; Cohen, Y.; Talmon, Y.; Smalley, R. E.; Pasquali, M., True Solutions of Single-Walled Carbon Nanotubes for Assembly into Macroscopic Materials. *Nature Nanotechnology* **2009,** *4* (12), 830-834.
11. Dobb, M.; Johnson, D.; Saville, B., Supramolecular Structure of a High Modulus Polyaromatic Fiber (Kevlar 49). *Journal of Polymer Science: Polymer Physics Edition* **1977,** *15* (12), 2201-2211.

12. Revol, J.-F.; Bradford, H.; Giasson, J.; Marchessault, R.; Gray, D., Helicoidal Self-Ordering of Cellulose Microfibrils in Aqueous Suspension. *International journal of biological macromolecules* **1992,** *14* (3), 170-172.

13. Brown, R. M., Cellulose Structure and Biosynthesis: What Is in Store for the 21st Century? *Journal of Polymer Science Part A: Polymer Chemistry* **2004,** *42* (3), 487-495.

14. O'Sullivan, A. C., Cellulose: The Structure Slowly Unravels. *Cellulose* **1997,** *4* (3), 173-207.

15. Habibi, Y.; Lucia, L. A.; Rojas, O. J., Cellulose Nanocrystals: Chemistry, Self-Assembly, and Applications. *Chemical Reviews* **2010,** *110* (6), 3479-3500.

16. Rånby, B., Aqueous Colloidal Solutions of Cellulose Micelles. *Acta Chemica Scandinavica* **1949,** *3* (5), 649-650.

17. Sjöström, E., *Wood Chemistry: Fundamentals and Applications*. Gulf Professional Publishing: Houston, 1993.

18. Gardner, K.; Blackwell, J., The Hydrogen Bonding in Native Cellulose. *Biochimica et Biophysica Acta* **1974,** *343* (1), 232-237.

19. Urena-Benavides, E. E.; Ao, G.; Davis, V. A.; Kitchens, C. L., Rheology and Phase Behavior of Lyotropic Cellulose Nanocrystal Suspensions. *Macromolecules* **2011,** *44* (22), 8990-8998.

20. Davidson, G., The Rate of Change in the Properties of Cotton Cellulose under the Prolonged Action of Acids. *Journal of the Textile Institute Transactions* **1943,** *34* (10), 87-96.

21. Beck-Candanedo, S.; Roman, M.; Gray, D. G., Effect of Reaction Conditions on the Properties and Behavior of Wood Cellulose Nanocrystal Suspensions. *Biomacromolecules* **2005,** *6* (2), 1048-1054.

22. Rånby, B.; Ribi, E., Über Den Feinbau Der Zellulose. *Experientia* **1950,** *6* (1), 12-14.

23. Marchessault, R.; Morehead, F.; Koch, M. J., Some Hydrodynamic Properties of Neutral Suspensions of Cellulose Crystallites as Related to Size and Shape. *Journal of Colloid Science* **1961,** *16* (4), 327-344.

24. Dong, X. M.; Revol, J.-F.; Gray, D. G., Effect of Microcrystallite Preparation Conditions on the Formation of Colloid Crystals of Cellulose. *Cellulose* **1998,** *5* (1), 19-32.

25. Battista, O., Hydrolysis and Crystallization of Cellulose. *Industrial & Engineering Chemistry* **1950,** *42* (3), 502-507.

26. Battista, O. A.; Hill, D.; Smith, P. A. Level-Off D.P. Cellulose Products. 1961.

27. Araki, J.; Wada, M.; Kuga, S.; Okano, T., Flow Properties of Microcrystalline Cellulose Suspension Prepared by Acid Treatment of Native Cellulose. *Colloids and Surfaces A: Physicochemical and Engineering Aspects* **1998,** *142* (1), 75-82.

28. Braun, B.; Dorgan, J. R., Single-Step Method for the Isolation and Surface Functionalization of Cellulosic Nanowhiskers. *Biomacromolecules* **2008,** *10* (2), 334-341.

29. Donald, A.; Windle, A.; Hanna, S., *Liquid Crystalline Polymers*. 2nd ed.; Cambridge University Press: Cambridge, 2006.

30. Doi, M.; Edwards, S. F., *The Theory of Polymer Dynamics*. Oxford University Press: New York, 1988.

31. Davis, V. A.; Ericson, L. M.; Parra-Vasquez, A. N. G.; Fan, H.; Wang, Y.; Prieto, V.; Longoria, J. A.; Ramesh, S.; Saini, R. K.; Kittrell, C.; Billups, W. E.; Adams, W. W.; Hauge, R. H.; Smalley, R. E.; Pasquali, M., Phase Behavior and Rheology of Swnts in Superacids. *Macromolecules* **2004,** *37* (1), 154-160.

32. Onsager, L., The Effect of Shape on the Interaction of Colloidal Particles. *Annals of the New York Academy of Sciences* **1949,** *51* (4), 627-659.

33. Flory, P. J., Theory of Crystallization in Copolymers. *Transactions of the Faraday Society* **1955,** *51* (6), 848-857.

34. Lekkerkerker, H. N. W.; Coulon, P.; Haegen, v. d. R., On the Isotropic-Liquid Crystal Phase Separation in a Solution of Rodlike Particles of Different Lengths. *The Journal of Chemical Physics* **1984,** *80* (7), 3427-3433.

35. Khokhlov, A., Theories Based on the Onsager Approach. In *Thermodynamics of Flowing Systems: With Internal Microstructure*, Beris, A. N.; Edwards, B. J., Eds. Oxford University Press: New York, 1991; pp 97-118.

36. Khokhlov, A.; Semenov, A., On the Theory of Liquid-Crystalline Ordering of Polymer Chains with Limited Flexibility. *Journal of Statistical Physics* **1985,** *38* (1-2), 161-182.

37. Speranza, A.; Sollich, P., Isotropic-Nematic Phase Equilibria in the Onsager Theory of Hard Rods with Length Polydispersity. *Physical Review E* **2003,** *67* (6), 061702.

38. Speranza, A.; Sollich, P., Isotropic-Nematic Phase Equilibria of Polydisperse Hard Rods: The Effect of Fat Tails in the Length Distribution. *The Journal of Chemical Physics* **2003,** *118* (11), 5213-5223.

39. Wensink, H.; Vroege, G., Isotropic–Nematic Phase Behavior of Length-Polydisperse Hard Rods. *The Journal of Chemical Physics* **2003,** *119* (13), 6868-6882.

40. Stroobants, A.; Lekkerkerker, H.; Odijk, T., Effect of Electrostatic Interaction on the Liquid Crystal Phase Transition in Solutions of Rodlike Polyelectrolytes. *Macromolecules* **1986,** *19* (8), 2232-2238.

41. Odijk, T., Theory of Lyotropic Polymer Liquid Crystals. *Macromolecules* **1986,** *19* (9), 2313-2329.

42. Larson, R. G., *The Structure and Rheology of Complex Fluids*. Oxford University Press: New York, 1999.

43. Wissbrun, K. F., Rheology of Rod-Like Polymers in the Liquid Crystalline State. *Journal of Rheology* **1981,** *25* (6), 619-662.

44. Kiss, G.; Porter, R. S., Flow Induced Phenomena of Lyotropic Polymer Liquid Crystals: The Negative Normal Force Effect and Bands Perpendicular to Shear. In *Mechanical and Thermophysical Properties of Polymer Liquid Crystals*, Springer: 1998; pp 342-406.

45. Onogi, S.; Asada, T., Rheology and Rheo-Optics of Polymer Liquid Crystals. In *Rheology*, Springer: 1980; pp 127-147.

46. Asada, T.; Muramatsu, H.; Watanabe, R.; Onogi, S., Rheooptical Studies of Racemic Poly(Γ-Benzyl Glutamate) Liquid-Crystals. *Macromolecules* **1980,** *13* (4), 867-871.

47. Montesi, A.; Peña, A. A.; Pasquali, M., Vorticity Alignment and Negative Normal Stresses in Sheared Attractive Emulsions. *Physical review letters* **2004,** *92* (5), 058303.

48. Marrucci, G., Rheology of Nematic Polymers. In *Liquid Crystallinity in Polymers: Principles and Fundamental Properties*, Ciferri, A., Ed. VCH Publishers: New York, 1991; pp 395-422.

49. Kiss, G.; Porter, R. S., Rheology of Concentrated-Solutions of Helical Polypeptides. *Journal of Polymer Science Part B: Polymer Physics* **1980,** *18* (2), 361-388.

50. Walker, L. M.; Wagner, N. J.; Larson, R. G.; Mirau, P. A.; Moldenaers, P., The Rheology of Highly Concentrated Pblg Solutions. *Journal of Rheology* **1995,** *39* (5), 925-952.

51. Grizzuti, N.; Cavella, S.; Cicarelli, P., Transient and Steady-State Rheology of a Liquid-Crystalline Hydroxypropylcellulose Solution. *Journal of Rheology* **1990,** *34* (8), 1293-1310.

52. Mukherjee, S.; Woods, H., X-Ray and Electron Microscope Studies of the Degradation of Cellulose by Sulphuric Acid. *Biochimica et Biophysica Acta* **1953,** *10*, 499-511.

53. van den Berg, O.; Capadona, J. R.; Weder, C., Preparation of Homogeneous Dispersions of Tunicate Cellulose Whiskers in Organic Solvents. *Biomacromolecules* **2007,** *8* (4), 1353-1357.

54. Battista, O.; Smith, P., Microcrystalline Cellulose. *Industrial & Engineering Chemistry* **1962,** *54* (9), 20-29.

55. Araki, J.; Wada, M.; Kuga, S.; Okano, T., Influence of Surface Charge on Viscosity Behavior of Cellulose Microcrystal Suspension. *Journal of Wood Science* **1999,** *45* (3), 258-261.

56. Marchessault, R.; Morehead, F.; Walter, N., Liquid Crystal Systems from Fibrillar Polysaccharides. *Nature* **1959,** *184*, 632-633.

57. Revol, J.-F.; Marchessault, R., In Vitro Chiral Nematic Ordering of Chitin Crystallites. *International journal of biological macromolecules* **1993,** *15* (6), 329-335.

58. Revol, J. F.; Godbout, D. L.; Gray, D. G. Solidified Liquid Crystals of Cellulose with Optically Variable Properties. 1997.

59. Dong, X. M.; Gray, D. G., Effect of Counterions on Ordered Phase Formation in Suspensions of Charged Rodlike Cellulose Crystallites. *Langmuir* **1997,** *13* (8), 2404-2409.

60. Bercea, M.; Navard, P., Shear Dynamics of Aqueous Suspensions of Cellulose Whiskers. *Macromolecules* **2000,** *33* (16), 6011-6016.

61. Shafiei-Sabet, S.; Hamad, W. Y.; Hatzikiriakos, S. G., Rheology of Nanocrystalline Cellulose Aqueous Suspensions. *Langmuir* **2012,** *28* (49), 17124-17133.

62. Wu, Q.; Meng, Y.; Wang, S.; Li, Y.; Fu, S.; Ma, L.; Harper, D., Rheological Behavior of Cellulose Nanocrystal Suspension: Influence of Concentration and Aspect Ratio. *Journal of Applied Polymer Science* **2014,** *131* (15), 40525.

63. Xu, T.; Davis, V. A., Liquid Crystalline Phase Behavior of Silica Nanorods in Dimethyl Sulfoxide and Water. *Langmuir* **2014,** *30* (16), 4806-4813.

64. Xu, T.; Davis, V. A., Rheology and Shear-Induced Textures of Silver Nanowire Lyotropic Liquid Crystals. *Journal of Nanomaterials* **2015,** *2015*.

65. Ao, G.; Nepal, D.; Aono, M.; Davis, V. A., Cholesteric and Nematic Liquid Crystalline Phase Behavior of Double-Stranded DNA Stabilized Single-Walled Carbon Nanotube Dispersions. *ACS nano* **2011,** *5* (2), 1450-1458.

66. Luo, Z.; Song, H.; Feng, X.; Run, M.; Cui, H.; Wu, L.; Gao, J.; Wang, Z., Liquid Crystalline Phase Behavior and Sol–Gel Transition in Aqueous Halloysite Nanotube Dispersions. *Langmuir* **2013,** *29* (40), 12358-12366.

67. Orts, W.; Godbout, L.; Marchessault, R.; Revol, J.-F., Enhanced Ordering of Liquid Crystalline Suspensions of Cellulose Microfibrils: A Small Angle Neutron Scattering Study. *Macromolecules* **1998,** *31* (17), 5717-5725.

68. Ebeling, T.; Paillet, M.; Borsali, R.; Diat, O.; Dufresne, A.; Cavaille, J.; Chanzy, H., Shear-Induced Orientation Phenomena in Suspensions of Cellulose Microcrystals, Revealed by Small Angle X-Ray Scattering. *Langmuir* **1999,** *15* (19), 6123-6126.

69. Schütz, C.; Agthe, M.; Fall, A. B.; Gordeyeva, K.; Guccini, V.; Salajková, M.; Plivelic, T. S.; Lagerwall, J. P.; Salazar-Alvarez, G.; Bergström, L., Rod Packing in Chiral Nematic Cellulose Nanocrystal Dispersions Studied by Small Angle X-Ray Scattering and Laser Diffraction. *Langmuir* **2015,** *31* (23), 6507-6513.

70. Pan, J.; Hamad, W.; Straus, S. K., Parameters Affecting the Chiral Nematic Phase of Nanocrystalline Cellulose Films. *Macromolecules* **2010,** *43* (8), 3851-3858.

71. Edgar, C. D.; Gray, D. G., Smooth Model Cellulose I Surfaces from Nanocrystal Suspensions. *Cellulose* **2003,** *10* (4), 299-306.

72. Hoeger, I.; Rojas, O. J.; Efimenko, K.; Velev, O. D.; Kelley, S. S., Ultrathin Film Coatings of Aligned Cellulose Nanocrystals from a Convective-Shear Assembly System and Their Surface Mechanical Properties. *Soft Matter* **2011,** *7* (5), 1957-1967.

73. Reising, A. B.; Moon, R. J.; Youngblood, J. P., Effect of Particle Alignment on Mechanical Properties of Neat Cellulose Nanocrystal Films. *Journal of Science & Technology for Forest Products and Processes* **2013,** *2*, 32-41.

74. Mitov, M., Cholesteric Liquid Crystals with a Broad Light Reflection Band. *Advanced Materials* **2012,** *24* (47), 6260-6276.

75. Dumanli, A. G. m.; van der Kooij, H. M.; Kamita, G.; Reisner, E.; Baumberg, J. J.; Steiner, U.; Vignolini, S., Digital Color in Cellulose Nanocrystal Films. *ACS applied materials & interfaces* **2014,** *6* (15), 12302-12306.

76. Park, J. H.; Noh, J.; Schütz, C.; Salazar-Alvarez, G.; Scalia, G.; Bergström, L.; Lagerwall, J. P., Macroscopic Control of Helix Orientation in Films Dried from Cholesteric Liquid Crystalline Cellulose Nanocrystal Suspensions. *ChemPhysChem* **2014,** *15* (7), 1477-1484.

77. Kline, S. R., Reduction and Analysis of SANS and USANS Data Using Igor Pro. *Journal of applied crystallography* **2006,** *39* (6), 895-900.

78. Wagner, N.; Liberatore, M.; Nettesheim, F.; Helgeson, M.; Kalman, D.; Reichert, M.; Porcar, L.; Butler, P., Rheo-SANS. In *American Conference on Neutron Scattering*, Santa Fe, NM, 2008.

79. Abitbol, T.; Palermo, A.; Moran-Mirabal, J. M.; Cranston, E. D., Fluorescent Labeling and Characterization of Cellulose Nanocrystals with Varying Charge Contents. *Biomacromolecules* **2013,** *14* (9), 3278-3284.

80. Kwok, D. Y.; Neumann, A. W., Contact Angle Measurement and Contact Angle Interpretation. *Advances in colloid and interface science* **1999,** *81* (3), 167-249.

81. Uhlig, M.; Fall, A.; Wellert, S.; Lehmann, M.; Prévost, S.; Wagberg, L.; von Klitzing, R.; Nyström, G., Two-Dimensional Aggregation and Semidilute Ordering in Cellulose Nanocrystals. *Langmuir* **2016,** *32* (2), 442-450.

82. Li, M.-C.; Wu, Q.; Song, K.; Lee, S.; Qing, Y.; Wu, Y., Cellulose Nanoparticles: Structure–Morphology–Rheology Relationships. *ACS Sustainable Chemistry & Engineering* **2015,** *3* (5), 821-832.

83. Walker, L.; Wagner, N., Rheology of Region I Flow in a Lyotropic Liquid Crystal Polymer: The Effects of Defect Texture. *Journal of Rheology* **1994,** *38* (5), 1525-1547.

84. Lavrentovich, O.; Kleman, M., Cholesteric Liquid Crystals: Defects and Topology. In *Chirality in Liquid Crystals,* Springer: 2001; pp 115-158.

85. Geng, Y.; Almeida, P. L.; Feio, G. M.; Figueirinhas, J. o. L.; Godinho, M. H., Water-Based Cellulose Liquid Crystal System Investigated by Rheo-Nmr. *Macromolecules* **2013,** *46* (11), 4296-4302.

86. Kim, J.; Peretti, J.; Lahlil, K.; Boilot, J. P.; Gacoin, T., Optically Anisotropic Thin Films by Shear-Oriented Assembly of Colloidal Nanorods. *Advanced Materials* **2013,** *25* (24), 3295-3300.

87. Michel-Lévy, M.; Lacroix, A., Minéralogie Sur Nouveau Gisemant De Dumortiérite. *Comptes Rendus de I'Académie des Sciences* **1888,** *106*, 1546-1548.

88. Onogi, Y.; White, J. L.; Fellers, J. F., Rheo-Optics of Shear and Elongational Flow of Liquid Cystalline Polymer Solutions: Hydroxypropyl Cellulose/Water and Poly-P-Phenylene Terephthalamide/Sulfuric Acid. *Journal of Non-Newtonian Fluid Mechanics* **1980,** *7* (2), 121-151.

89. Kiss, G.; Orrell, T.; Porter, R. S., Rheology and Rheo-Optics of Anisotropic Poly-B-Benzyl-Aspartate Gel. *Rheologica acta* **1979,** *18* (5), 657-661.

90. Beck, S.; Bouchard, J.; Chauve, G.; Berry, R., Controlled Production of Patterns in Iridescent Solid Films of Cellulose Nanocrystals. *Cellulose* **2013,** *20* (3), 1401-1411.

91. Duggal, R.; Hussain, F.; Pasquali, M., Self-Assembly of Single-Walled Carbon Nanotubes into a Sheet by Drop Drying. *Advanced Materials* **2006,** *18* (1), 29-34.

92. Singh, K. B.; Bhosale, L. R.; Tirumkudulu, M. S., Cracking in Drying Colloidal Films of Flocculated Dispersions. *Langmuir* **2009,** *25* (8), 4284-4287.

93. Bardet, R.; Belgacem, N.; Bras, J., Flexibility and Color Monitoring of Cellulose Nanocrystal Iridescent Solid Films Using Anionic or Neutral Polymers. *ACS applied materials & interfaces* **2015,** *7* (7), 4010-4018.

94. Ansari, N. Understanding the Effect of Surface Topography on Stiction and Friction in Mems. Dissertation, Auburn University, Auburn, AL, 2011.

95. Klemm, D.; Kramer, F.; Moritz, S.; Lindström, T.; Ankerfors, M.; Gray, D.; Dorris, A., Nanocelluloses: A New Family of Nature-Based Materials. *Angewandte Chemie International Edition* **2011,** *50* (24), 5438-5466.

96. Roman, M.; Winter, W. T., Effect of Sulfate Groups from Sulfuric Acid Hydrolysis on the Thermal Degradation Behavior of Bacterial Cellulose. *Biomacromolecules* **2004,** *5* (5), 1671-1677.

97. Fernandes Diniz, J.; Gil, M.; Castro, J., Hornification—Its Origin and Interpretation in Wood Pulps. *Wood Science and Technology* **2004,** *37* (6), 489-494.

98. Fang, W.; Wickert, J., Determining Mean and Gradient Residual Stresses in Thin Films Using Micromachined Cantilevers. *Journal of Micromechanics and Microengineering* **1999,** *6* (3), 301.

99. Perry, A.; Boswell, R., Fast Anisotropic Etching of Silicon in an Inductively Coupled Plasma Reactor. *Applied Physics Letters* **1989,** *55* (2), 148-150.

100. Pruessner, M. W.; King, T. T.; Kelly, D. P.; Grover, R.; Calhoun, L. C.; Ghodssi, R., Mechanical Property Measurement of InP-Based Mems for Optical Communications. *Sensors and Actuators A: Physical* **2003,** *105* (2), 190-200.

101. Li, X.; Bhushan, B.; Takashima, K.; Baek, C.-W.; Kim, Y.-K., Mechanical Characterization of Micro/Nanoscale Structures for Mems/Nems Applications Using Nanoindentation Techniques. *Ultramicroscopy* **2003,** *97* (1), 481-494.

102. Orlova, T.; Aßhoff, S. J.; Yamaguchi, T.; Katsonis, N.; Brasselet, E., Creation and Manipulation of Topological States in Chiral Nematic Microspheres. *Nature communications* **2015,** *6*.

103. Burghardt, W. R., Molecular Orientation and Rheology in Sheared Lyotropic Liquid Crystalline Polymers. *Macromolecular Chemistry and Physics* **1998,** *199* (4), 471-488.

104. Hongladarom, K.; Burghardt, W. R., Molecular Orientation,"Region I" Shear Thinning and the Cholesteric Phase in Aqueous Hydroxypropylcellulose under Shear. *Rheologica acta* **1998,** *37* (1), 46-53.

105. Murali, S.; Xu, T.; Marshall, B. D.; Kayatin, M. J.; Pizarro, K.; Radhakrishnan, V. K.; Nepal, D.; Davis, V. A., Lyotropic Liquid Crystalline Self-Assembly in Dispersions of Silver Nanowires and Nanoparticles. *Langmuir* **2010,** *26* (13), 11176-11183.

106. Ao, G.; Nepal, D.; Davis, V. A., Rheology of Lyotropic Cholesteric Liquid Crystal Forming Single-Wall Carbon Nanotube Dispersions Stabilized by Double-Stranded DNA. *Rheologica acta* **2016**, 1-9.

107. Burger, C.; Hsiao, B. S.; Chu, B., Preferred Orientation in Polymer Fiber Scattering. *Journal of Macromolecular Science, Part C: Polymer Reviews* **2010,** *50* (1), 91-111.

108. Dong, X. M.; Kimura, T.; Revol, J.-F.; Gray, D. G., Effects of Ionic Strength on the Isotropic-Chiral Nematic Phase Transition of Suspensions of Cellulose Crystallites. *Langmuir* **1996,** *12* (8), 2076-2082.

109. Beris, A. N.; Edwards, B. J., *Thermodynamics of Flowing Systems: With Internal Microstructure*. Oxford University Press: New York, 1994.

110. Tsuji, T.; Rey, A. D., Effect of Long Range Order on Sheared Liquid Crystalline Materials Part 1: Compatibility between Tumbling Behavior and Fixed Anchoring. *Journal of Non-Newtonian Fluid Mechanics* **1997,** *73* (1), 127-152.

111. Rey, A. D.; Tsuji, T., Recent Advances in Theoretical Liquid Crystal Rheology. *Macromolecular theory and simulations* **1998,** *7* (6), 623-639.

112. Sgalari, G.; Leal, G.; Feng, J., The Shear Flow Behavior of Lcps Based on a Generalized Doi Model with Distortional Elasticity. *Journal of Non-Newtonian Fluid Mechanics* **2002,** *102* (2), 361-382.

113. Feng, J.; Chaubal, C.; Leal, L., Closure Approximations for the Doi Theory: Which to Use in Simulating Complex Flows of Liquid-Crystalline Polymers? *Journal of Rheology* **1998,** *42* (5), 1095-1119.

114. Cui, Z.; Calderer, M. C.; Wang, Q., Mesoscale Structures in Flows of Weakly Sheared Cholesteric Liquid Crystal Polymers. *DISCRETE AND CONTINUOUS DYNAMICAL SYSTEMS SERIES B* **2006,** *6* (2), 291.

115. Marenduzzo, D.; Orlandini, E.; Yeomans, J., Interplay between Shear Flow and Elastic Deformations in Liquid Crystals. *The Journal of Chemical Physics* **2004,** *121* (1), 582-591.

116. Cates, M.; Henrich, O.; Marenduzzo, D.; Stratford, K., Lattice Boltzmann Simulations of Liquid Crystalline Fluids: Active Gels and Blue Phases. *Soft matter* **2009,** *5* (20), 3791-3800.

117. Orlandini, E.; Marenduzzo, D.; Yeomans, J. M., Shear Dynamics in Cholesterics. *Computer physics communications* **2005,** *169* (1), 122-125.